SANDIA REPORT
SAND2021-13956
Printed April 2021

Sandia National Laboratories

Evaluation of Microhole Drilling Technology for Geothermal Exploration, Assessment, and Monitoring

Jiann-cherng Su
Anirban Mazumdar
Stephen Buerger
Adam Foris

Dennis Kaspereit (Geothermal Resources Group)
Brian Faircloth (Foro Energy, Inc.)

Prepared by
Sandia National Laboratories
Albuquerque, New Mexico
87185 and Livermore,
California 94550

Issued by Sandia National Laboratories, operated for the United States Department of Energy by National Technology & Engineering Solutions of Sandia, LLC.

Available to DOE and DOE contractors from

U.S. Department of Energy
Office of Scientific and Technical Information
P.O. Box 62
Oak Ridge, TN 37831

Telephone: (865) 576-8401
Facsimile: (865) 576-5728
E-Mail: reports@osti.gov
Online ordering: http://www.osti.gov/scitech

Available to the public from

U.S. Department of Commerce
National Technical Information Service
5301 Shawnee Rd
Alexandria, VA 22312

Telephone: (800) 553-6847
Facsimile: (703) 605-6900
E-Mail: orders@ntis.gov
Online order: https://classic.ntis.gov/help/order-methods/


DEPARTMENT OF ENERGY
UNITED STATES OF AMERICA
NNSA
National Nuclear Security Administration

ABSTRACT

One of the greatest barriers to geothermal energy expansion is the high cost of drilling during exploration, assessment, and monitoring. Microhole drilling technology—small-diameter 2–4 in. (~5.1–10.2 cm) boreholes—is one potential low-cost alternative for monitoring and evaluating bores. However, delivering high weight-on-bit (WOB), high torque rotational horsepower to a conventional drill bit does not scale down to the hole sizes needed to realize the cost savings. Coiled tube drilling technology is one solution, but these systems are limited by the torque resistance of the coil system, helical buckling in compression, and most of all, WOB management. The evaluation presented herein will: (i) evaluate the technical and economic feasibility of low WOB technologies (specifically a percussive hammer and a laser-mechanical system), (ii) develop downhole rotational solutions for low WOB drilling, (iii) provide specifications for a low WOB microhole drilling system, (iv) implement WOB control for low WOB drilling, and (v) evaluate and test low WOB drilling technologies.

This page left blank.

EXECUTIVE SUMMARY

Our evaluation was able to validate and establish a proof-of-concept low weight-on-bit (WOB) drilling technology for microhole drilling, taking us one step closer to a more affordable approach to geothermal energy development. One of the greatest barriers to widespread geothermal energy development is the high cost of drilling during exploration, assessment, and monitoring. Albright and Dreesen (2003) suggest that microhole drilling could reduce costs by up to 70% over conventional drilling. Furthermore, the literature revealed that microhole drilling can reduce costs by 40–60% for exploration wells and 25–40% for production and injection wells (Zhu et al., 1995) compared to conventional (large diameter) drilling techniques. However, the technology faces many technical challenges that our research aims to address.

Previous microhole studies (Jeanloz and Stone, 2013; NETL, 2006) have focused on high WOB drilling technologies, which deliver high torque rotational horsepower to a conventional drill bit but unfortunately, do not easily scale down to smaller diameter boreholes. Problems with drill string loading—such as buckling, friction, and twist—become more severe as the borehole diameter decreases. Coiled tube drilling technology (CTD) is one possible solution, but these systems are limited by the torque resistance of the coil system, helical buckling in compression, and WOB management.

The research presented herein represents a major departure from previous microhole drilling studies. Rather than miniaturizing high WOB conventional rotating drilling methods, our study focuses on low WOB drilling technologies. This approach helps mitigate the issues surrounding drill string torsion and buckling and provides more flexibility in the type of components that can be used on the ground surface and in the bottom hole assembly (BHA). The primary objective of our research is to validate and establish a proof-of-concept low WOB drilling technology for microhole drilling for geothermal energy development. To meet our main objective, we undertook the following tasks:

- Researched historical microhole drilling costs to establish a baseline for our study.

- Developed and tested low WOB downhole rotational mechanisms compatible with CTD technology.
- Developed specifications for a field-deployable low WOB microhole drilling system.
- Developed low WOB control systems compatible with CTD technology.
- Evaluated and tested low WOB drilling technologies, including percussive hammers and high-power laser-mechanical drilling systems.

Our study included a market survey to evaluate the true costs of microhole drilling using current technologies (i.e., high WOB) to establish a baseline for our project as we develop low WOB techniques. Microhole drilling cost savings are realized through reduced material costs (e.g., fluid volume, piping, etc.); smaller drilling/workover rigs; and lower fuel consumption. We found limited data on actual microhole drilling costs and were unable to specify a typical cost per foot of borehole drilled, but we were able to normalize drilling costs with respect to hole size to define a relative cost factor associated with borehole size, borehole depth, and casing size. The goal of our program is to evaluate comparable drilling scenarios using the relative cost factor approach to be competitive with previous microhole coiled tubing drilling operations.

Our partners at Geothermal Resources Group conducted computer simulations to determine the limiting flow rate as a function of borehole depth, borehole diameter, enthalpy, productivity index (PI), and flow rate. The simulations demonstrated that using conventional techniques, such as production and injection tests, to characterize reservoir performance has limitations for scaling microhole test results to production-size boreholes. In smaller boreholes, the ability to conduct a production test is heavily dependent on enthalpy and PI. Injection tests quickly reach the capacity of the pumping equipment or the casing shoe pressure limits before significant injection rates are achieved. Our simulations showed that evaluating microholes using current production or injection test methods does not provide sufficient resolution of the critical parameters to scale up performance to production-sized wells. However, the results of the modeling were used to help define what a microhole should be. In this application, the target borehole diameter was limited to 3–4 in. (~7.6–10.2 cm).

Our program developed system-level specifications and tested two low WOB drilling technologies:

- Laser-assisted mechanical drill, which was tested in the laboratory and is currently at a low technology readiness level (TRL), and
- Lightly modified commercial off-the-shelf (COTS) percussive hammer, which was deployed in the field and has a high TRL due to its commercial availability.

The specifications we prepared addressed subsystems, including the drill conveyance system, surface equipment, WOB control, rotation, and BHA with a focus on the latter three subsystems. We also briefly addressed the mechanical, electrical, and optical system interfaces between components of the system. Other specifications included requirements for rotation speed, torque, borehole diameter, and maximum operating temperature and pressure.

Foro Energy designed, built, and laboratory tested a high-power optics package and 3⅝ diameter mechanical laboratory drilling BHA. A rate of penetration (ROP) of 17 ft/hr (5.2 m/hr) was achieved with 1,000 lbs (~454 kg) WOB, 20 kW (~27 hp) of power, and 200 rpm through Sierra White Granite test samples. The resulting torque was 70 lbf-ft (~95 Nm). The system experienced reliability issues that prevented it from achieving all the desired parameters in the original design specifications. The sub-optimum beam profile also slowed the drilling process. These problems, coupled with the inability to achieve the desired ROP, led to the conclusion that the BHA should be redesigned. Thus, future work should focus on designing and testing a system to improve manufacturability, assembleability, ROP, and reliability.

Sandia deployed a lightly modified commercial percussive hammer at the Blue Canyon Dome field site in Socorro, New Mexico, to evaluate its technical feasibility for microhole drilling. Percussive hammers are well-suited for use in the hard, brittle rock characteristic of geothermal formations and may reduce overall costs by significantly improving the ROP. Additionally, downhole hammers are compatible with low-density fluids that are often used for geothermal drilling. We largely focused on identifying gaps that need to be filled to allow COTS hardware to be used in the low WOB microhole

drilling system. This was done to provide a path towards commercial adoption since the tools have been proven and are already at a high TRL. We developed and refined a WOB control algorithm used in the overall system controller to optimize the WOB during drilling.

This program also evaluated options for downhole bit rotation for low WOB drilling because the ability to generate rotation downhole and control WOB will be key to the success this technology. Previous efforts at microhole drilling utilized turbines and small diameter positive displacement motors, but Sandia is currently developing alternatives to those approaches. The final concept for the microhole motor is an amalgamation of various approaches and is compatible with both rock reduction techniques pursued in this effort. Initial tests of the motor design were conducted on the Sandia Dynamometer Test Stand, and later tests were laboratory-scale drilling tests conducted at the Sandia High Operating Temperature (HOT) drilling facility to test the tool under more realistic drilling conditions. The test results showed no obvious signs of accelerated wear or damage on the internal motor components following testing.

Our evaluation of low WOB drilling also included the development of a novel mechanism that enables effective and controllable downhole WOB transmission and torque reaction. The scalable and simple mechanical device can react large torques while transmitting controlled force to the drill bit. Based on the downhole motor design and previous drilling experience, the functional requirements include the capacity to resist up to 450 Nm (300 lbf-ft) torque at the downhole motor while achieving nominal downhole WOB of 2,225－4,450 N (500－1,000 lbf) during continuous drilling. Our results demonstrated effective torque reaction, axial force transmission, favorable scaling with multiple modules, and predictable performance that is proportional to the applied force. Other drilling systems requiring downhole rotation, such as directional drilling, could benefit from the ability to react torque near the motor rather than with the drill string. Similarly, the mechanical advantage principles can be used to create other types of relevant devices, such as inchworm type devices that lock within the borehole or cutting tools that exploit mechanical advantage to apply large radial loads to the borehole wall.

Our program successfully demonstrated the technical feasibility of low WOB microhole drilling for geothermal energy development, and the results warrant further investigation

into ways to improve subsystems and components for this purpose. Specifically, drilling components need to be ruggedized (made more durable) to withstand the extreme pressures encountered during drilling, and the drill conveyance system, which advances the drill bit and retracts it on pullback, requires additional capacity for pullback.

ACKNOWLEDGEMENTS

The authors would like to thank Dale Wolfer at Atlas Copco for input in percussive hammer selection and technical assistance. The authors would like to thank the DOE-GTO for supporting this work.

CONTENTS

LIST OF FIGURES

LIST OF TABLES

ACRONYMS AND DEFINITIONS

Abbreviation	Definition
AC	Alternating current
API	American Petroleum Institute
AQ	standard wireline bit size (48 mm OD, 27 mm ID)
BCD	Blue Canyon Dome
BHA	bottom hole assembly
BQ	standard wireline bit size (60 mm OD, 36.5 mm ID)
BTS	Brazilian Tensile Test
COTS	commercial off-the-shelf
CTD	coiled tube drilling
DC	direct current
DHC	downhole connector
DHC3	downhole connector 3
DLC	diamond-like carbon
DOE	Department of Energy
DST	drill stem test
DTHH	down-the-hole hammer
DTS	distributed temperature sensing
EMRTC	Energetic Materials Research and Testing Center
GTO	U.S. DOE Geothermal Technologies Office
GSS	Golden Section Search
HOT	(Sandia) High Operating Temperature (facility)
ID	inner diameter
LANL	Los Alamos National Laboratory
LWD	logging while drilling
MWD	measurement while drilling
NETL	National Energy Technology Laboratory
NQ	standard wireline bit size (75.7 mm OD, 47.6 mm ID)
OD	outer diameter
PDC	polycrystalline diamond compact (drill bit)
PDM	positive displacement motor

Abbreviation	Definition
PEEK	Polyetheretherketone
PI	productivity index
PNSM	Permanent Magnet Synchronous Machine
PTFE	polytetrafluoroethylene
QLX	Atlas Copco QLX line of percussive hammers
ROP	rate of penetration
Sandia	Sandia National Laboratories
TCF	Technology Commercialization Fund
TRL	technology readiness level
UCS	Unconfined compressive strength
WOB	weight-on-bit

1. BACKGROUND/OVERVIEW

This report documents our evaluation of low weight-on-bit (WOB) microhole drilling technology for geothermal exploration, assessment, and monitoring. The research was a team effort, including investigations by Sandia National Laboratories (Sandia), Geothermal Resources Group, and Foro Energy. As such, many of the sections were originally developed as standalone reports, containing their own references, footnotes, and writing styles. Although Sandia served as editor of the combined report, an effort was made to honor the authors' original intent. Thus, there are minor differences in how material is presented in each section.

1.1. Problem Statement

The well documented promise of microhole drilling technology has not yet matched expectations, primarily because delivering high WOB, high torque rotational horsepower to a conventional drill bit does not easily scale down to the smaller diameter boreholes necessary to realize the cost savings. Prior work has focused on miniaturizing the various systems—such as motors, steering systems, mud handling, logging tools, and coiled tubing drilling units—used in conventional drilling technologies [1]. Although notable gains were made in these efforts, high WOB drilling technologies were relied upon at the rock/bit interface. Finger et al. [2] document the need for low WOB drilling for mineral exploration, and these methods will also be required to make microhole drilling a reality for geothermal development.

It is commonly accepted that low-cost microhole drilling, when fully embodied, will likely use coiled tube drilling (CTD) technology because a continuous umbilical to the bottom hole assembly (BHA) enables rapid hole entry and exit, continuous circulation (improving borehole integrity), and a conduit for secondary power and telemetry lines.

However, the performance of CTD systems used with miniaturized conventional drilling techniques is limited due to factors including:

- Torque resistance of the coil system
- Helical buckling in compression, and
- WOB management.

In addition, microhole drilling using CTD methods requires downhole rotation and WOB management at microhole diameters that are not commercially available.

The Department of Energy (DOE) Office of Energy Efficiency and Renewable Energy Geothermal Technology Office understands that typical geothermal exploration, reservoir assessment, and monitoring hole drilling costs are a key barrier limiting the development of geothermal reserves. A recent JASON report on Enhanced Geothermal Systems indicated that "micro drilling holds great promise because of the rapidity and reduced costs with which boreholes can be emplaced." [1]

Efforts at slimhole drilling and miniaturization in oil exploration date back to the 1950s [5]. Notable efforts in recent decades include DOE's Microhole Technology Initiative, funded by the National Energy Technology Laboratory (NETL), to explore complete drilling systems designed around microhole drilling technology. As part of these previous efforts, the Gas Technology Institute fielded a built-for-purpose coiled tubing rig for drilling exploratory and development wells [1]. Similarly, research at Los Alamos National Laboratory (LANL) [6] demonstrated the feasibility of drilling microholes to intermediate depths (~800 ft [~244 m]). These tests were performed using mechanical rotary bits and a hydraulically powered positive displacement motor (PDM) using CTD to drill a 1¾ in. (~4.5 cm) borehole. Additional tests demonstrated drilling to depths of

500 ft (~152 m) with 2⅜ in. (~6 cm) diameter microholes. This work successfully demonstrated the microhole technology.

1.2. Relevance to DOE Objectives

Drilling costs remain one of the most significant economic barriers to geothermal energy development. Sandia and its partners see an opportunity to develop low WOB drilling technologies to enable microhole technology to become a viable, cost effective method for geothermal exploration, assessment, and monitoring. This will also lower power requirements for surface equipment. Albright and Dreesen [7] estimate that cost savings of up to 70% can be achieved when routinely drilling microholes rather than conventional-sized boreholes.

1.3. Major R&D Challenges

In general, there are many technical challenges associated with the development of microhole drilling systems, but for the effort proposed herein, the primary challenges are: (i) robust, cost-effective reduced diameter rock reduction systems, (ii) compatible downhole rotation systems, and (iii) methods to control WOB in CTD applications.

1.4. Technical Risks and Mitigation

The proposed work is a major departure from the previous paradigm of miniaturizing high WOB conventional rotating drilling operations. The current project focuses on low WOB drilling technologies applied to microholes. Several challenges arise as smaller diameters are targeted for low WOB drilling technologies. For example, energy transfer efficiency in small diameter percussive hammers is different than in conventional hammers. Finding adequate methods of producing downhole rotation may prove difficult. Furthermore, the rotational requirements for percussive drilling are different than the requirements for laser-mechanical drilling. Heterogeneities in real-world geologic environments may introduce additional complications not typically found in laboratory environments. Despite the technical risks, this project capitalizes on the advantages of using drilling strategies that are inherently low WOB. This helps to mitigate the issues of drill string torsion and buckling associated with prior efforts.

Additionally, this provides more flexibility in the types of components that can be used at the ground surface and in the BHA.

1.5. Project Objectives

The primary goal of the project is to validate and establish proof-of-concept low WOB drilling technologies for microhole drilling, which can be used to lower well evaluation and monitoring costs for geothermal development. The project leverages existing DOE investments in geothermal and associated areas of research.

To meet the project objectives, the following technical issues will be addressed:

- Evaluate the technical and economic feasibility of low WOB technologies, specifically hammers and laser-mechanical systems.
- Develop downhole rotational solutions for low WOB drilling.
- Provide specifications for low WOB microhole drilling systems.
- Implement WOB control for low WOB drilling.
- Evaluate and test low WOB drilling technologies.

1.5.1. Technical and economic feasibility of low WOB technologies

A market survey will be conducted to determine the actual costs of microhole drilling using current technology. The survey will serve as the baseline for the overall project with respect to economic and technical targets. Portions of this effort will identify cost drivers for drilling and ways to reduce overall drilling costs. The economic analysis of drilling costs is discussed in Section 2.

1.5.2. Develop downhole rotational solutions for low WOB drilling

The second objective is to develop downhole rotational solutions for low WOB drilling, but before that could be done, modeling and simulation were conducted (Section 3) to bound the size of the usable holes. The ability to generate rotation downhole and control WOB will be key to the success of the project. Previous efforts at microhole drilling utilized turbines and small diameter PDMs. Sandia is also currently developing alternative downhole motors that could be used for low WOB drilling applications.

Electric motors are also an option because of the low torque requirements. The development of solutions to downhole rotational issues associated with low WOB drilling are discussed in Section 7.

1.5.3. Specify low WOB microhole drilling system

The third objective of the project is to provide design specifications for both the laboratory laser-mechanical drilling tool and the field percussive hammer drilling system. WOB and torque, as well as other operating requirements, are discussed in Section 5. The baseline design of a field deployable system utilizing the low WOB tools is provided. The BHA configuration and the surface equipment are also specified.

1.5.4. Implement WOB control for low WOB drilling

Microhole drilling will most likely employ CTD-based technologies. Although this is convenient because of the continuous conduit to the surface, controlling WOB is a challenge. Both the laser-mechanical drilling and the percussive hammer drilling will require a minimal amount of WOB. The rotational requirements are also dependent on WOB control. Implementing a robust WOB application and control scheme will be critical to the success of the project. Section 9 discusses what was implemented to control weight on the drill bit during low WOB drilling.

1.5.5. Evaluate and test low WOB drilling technologies

The final objective was to evaluate and test the low WOB drilling technologies, as discussed in Sections 4–7 and 10. Atlas Copco has a concept 2 in. (~5.1 cm) hammer that is currently in the development phase, which would be a good candidate for low WOB microhole drilling. Coring tools were also evaluated for effectiveness to meet the proposed objectives. Foro Energy designed, built, and laboratory tested a high-power optics package and prototype downhole microhole drilling tool currently targeted at an approximately 2 in. (~5.1 cm) diameter, as discussed in Section 5.

2. ECONOMIC ANALYSIS OF DRILLING COSTS

2.1. Introduction

Geothermal resources provide an opportunity for clean, renewable base load energy in the U.S. and worldwide. The current utilization of available resources is only a fraction of the potential supply. One of the primary obstacles to increasing the use of geothermal energy is developing those resources in a cost-effective manner. A JASON report on Enhanced Geothermal Systems published in 2013 indicated that "micro drilling holds great promise because of the rapidity and reduced costs with which boreholes can be emplaced." [1]

Drilling costs associated with exploration and reservoir assessment are a barrier limiting the development of geothermal reserves. Typical exploration requires drilling large-diameter production-sized wells that cost nearly $2.5-~5.0M per well for depths up to 2500m [2]. By using slimhole technology, the cost to drill exploration wells can be reduced 40–60%, while the cost to drill production and injection wells can be reduced 25–40% [3]. The large diameter boreholes currently used in geothermal exploration have large upfront capital expenses, and slimholes provide the opportunity to lower those early exploratory costs.

The notion of drilling smaller boreholes has been around since the 1950s when efforts at slimhole drilling and miniaturization were investigated for oil exploration [4]. Previous work drilling smaller holes has shown cost savings up to 30–40% over conventional drilling, and Albright and Dreesen (2000) estimate savings of up to 70% when routinely drilling microholes rather than conventional-sized boreholes. Not only will microhole technology lower costs for drilling exploration and monitoring holes, but it will also improve access to data by enabling the drilling of more monitoring holes at a lower cost.

Although there is no formal definition of microhole drilling, it is typically considered as boreholes less than 5 in. (12.7 cm) in diameter [6]. Slimhole drilling, on the other hand, produces boreholes with a slightly larger diameter than microholes but still smaller than conventional boreholes. Figure 2-1 illustrates the relative size differences between conventional, slimhole, and microhole boreholes. In the mid-2000s, NETL began to

explore complete drilling systems designed around microhole technology, and previous work includes DOE's Microhole Technology Initiative funded by NETL.

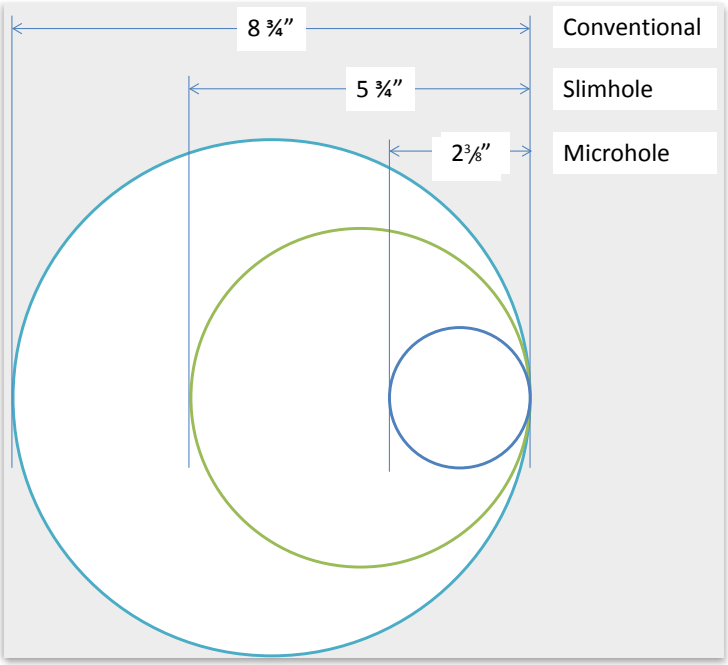

Figure 2-1. Relative sizes of boreholes used in drilling

2.2. Cost Drivers

The scale reduction and lower costs become attractive at the microhole level as shown in Table 2-1. Microholes offer direct cost savings through reduced material costs, fluid volumes, and drill pipe requirements. Cost savings are also realized through the use of smaller drilling/workover rigs (lower daily costs) and smaller surface footprints (100K ft-2 vs. 35K ft2 [~30.5K m2 vs. ~10.7K m2]) [7]. Additional cost savings include lower fuel costs associated with smaller auxiliary equipment that require less fuel and other costs directly linked to borehole size.

Table 2-1. Scaling Gains (adapted from [5])

Hole Type	Hole Size (in.)[1]	Drill Pipe OD[2] (in.)[1]	System Capacity (bbls/1,000ft)[3]	Fluid Capacity Ratio	Pipe Weight (lbs/100ft)[3]	Weight Ratio
Microhole	1.38 2.00	0.75 1.25	1.7 3.3	40 19	580 1,500	29 11
Slimhole	4.00 5.88	2.88 3.50	13.3 29.1	5.2 2.4	6,850 13,300	2.4 1.2
Conventional O&G	6.13 8.75	3.50 4.50	32.0 68.9	2.2 1.0	13,300 16,600	1.2 1.0

[1] Multiply in. by 2.54 to obtain cm

[2] OD is outer diameter

[3] Multiply ft by 0.305 to obtain m

Randolph [4] provided a similar comparison of conventional versus slimhole drilling as shown in Table 2-2.

Table 2-2. Conventional vs. Slimhole Rigs with 5,000 ft (1,520 m) Drilling Capability [4]

Type of Rig	Conventional	Slimhole
Hole diameter	8.5	3–4
Drill string weight (tons)[1]	40	5–7
Rig weight (tons)	65	12
Drill site area (%)	100	25
Installed power (kW)	350	75–100
Mud pump power (kW)	300	45–90
Mud tank capacity (bbl)	470	30
Hole volume (bbl/1,000 ft)[2]	60	6–12

[1] Multiply tons by 0.907 to obtain metric tons

[2] Multiply ft by 0.305 to obtain m

McLaughin [9] normalized the costs of drilling activities with respect to borehole size to define a cost factor associated with borehole diameter as a function of daily rig cost, depth cost, and casing cost as shown in Figure 2-2–Figure 2-2.

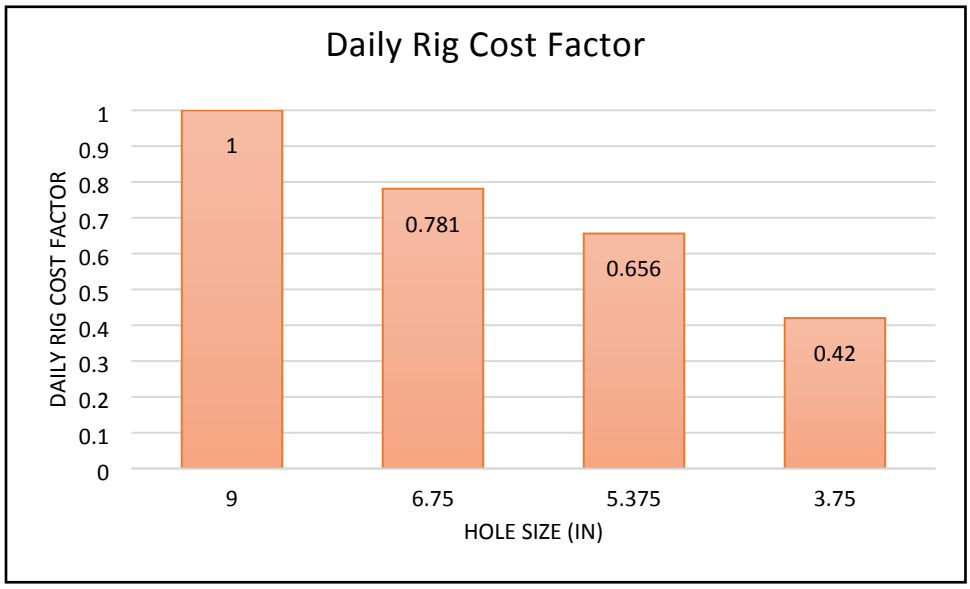

Figure 2-2. Daily rig cost factor [9]

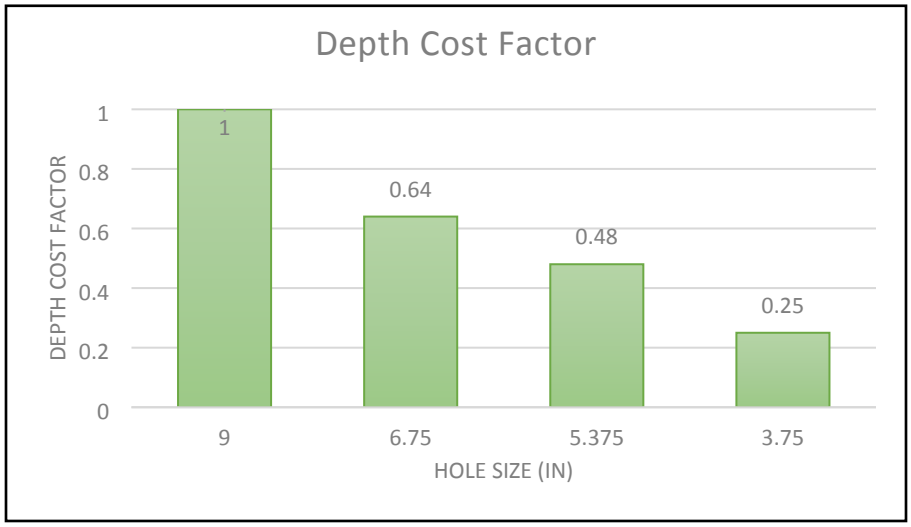

Figure 2-3. Depth cost factor [9]

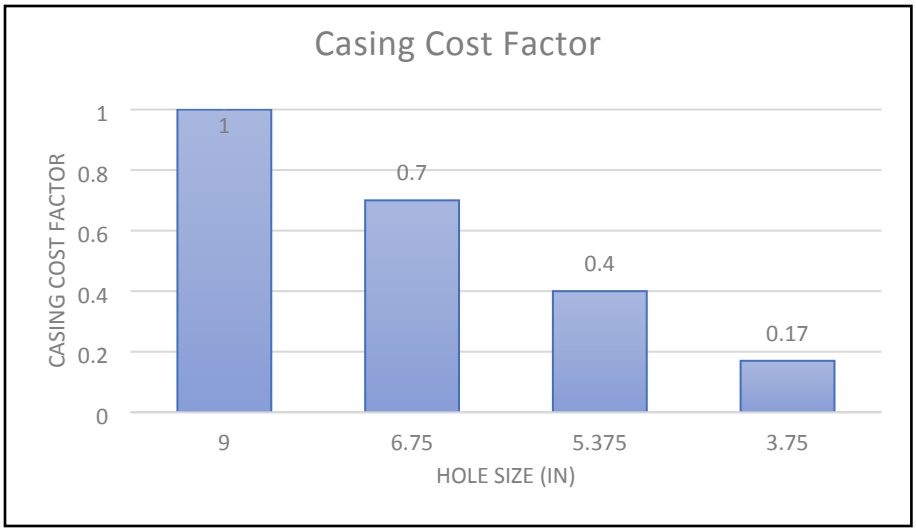

Figure 2-4. Casing cost factor [9]

Data compiled by Spears & Associates [7] further illustrates the potential cost savings of using coiled tubing for microhole drilling compared to conventional drilling (Table 2-3). Although not a direct comparison between drilling applications, the "other" column highlights the difference between the ancillary costs and "fixed" costs (e.g., operator and drill pipe) for small diameter borehole drilling.

Table 2-3. Cost per foot for a 3,000-ft (914.4-m) well in Canada [7]

Region	Contractor	Pipe	Other	Total
Rotary	$15	$5	$23	$43
Coiled Tubing	$15	$4	$14	$33

2.3. Conclusion

Based on the literature review of slimhole/microhole drilling and various case studies, the potential economic benefits associated with drilling smaller diameter boreholes for exploration and workover is evident. However, the technology has seen limited commercial success due, in part, to challenges associated with drilling smaller diameter boreholes. The cost benefits have been insufficient to overcome the practical limitations.

Limited data is available in the literature regarding actual microhole drilling costs. Specifying a cost per foot for the DOE Geothermal Technology Program microhole drilling program will be challenging since the goal of the project is to develop enabling technologies rather than a complete system. However, the program's goal is to be competitive with microhole coiled tubing drilling operations attempted in the past by evaluating comparable drilling scenarios using the relative Cost Factor approach.

2.4. References for Executive Summary and Sections 1 and 2

[1] Jeanloz, R., and H. Stone, Enhanced Geothermal Systems, JASON, JSR-13-320. The Mitre Corporation, McLean, Virginia, December 2013.

[2] Lowry, Thomas Stephen, Finger, John T., Carrigan, Charles R., Foris, Adam, Kennedy, Mack B., Corbet, Thomas F., Doughty, Christine A., Pye, Steven, & Sonnenthal, Eric L. GeoVision Analysis: Reservoir Maintenance and Development Task Force Report (GeoVision Analysis Supporting Task Force Report : Reservoir Maintenance and Development). United States. https://doi.org/10.2172/1394062.

[3] Zhu, T., and H.B. Carroll, Slimhole Drilling: Applications and Improvements, NIPER/BDM-0155. U.S. Department of Energy, Bartlesville, Oklahoma, August 1995.

[4] Randolph, S., J. Bosio, and B. Boyington, Slimhole Drilling: The Story So Far. *Oilfield Review*, 1991, p. 46–54.

[5] Albright, J.N., and D.S. Dreesen, "Microhole technology lowers reservoir exploration, characterization costs," *Oil & Gas Journal*, 98(2) (January 2000).

[6] Long, R. Slimhole vs. Microhole: Future of E&P. In 2005 Society of Petroleum Engineers (SPE) Annual Technical Conference & Exhibition (ATCE). 2005.

[7] Spears & Associates, Microdrill Initiative Initial Market Evaluation, DOE/SW/54387-1. National Petroleum Technology Office, Tulsa, Oklahoma, July 2003.

[8] NETL, Microhole Technology: A Systems Approach to Mature Resource Development. 2006. DOE National Energy Technology Laboratory.

[9] McLaughlin, P.L. 1959. Reassessing the Merit of Small-Diameter Drill Holes. In Ninth Annual Drilling Symposium, held in University Park, Pennsylvania, October 8–10, 1959. Pennsylvania State University, College of Mineral Industries, University Park, Pennsylvania.

3. GEOTHERMAL RESOURCE EVALUATION USING MICROHOLES

This section was prepared by Geothermal Resources Group.

3.1. Summary

Drilling cost is the most significant impediment to geothermal exploration and development for power generation. Despite efforts to the contrary, the cost of drilling production-sized geothermal wells continues to rise. Drilling smaller diameter wells is significantly less expensive. The implementation of slimhole drilling and well testing in the 1990s successfully reduced the cost of resource development in some locations, but it had limitations in cases of greater depth, lower temperature, and lower permeability. Drilling microholes—boreholes with bottom hole diameters less than about 5 cm (2 in.)—could further reduce exploration drilling costs, but alternative well test methods may be required.

We conducted borehole simulations to determine the flow rate at which a particular borehole size and resource condition would prevent flow to the surface. The simulations presented in this section demonstrate that using conventional techniques, such as production and injection tests, to characterize reservoir performance have limitations for scaling microhole test results to production-sized boreholes. In smaller boreholes, the ability to conduct a production test is heavily dependent on enthalpy and the productivity index (PI). Injection tests quickly reach the capacity of pumping equipment or the limits of casing shoe pressure before significant injection rates are achieved.

Alternative techniques, including drill stem tests and in situ chemical analysis, can be used to evaluate microholes if a surface discharge test is not possible due to low temperature, low permeability, or small well diameter. In situ analysis could eliminate delays experienced waiting for the results of conventional laboratory analyses. Replacing the surface discharge test also negates the need for large and costly flow test equipment installation and operation; reduces safety risks; and eliminates environmental impacts related to atmospheric emission of gas and aerosols, water storage, diesel-power pumping, and transportation.

3.2. Introduction

Drilling cost is the most significant impediment to geothermal development for power generation. The typical cost of a 2,000 m (~6,560 ft), 8½ in. (~21.6 cm) bottom hole diameter geothermal well is approximately $3M–$6M (Silverman et al., 2014). Despite concerted efforts by the geothermal industry to improve drilling efficiency and reduce cost, the latter continues to rise, often at rates exceeding the Consumer Price Index (Mansure and Blankenship, 2013).

Garg and Combs (1993) proposed the use of slimholes for geothermal exploration. Although the industry was slow to adopt this method, slimholes are now commonly drilled to evaluate geothermal resource potential (e.g., Osborn et al., 2014). A critical assumption in using a surrogate slimhole is that test results can be accurately scaled up to the larger, more expensive production boreholes completed upon successful discovery of a proven geothermal resource.

Smaller diameter boreholes can be drilled at one-half to one-third the cost of a conventional 8½ in. (~21.6 cm) diameter completion (Tuttle et al., 2010) due to reductions in most major cost factors, including site preparation, mobilization and demobilization, daily drill rig costs, number of personnel, bits, casing, and cementing. Diamond core rigs are capable of drilling to depths greater than 3 km using 75.7 mm (3 in.) NQ core rod and to greater than 4 km using 60 mm (2.36 in.) BQ core rod. Smaller 48 mm (1.9 in.) AQ core rod is also commercially available. Microholes have become an attractive alternative due to the significant technological advancements in instrument miniaturization and durability in the 20 years since the introduction of slimhole technology. However, drilling deep small diameter microholes using coring technology can be problematic. The DOE and others are currently pursuing advanced drilling techniques—including the use of lasers, percussive hammers, and microwaves—that have the potential to drill deep microholes at substantially lower cost and risk.

Geothermal exploration wells are typically evaluated by discharging the well to surface equipment at atmospheric pressure to measure flow rate, enthalpy, and fluid composition. Reservoir characteristics are further evaluated by conducting step-rate production and/or injection tests and pressure recovery measurements. This equipment

typically consists of a flow line, James tube, atmospheric separator, weir box, and instrumentation. However, low temperature resources or small diameter boreholes are often incapable of continuous, unassisted flow. In such cases, flow to the surface can sometimes be induced or temporarily maintained by air- or nitrogen-lift or assisted by pumping, but these methods add significant cost and complexity to the test operation. In addition, atmospheric flow tests require relatively large liquid storage facilities (e.g., sumps or tanks) or a nearby injection well, and their use may be limited due to steam and gas emissions, hazardous liquid generation, or water disposal restrictions.

3.3. Borehole Flow Limitations

A parametric study was conducted to determine borehole flow limitations. A hypothetical geothermal slimhole was used as a basis for the study. Parameters included depth, borehole diameter, enthalpy, PI, and flow rate. A matrix was constructed using the results of numerous borehole simulations. Two depths were studied, 914 m (3,000 ft) and 1,829 m (6,000 ft). Borehole diameters ranged from 4.6–12.7 cm (1.8 in.–5.0 in.), productivity indexes ranged from 2.1–25 TPH/bar (0.3–4.0 MTPH/psi), and enthalpy ranged from 814–2,791 kJ/kg (350–1,200 BTU/lbm). For both boreholes, casing was set and cemented at 609 m (2,000 ft). The casing diameter is assumed to be one standard size larger than the open borehole diameter. For each simulation, a choke rate was determined for combinations of these three variables (i.e., borehole diameter, PI, and enthalpy). Choke rate represents the flow rate at which the well will no longer sustain flow.

3.3.1. Shallow Borehole (914 m)

The resulting data set is visualized as isosurfaces of choke rate conditions at various flow rates (Figure 3-1). In these visualizations, isosurfaces are constructed at arbitrary and regularly spaced intervals from 23 to 113 TPH (50 to 250 MTPH) to represent the conditions under which choked flow occurs. Smaller diameter boreholes experience choked conditions at lower flow rates and have a lower maximum flow for any given enthalpy. Generally, fluids with relatively high or low enthalpy, choke at a lower maximum rate than moderate enthalpy wells.

Isosurfaces for smaller diameter boreholes show less variation in PI (i.e., the leading edge of the isosurface is nearly parallel to the PI axis), while larger borehole diameters show appreciable variation in PI (Figure 3-2). This is because friction pressure becomes the dominant variable at smaller borehole diameters. This shows that flowing conditions in these small diameter boreholes are not sensitive to PI such that the test results are not useful for scaling borehole performance to larger borehole diameters because the indicated PI yields a nonunique solution. For larger bottom hole diameters, there is a significant sensitivity to PI (Figure 3-3). Borehole diameter and enthalpy data pairs located to the right of an isosurface have enough variability in PI to allow unique solutions when scaling up borehole performance to larger diameters. To better visualize the limiting PI factor, the isosurfaces shown in Figure 3-1 are replotted in Figure 3-4 to exclude data points for enthalpies greater than 1,744 kJ/kg (750 BTU/lbm). The top edges of each isosurface at constant enthalpy clearly shows the lack of variability in PI for smaller boreholes and the relatively large change in PI for larger boreholes. Similarly, Figure 3-5 shows only the data points for enthalpy of 1,744 kJ/kg (750 BTU/lbm) and the progressive increase in PI variability from smaller to larger borehole sizes.

In Figure 3-6, the isosurfaces shown in Figure 3-1 are rotated so the effects of borehole size and enthalpy are more prominent. This shows that at smaller borehole sizes enthalpy has a slightly greater impact on flow rate with a flattening of the surfaces relative to the larger borehole sizes. The effect is greater for lower enthalpy than higher enthalpy. Moderate enthalpy wells with two-phase flow experience choked flow at high flow rates and are thus more likely to be successfully flow-tested by smaller borehole exploration wells.

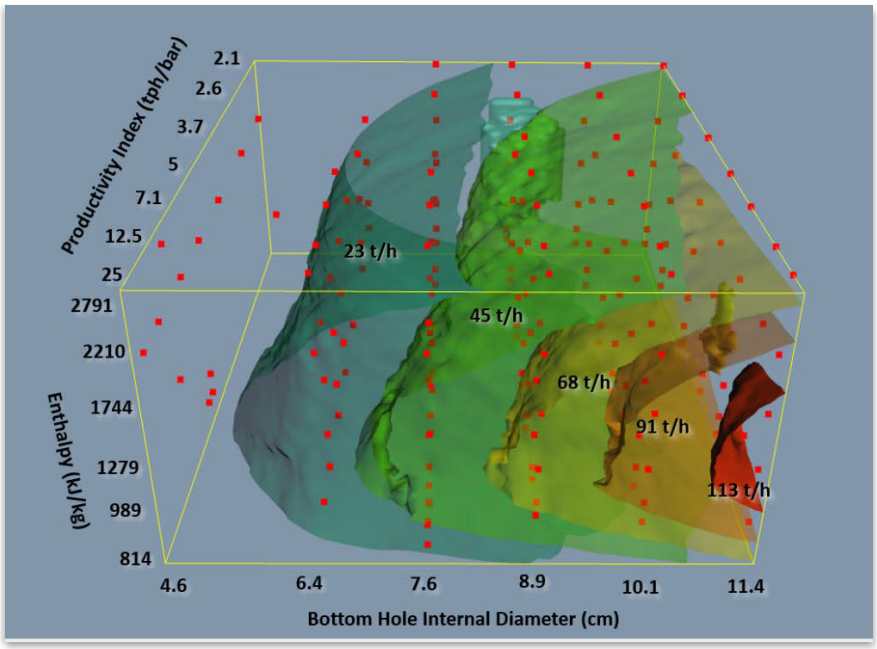

Figure 3-1. Isosurfaces of choke rate in TPH (shown as t/h in the figure) in a 914 m (3,000 ft) borehole based on simulated variation in borehole size (x-axis), PI (y-axis), and enthalpy (z-axis)

Red squares represent individual borehole simulations located by the three simulation variables of borehole size, enthalpy, and PI. Points to the left (or above and below) each isosurface represent conditions under which the well is choked and will not flow, while points to the right of or within the isosurface represent flowing conditions. Light green on the back isosurface is an artifact of the contouring. Red squares in all figures represent simulation data points.

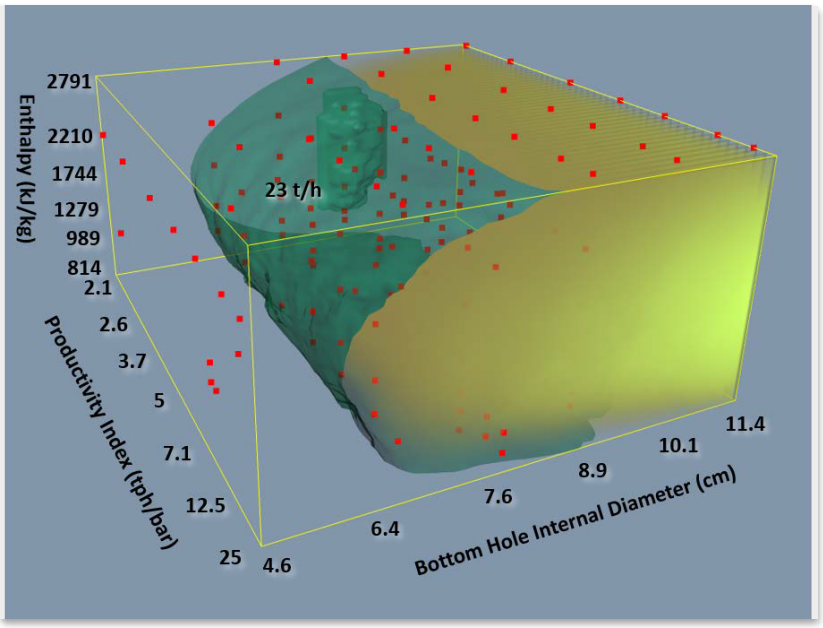

Figure 3-2. A single isosurface at a choke rate of 23 TPH for a 914 m (3,000 ft) borehole

All points in the yellow shaded area represent conditions that will allow flow. Note that the choke isosurface at the smallest borehole diameter is nearly parallel to the PI.

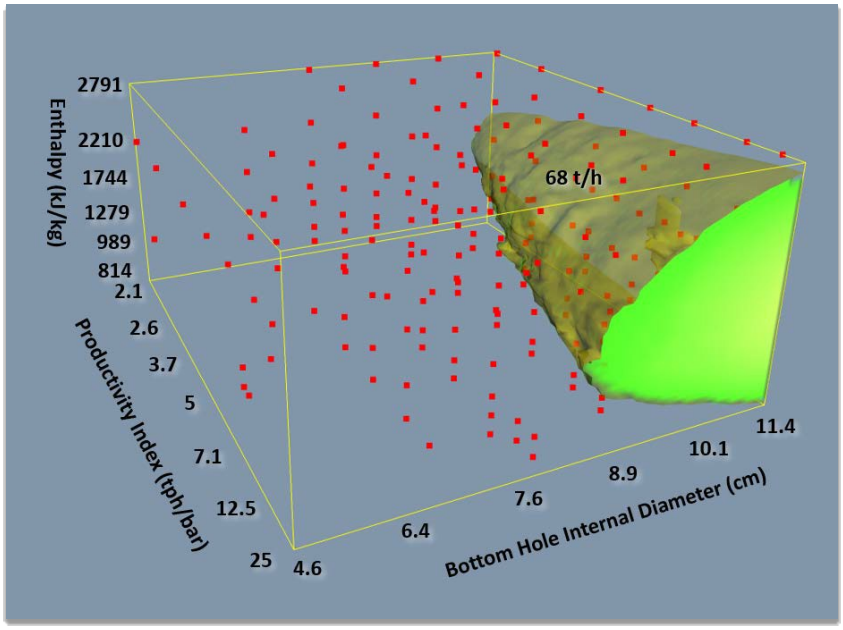

Figure 3-3. An isosurface at a choke rate of 68 TPH (shown as t/h in the figure) for a 914 m (3,000 ft) borehole

The choke isosurface at the smallest borehole diameters is not parallel with the PI axis, unlike Figure 3-2, which indicates sufficient sensitivity to borehole diameter and enthalpy under these conditions to allow test results to be scaled up to larger borehole diameters.

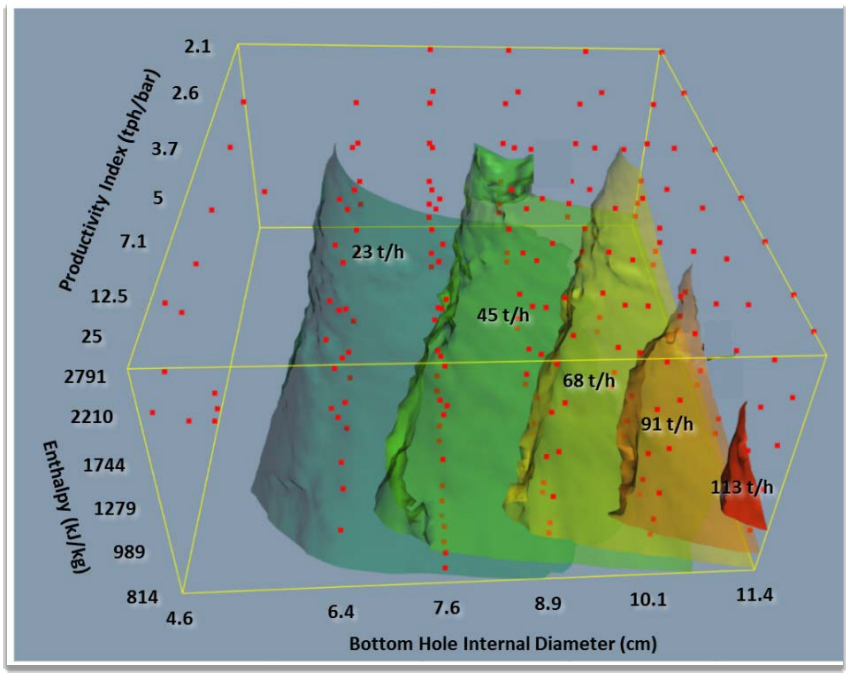

Figure 3-4. Isosurfaces of choke rate in TPH (shown as t/h in the figure) for a 914 m (3,000 ft) borehole, excluding enthalpy greater than 1,744 kJ/kg (750 BTU/lbm), showing sensitivity to enthalpy and borehole diameter

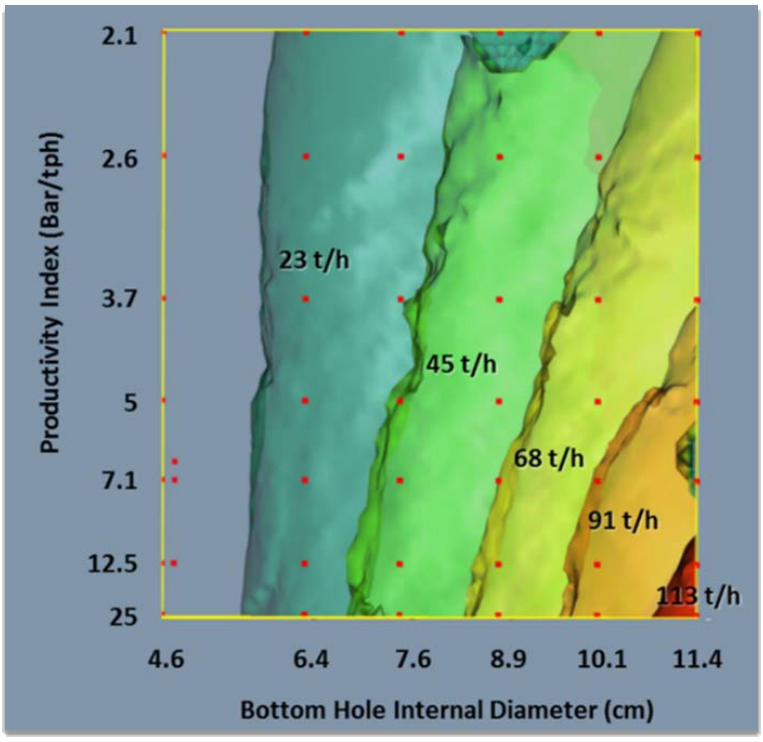

Figure 3-5. Isosurfaces of choke rate in TPH (shown as t/h in the figure) as a function of PI and borehole diameter for a range of flow rates for 914 m (3,000 ft) borehole with a flowing enthalpy of 1,744 kJ/kg (750 BTU/lbm), showing sensitivity to borehole diameter and PI

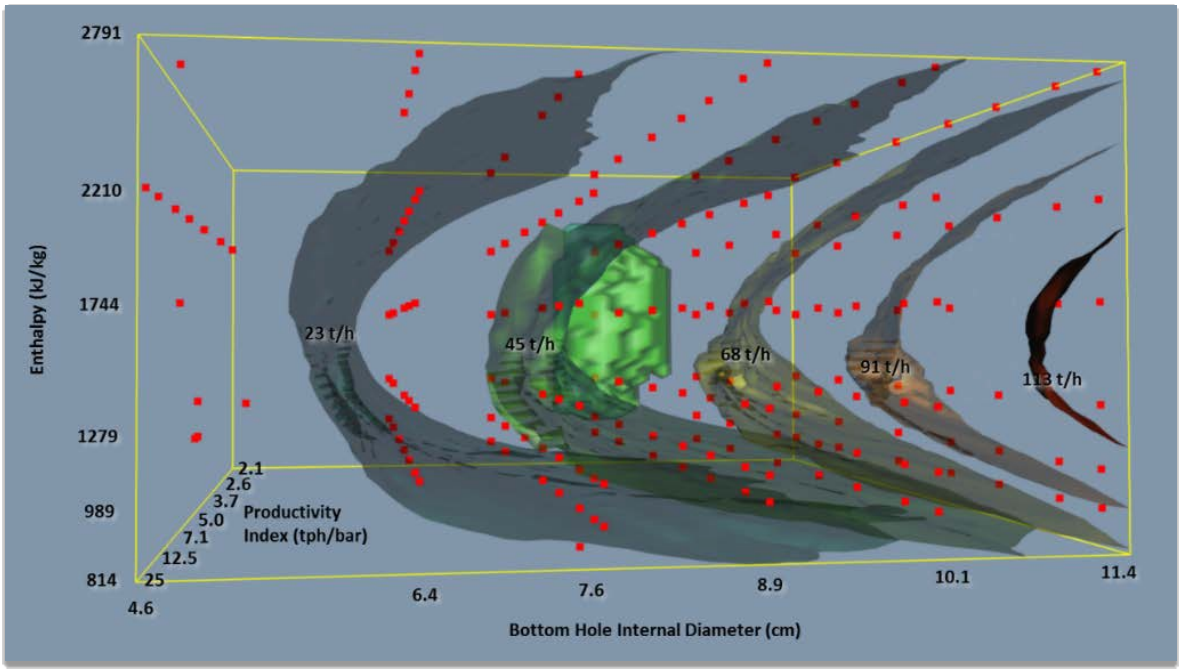

Figure 3-6. Isosurfaces of choke rate in TPH (shown as t/h in the figure) from a 914 m (3,000 ft) borehole based on simulated variation in hole size (x-axis), PI (y-axis) and enthalpy (z-axis)

Light green on the back surface is an artifact of the isosurface contouring. Red squares in all figures represent simulation data points. Figure 3-6 shows the sensitivity of the isosurfaces to enthalpy and that moderate enthalpy fluids can sustain flow in much smaller boreholes, whereas cooler, lower enthalpy fluids do not have sufficient energy to overcome friction pressure, and higher flash enthalpies choke due to expanded volume.

In theory, measurements of well and reservoir performance for slimholes can be scaled up to larger production boreholes for geothermal development. However, at constant enthalpy, especially for small borehole sizes, a wide range in PI produces choke flows at essentially the same flow rate. This demonstrates that friction pressure is the dominant control on flow rate and that the performance of progressively smaller boreholes is increasingly less suitable for scaling up to larger diameters. This is most apparent for 6.4 cm (2.5 in.) diameter boreholes, whereas 7.6 cm (3 in.) boreholes show enough variation to allow scaling up with reasonable accuracy, and 10.1 cm (4.0 in.) and 12.7 cm (5.0 in.) boreholes have even greater accuracy. Thus, boreholes less than 7.6 cm (3 in.) do not show sufficient variation in PI to allow accurate scaling to production-sized boreholes.

3.3.2. Deep Borehole (1,829 m)

The analysis discussed above for a 914 m (3,000 ft) borehole was repeated for an 1,829 m (6,000 ft) borehole. This configuration can accommodate a large range of enthalpies (Figure 3-7). Boreholes sizes from 4.6 cm to 7.6 cm (1.8 in. to 3.5 in.) showed negligible variation in PI at lower flow rates (Figure 3-8), indicating that flow test parameters for these borehole sizes are not useful for scaling up to larger diameter wells. For this depth, borehole sizes should be at least 11.4 cm (4.5 in.) to allow accurate scaling to production-sized boreholes. This confirms that smaller microholes will require a different method to determine PI or permeability.

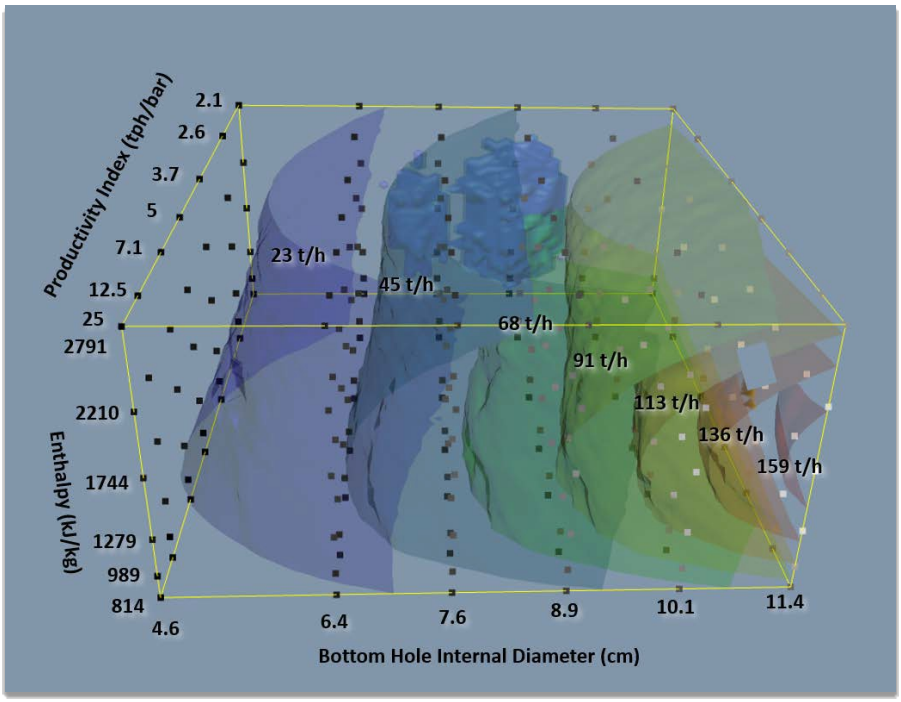

Figure 3-7. Isosurfaces of choke flow for an 1,829 m (6,000 ft) borehole showing sensitivity to enthalpy, PI, and borehole diameter

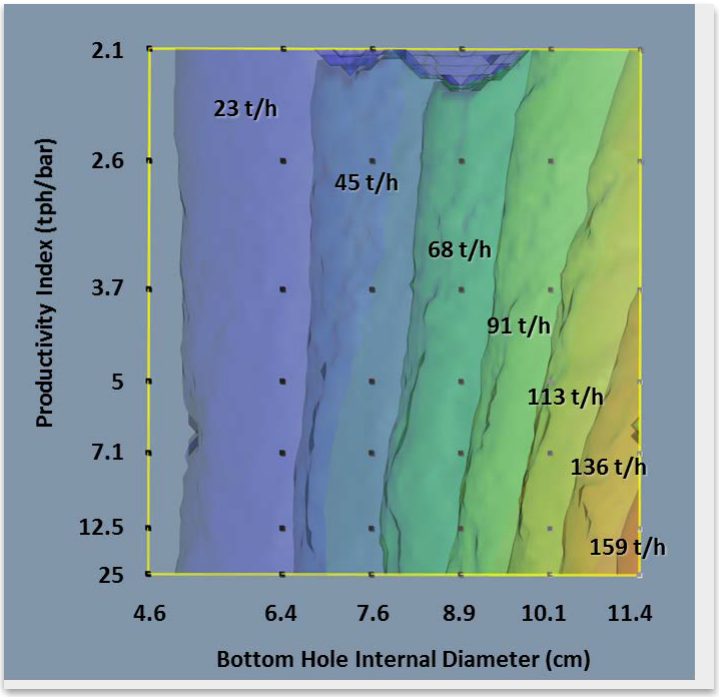

Figure 3-8. Choke flow as a function of PI and borehole diameter for a range of flow rates for an 1,829 m (6,000 ft) borehole, cropped to eliminate results for enthalpy greater than 1,744 kJ/kg (750 BTU/lbm), showing sensitivity to borehole diameter and PI

3.3.3. Temperature and Pressure

Fiber optic distributed temperature sensing (DTS) is commercially available and now commonly used in geothermal applications.[1] These instruments can continuously measure temperature over the entire length of the borehole to temperatures in excess of 1,000 ° C (1,832 ° F). Housed in ¼ in. (~0.64 cm) capillary tubing, these instruments can be easily deployed in a microhole.

Distributed pressure sensing is also commercially available, but systems are unstable. Instead, a commercially available strain gauge pressure sensor can be deployed on the end of a DTS assembly for continuous pressure measurement.

3.3.4. Injection Testing

Injection tests are routinely conducted in most geothermal wells immediately after drilling is completed, including when slimholes are used. Injection tests using a drilling rig can be conducted quickly at relatively low cost because the required equipment is usually part of the standard drilling package. The injection test is usually performed with a single phase ambient temperature liquid, so fluid enthalpy is essentially constant, and only PI and borehole diameter are significant variables.

To assess the feasibility of conducting injection tests in microholes, we simulated injection into an 1,829 m (6,000 ft) borehole with varying borehole diameters, assuming high and low permeabilities. Achieving sufficient wellhead pressure is the most important factor for a useful test. Injection tests are typically conducted at pressures less than 35 bar (500 psi) but can be completed at pressures over 100 bar (1,450 psi) with typical drill rig pumping equipment. However, higher pressures may not be possible due to pumping equipment limitations and may increase the risk of breaking the casing shoe and damaging well integrity.

The results show that for a 4.6 cm (1.8 in.) borehole, wellhead pressure increases rapidly at very low flow rates, quickly exceeding the pressure achievable with typical pumping

[1] https://www.slb.com/
https://web-material3.yokogawa.com/BU39J06B45-01E_006.pdf
http://www.ozoptics.com/ALLNEW_PDF/DTS0127.pdf

equipment (Figure 3-9). The feasibility of injection testing in a high permeability formation increases as borehole size increases. It is feasible with a borehole diameter of 7.6 cm (3 in.) and even easier at larger diameters. For the low permeability simulation (Figure 3-10), none of the borehole sizes showed sufficient variation in flow rate to provide useful test results, and the 4.6 cm (1.8 in.) borehole performed the worst.

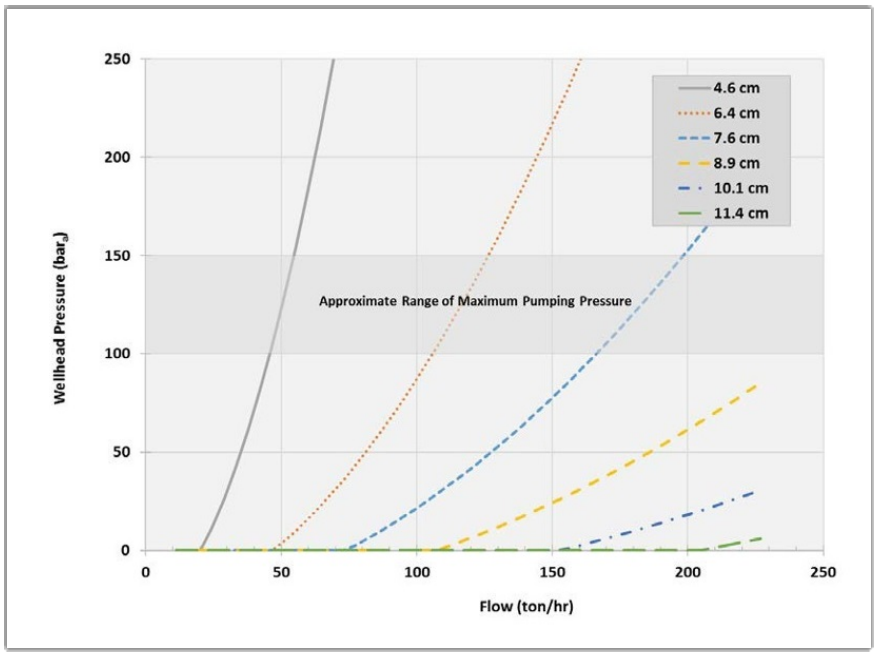

Figure 3-9. Injectivity in an 1,829 m (6,000 ft) borehole with varying hole diameter, assuming high permeability; the approximate range of maximum pumping pressure is based on pumping equipment and casing shoe limitations

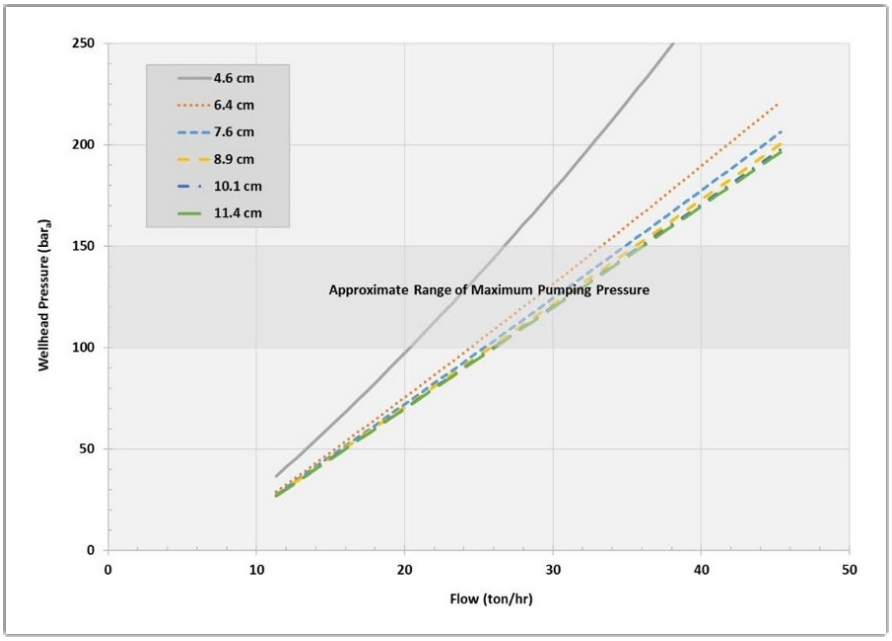

Figure 3-10. Injectivity in an 1,829 m (6,000 ft) borehole with varying hole diameter, assuming low permeability (note lower flow range); the approximate range of maximum pumping pressure is based on pumping equipment and casing shoe limitations

3.3.5. Drill Stem Testing

The previous simulations demonstrated that productivity and injectivity indexes from microhole production or injection tests have limitations for scaling up to the potential performance of larger production-sized boreholes. Thus, to effectively use microholes, an alternate method is needed to assess well and reservoir performance. A downhole test—possibly a drill stem test (DST)—is required to avoid the dominant friction factor that influences microhole testing. A DST is a temporary completion of a borehole, typically used in the oil and gas industry, to determine whether the well should be completed at the currently drilled depth. Using a DST tool deployed on a drill string or wireline, the geologic zone in question is sealed off from the rest of the borehole by packers. The tool is then remotely activated to allow borehole flow into the tool while pressure, temperature, and other conditions are recorded. Data obtained from a DST include:

- Fluid samples,
- Reservoir pressure (P*),

- Formation properties including permeability (k), skin (S), and radius of investigation (ri),
- Productivity estimates including flow rate (Q), and
- Hydrodynamic information.

A DST moves the flow control and measurements downhole, largely eliminating frictional pressure. While bottom hole pressures can be determined from surface testing, the deeper flow control causes borehole effects to diminish and allows for a test with less flow, not necessarily to the ground surface. The potential elimination of flow to the ground surface negates the need for large, expensive flow test equipment.

The DST has long been used in oil and gas applications but not in the geothermal industry. DST tool temperature limitations and the difficulty of zone isolation (i.e., using downhole packers) in fractured reservoirs has limited the implementation of this technique in geothermal applications. Pressure transient testing techniques, typically applied to high volume surface flow data, can also be applied to the smaller flow volumes produced by a DST.

Pressure transient testing is not used frequently in geothermal applications due to phase changes that occur in geothermal fluid flow. The storage component is difficult to calculate, and the storage period is too long in most geothermal wells, masking the critical early time data, often preventing a definitive analysis in a normal surface test. A DST performed at elevated temperature could solve the borehole storage and phase problems in geothermal applications, which occur due to the large borehole volumes, frictional pressure drop, and pressure gradient. With the DST tool emplaced downhole where lower drawdown and higher pressures exist, the geothermal fluids will usually be single-phase liquids. Even in two-phase reservoirs, the steam fraction typically does not change significantly. With these more stable conditions, pressure transient analysis can be used to determine typical parameters, including reservoir pressure, permeability, skin, and estimated productivity.

Currently available DST tools are rated to about 175 ° C (350 ° F); high temperature tools are rated to 210 ° C (410 ° F); and premium seals are rated to up to 230 ° C (450

° F) (Figure 3-11). By applying sealing technologies from other high-temperature tools, such as drill bits and downhole sampling devices, it may be feasible to manufacture a tool rated to temperatures over 300 ° C (572 ° F), which would accommodate most geothermal wells. The DST tool can also be installed at shallower depths in lower temperature zones to avoid excessive temperatures. In addition, placing the DST tool in a cased hole significantly improves the likelihood of successful zone isolation because open-hole packers have less efficient sealing capability.

DST tools are available for a minimum borehole size of 8.9 cm (3.5 in.). This can serve as a prototype to test in larger microholes, greatly improving the analysis for those holes. If successful, the tool size could be reduced to fit smaller microhole diameters where the DST would be the only viable flow analysis tool. The smaller size would require redesign, so it may be possible to add additional measurements into the tool, such as the instrumentation discussed in the next section to aid in geothermal microhole well evaluation.

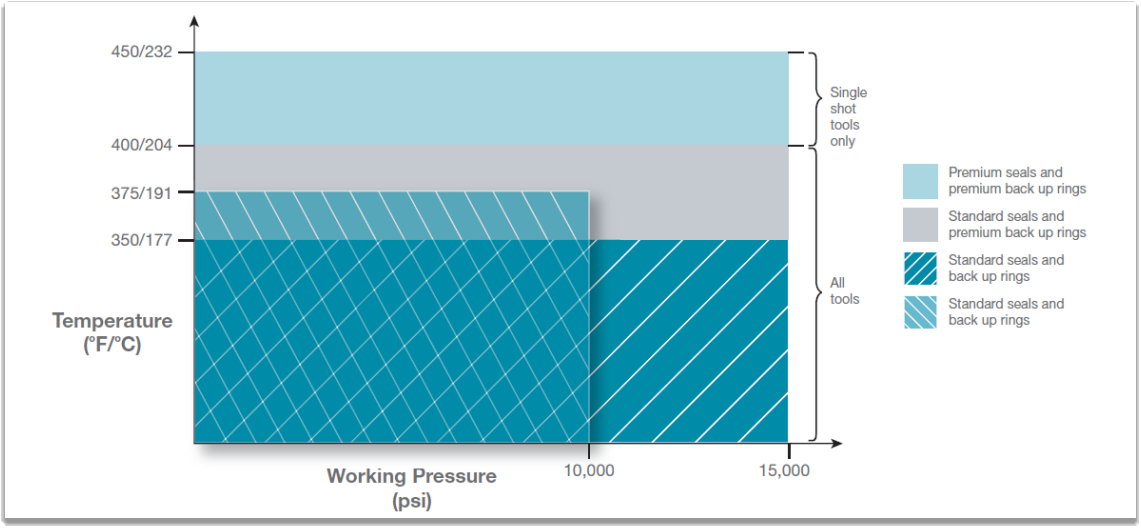

Figure 3-11. Operating ranges of current DST tools (Expro, 2016[2])

[2] https://www.exprogroup.com/

3.4. Instrumentation for Microhole Evaluation without Surface Discharge

In addition to the measurement and analysis of flow, enthalpy, PI, and permeability derived from a flowing (surface or downhole) test, it is also essential to measure several other borehole and resource parameters, including temperature, pressure, and fluid composition. These parameters are necessary for pressure transient analysis and reconstruction of reservoir fluid composition. While some methods are already commercially available for deployment in microholes, others will require modification for deployment at high temperatures and pressures and smaller hole sizes. The parameters typically recorded in geothermal well tests are listed in Table 3-1.

Table 3-1. Geothermal Well Measurement Parameters

PARAMETERS	
temperature	Potassium
pressure	Calcium
pH	Magnesium
conductivity	Silica
carbon (CO_2, HCO_3, etc.)	Sulfur
chloride	stable isotopes of water ($\delta^{18}O$, δD)
sodium	noble gas isotopes ($^{3/4}He$)

3.4.1. Fluid Composition

In the absence of a surface discharge sample, fluid composition can be measured using a downhole sampling tool to collect a sample or by taking an in-situ measurement in the borehole. Although downhole sampling tools have been commercially available for many years, their use has not been widely adopted. Significant time and expense is required to deploy and retrieve the sampler, and the single samples retrieved from each sampling run are often of questionable quality. However, DST tools used in the oil and gas industry are often equipped with fluid sampling chambers. Expanding the use of DST tools for geothermal applications will likely lead to improvements in downhole sampling success. Nevertheless, collection of downhole samples requires that the fluid be removed from the high pressure, high temperature environment downhole to the ground surface, resulting in changes in liquid to vapor ratio, fluid composition (i.e., pH), and mineral precipitation (e.g., SiO_2).

In-situ measurement of fluid composition offers the potential for continuous measurement of the parameters of interest. Continuous measurements can help identify when contaminated fluids introduced during the drilling process have been removed by subsurface fluid migration. Chevron developed a downhole laboratory tool (now owned by Schlumberger) that measures temperature, pressure, pH, conductivity, carbon

dioxide, fluorescence, and hydrocarbon concentrations.[3] Currently, this tool has a temperature limit of 177 ° C (350 ° F) and a 5.5 in. (~14 cm) OD, so it cannot be used in slimholes.

3.4.1.1. Instrument Power and Memory

Sandia has successfully tested flash memory modules to 225 ° C (437 ° F) for 1,000 hr (Cashion, 2015); demonstrated solid tantalum capacitors to 260 ° C (500 ° F) for 1,000 hr; and tested printed circuit boards. Commercialization of these components is essential to allow extended deployment of analytical measurement tools in deep, high temperature boreholes for continuous measurements during flow tests.

3.4.1.2. pH and Conductivity

Accurate measurement of pH is essential for determining speciation in geothermal solutions and in turn, for understanding reservoir connectivity and assessing the scaling and corrosion potential in brine processing for power generation. Measurement of pH in samples collected at the surface is inherently problematic because exsolution of CO_2 from a grab sample begins immediately and continues until the measurement has been completed. It is possible to conduct inline analysis of pH from a surface discharge test, but this requires relatively complicated equipment.[4] Therefore, most geochemists rely on rapid analysis of grab samples collected at the surface, thereby introducing considerable error into geochemical data analysis.

Instruments are commercially available for measuring pH and conductivity to temperatures of 343 ° C (650 ° F) and 35 MPa (5,100 psi).[5] Such instruments have been deployed to measure conditions in mid-ocean ridge vents for many years (Ding and Seyfried, 2007) but will require additional development to allow deployment in the subsurface environment.

---

[3] https://www.slb.com/~/media/Files/resources/oilfield_review/ors09/win09/04_downhole_fluids_laboratory.pdf

[4] https://web-material3.yokogawa.com/BU39J06B45-01E_006.pdf

[5] http://www.corrinstruments.com/High_T_High_P_Probes/H_T_H_P_probes.html

Conductivity is produced by the presence of charged ions in solution and therefore can be used as a surrogate for determining aqueous salinity. Noncontact high temperature, high pressure conductivity sensors are readily available and can handle the temperature and pressure ranges found in geothermal environments.

3.4.1.3. Carbon Dioxide

Continuous measurement of aqueous CO_2 concentrations at low temperatures and pressures is currently possible using a small, cable-deployed infrared gas analyzer as demonstrated by Johnson et al. (2010). Their device—contained in a 2 cm diameter, 15 cm long PTFE housing—has been used to measure relatively low concentrations of CO_2 at low temperatures, but they report that the infrared analyzer can be calibrated for CO_2 concentrations as high as 200,000 ppm CO_2, which is sufficient for most geothermal applications, but it has a temperature range up to only 60 ° C (140 ° F). However, the instrument requires correction for pressure and temperature relative to calibration conditions, and this correction would be significant for geothermal conditions.

3.4.1.4. Chloride Concentration

Chloride ion selective electrodes are common in laboratory applications. More recently, all-solid- state chloride sensors have been developed (Gao et al., 2010). The authors report that their device—small enough to fit in a microhole—can measure chloride up to 5 molal (sufficient for nearly all geothermal applications) in solutions up to 45 ° C (113 ° F).

3.5. Conclusion

Drilling costs, especially for early-stage exploration and confirmation of resources, is the most significant impediment to global geothermal development. Despite decades of effort and expenditure, geothermal drilling costs have not decreased. The use of slimholes in the 1990s demonstrated that drilling and testing of smaller diameter boreholes, which are less costly to drill, can be used to assess the commercial viability of a potential geothermal resource.

Further reduction in geothermal development costs can potentially be achieved by drilling microholes with diameters as small as 5 cm (2 in.). However, our analyses have demonstrated that evaluation of microholes using current production or injection test

methods does not provide the measurement resolution of the critical parameters required for scaling up well performance to production-sized wells. Evaluation of microholes may be accomplished using a DST tool modified from designs currently used in oil and gas applications. Measurement of fluid composition is also important in geothermal resource assessment. We have shown that production flow tests of microholes have physical limitations, so a continuous flow of geothermal fluid will not be available for geochemical sampling and analysis. Instead, we propose repurposing existing and newly emerging fluid analysis techniques to measure fluid compositions in-situ. Combining microhole drilling, DST technology, and downhole geochemical measurement has the potential to yield rapid, lower cost assessment of geothermal resources.

3.6. References for Section 3

Ding, K., and W. Seyfried. 2007. "In Situ Measurement of pH and Dissolved H2 in Mid-Ocean Ridge Hydrothermal Fluids at Elevated Temperatures and Pressures." *Chem. Rev.*, 107(2) (January 2007), pp 601–622.

Gao, X.; Zhang, J.; Yang, Y., and H. Deng 2010. Fabrication and Performance of All-Solid-StateChloride Sensors in Synthetic Concrete Pore Solutions. *Sensors*, 10 (November 2010), pp. 10226–10239.

Garg, S., and J. Combs. 1993. *Use of Slim Holes for Geothermal Exploration and Reservoir Assessment: A Preliminary Report on Japanese Experience.* In Proceedings of the Stanford Workshop on Geothermal Reservoir Engineering held in Stanford, California, June 1993.

Johnson, M.S.; Billett, M.F.; Dinsmore, K.J.; Wallin, M.; Dyson, K.E.; and Jassal, R.S., 2010. Direct and continuous measurement of dissolved carbon dioxide in freshwater aquatic systems – method and applications. *Ecohydrology* 3, (February 2010), pp. 68–78.

Mansure, A.J., and D.A. Blankenship. 2013. Geothermal Well Cost Update 2013. *GRC Transactions*, 37.

Osborn, W., Hernandez, J., and A. George. 2014. *Successful Discovery Drilling in Roseau Valley, Commonwealth of Dominica*. In Proceedings of the Thirty-Ninth

Workshop on Geothermal Reservoir Engineering, held in Stanford, California, February 24–26, 2014. Curran Associates, Inc.

Silverman, R.L.; Lukawski, M.Z.; and J.W. Tester, 2014. "Uncertainty Analysis of Geothermal Well Drilling and Completion Costs." *GRC Transactions*, 38 (January 2014), pp. 419–422. "Uncertainty Analysis of Geothermal Well Drilling and Completion Costs," *GRC Transactions*, 38

Tuttle, J.D.; Reilly, S.; Combs, J.; Welch, V.; and R. Listi. 2010. "Managing Geothermal Exploratory Drilling Risks: Drilling Geothermal Exploration and Delineation Wells with Small- Footprint, Highly-Portable Hydraulic Diamond Core Rigs," *GRC Transactions*, Vol. 34 (January 2010).

French, D.E., 1994. "Utility of drill-stem tests in determination of the geothermal regime of Railroad Valley, Nye County, Nevada," *AAPG Bulletin*, 79(6) (December 1994), pp. 917–918.

WELLSIM. Software from Geothermal Science and Data Systems. Available at http://www.gsds.co.nz/wellsim/.

4. MICROHOLE SYSTEM SPECIFICATIONS

This section documents the functional requirements for the low WOB microhole drilling project. It identifies subsystems, system interfaces, and functional requirements necessary to meet the project objectives. Instrumentation to control WOB and rotation are considered, but directional drilling is not considered at this time. The subsystems and potential components used for those systems are shown in Figure 4-1.

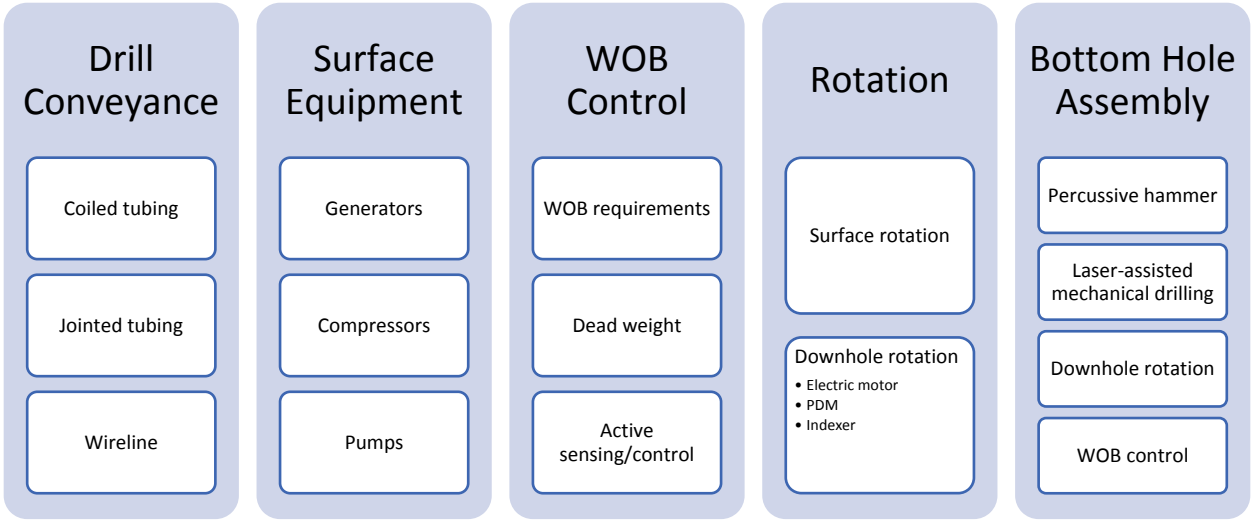

Figure 4-1. Microhole drilling subsystems

Definitions and requirements for various system components are described in the following subsections. Although the overall microhole drilling system is in the development process, the scope of the current proof-of-concept project activities will target WOB control, rotation, and the BHA.

4.1. Drill Pipe Conveyance System

The drill pipe conveyance system advances the bit during drilling and retracts it on pullback, which is all performed from the ground surface. Typical methods of performing these operations include jointed pipe, coiled tubing, and wireline. For this microhole drilling demonstration, the drill pipe conveyance system shall (i) provide up to 2,000 lbf (~8,900 N) drilling force, (ii) generate and handle 4,000 lbf (~17,800 N) of pullback

force, (iii) provide up to 30 ft (~9.1 m) of continuous drilling, and (iv) traverse up to 3 in./s (7.6 cm/s) during drilling and pullback.

The connections between parts of the drill string include mechanical, electrical, and optical interfaces. Mechanical interfaces between drill string components shall utilize standard API (American Petroleum Institute) tool joint connections. Some configurations for the microhole drilling system may require optical interfaces between surface components and BHA components, and those configurations shall be provided by the subsystem provider.

4.2. Surface Equipment

Surface equipment is additional equipment needed to drill the borehole, including air compressors, generators, or any other equipment located on the ground surface and not in the borehole. The surface equipment shall use standard pipe and hose fittings and connections to interface with the microhole drilling system.

4.3. Weight-on-Bit Control

The microhole drilling system will likely employ CTD-based technologies, which is convenient because of the continuous conduit to the surface. However, controlling the weight on the drill bit is challenging. Both the laser-mechanical drilling and the percussive hammer drilling will require a minimal amount of WOB. The rotational requirements are also dependent on WOB control.

A robust WOB application and control scheme is critical to the success of the project. Thus, the WOB subsystem shall be capable of regulating the WOB during drilling between 500–2,000 lbf (~2,220–8,900 N) based on a drilling rate up to 100 ft/hr (~30.5 m/hr). The WOB control subsystem shall be capable of transmitting the full pullback force.

4.4. Bit Rotation

Previous efforts at microhole drilling utilized turbines and small diameter PDMs. Electric motors are also an option because of the low torque requirements. Two main types of low WOB drilling were considered for this microhole drilling demonstration—laser-assisted mechanical drilling and down-the-hole hammers

(DTHH)—and each have different rotation requirements. The laser-assisted mechanical drilling rotation subsystem requires rotation rates up to 1500 rpm and up to 200 lbf-ft (~270 Nm) of torque, while the DTHH (percussive hammer) drilling rotation subsystem requires rotation rates up to 60 rpm and up to 700 lbf-ft (~950 Nm) of torque.

4.5. Bottom Hole Assembly

The bottom hole assembly includes the components that generate rock cuttings. Our project requires a conventional low WOB tool, such as the percussive hammer or the laser-assisted mechanical drilling assembly. Components in the BHA may include but are not limited to the bit, WOB control, and downhole rotation. This demonstration shall be capable of drilling holes between 2.5–4.0 in. (~6.4–10.2 cm) diameter.

The expected temperatures for geothermal exploration or monitoring can reach 300 ° C (572 ° F), and the pressures and chemical environments are also on the extreme-end of existing technology. With that in mind, we took steps toward ruggedizing components for geothermal environments. The specifications for this project included BHA components capable of operating in temperatures up to 250 ° C (482 ° F) and differential pressures up to 3,000 psi (~20,690 kPa).

5. LASER-ASSISTED MECHANICAL DRILLING

This content for Section 6 was provided by Foro Energy.

5.1. Summary

A 3⅝ in. (~9.2 cm) diameter laser mechanical laboratory drilling BHA was designed, built, and tested. This program produced an extremely high laser power density on the rock and required a water-cooled bit for the first time. The best rate of penetration (ROP) achieved was 17 ft/hr (~5.2 m/hr) with 1,000 lbs (~454 kg) WOB, 20 kW (~27 hp) of power, and 200 rpm. The resulting torque was 70 lbf-ft (~95 Nm). Future work should focus on system redesign and testing to improve manufacturability, assemble-ability, ROP, and reliability.

5.2. Definition and Requirements for High-Power Laser Surface Laboratory Drilling Tool

Three categories of requirements were laid out—operational, performance, and interface—which were derived from planned interfaces within the overall drilling system.

5.2.1. Operational Requirements

Operational requirements are shown in Table 5-1.

Table 5-1. Operational Requirements

Parameter	Requirement
Excavate material	Sierra White granite
Diameter	>Ø 3 in. (~7.6 cm)
Depth	12 in. (~30.5 cm), minimum
ROP	>40 ft/hr (~12.2 m/hr)

5.2.2. Performance Requirements

Performance requirements are shown in Table 5-2.

Table 5-2. Performance Requirements

Parameter	Requirement
WOB	up to 500 lbs (~227 kg)

Parameter	Requirement
WOB sensing & control	5% resolution (lbf)
Position sensing & control	3% resolution (deg)
Bit rotation	up to 1500 rpm
Laser wavelength	1064–1070 nm
Laser Power	up to 20 kW (~27 hp)
Power Intensity	>1.12 kW/cm^2
Deposited power	"flat top" beam shape

5.2.3. Interface Requirements

Interface requirements are shown in Table 5-3.

Table 5-3. Interface Requirements

Parameter	Requirement
Tool length	up to 4 ft (~1.2 m)
Tool diameter	up to 3 in. (~7.6 cm)
Tool reaction torque	200 lbf-ft, max (~270 Nm)

5.3. Laser Power Required to Fracture Rock

One of the most important considerations for understanding laser/rock interactions is the threshold laser power for a specific beam profile when the rock begins to spall. Before any physical testing was performed on the Sierra White granite, calculations were performed to better understand the magnitude of laser power required to cause spalling. Equation EQ5-1 gives the maximum temperature change that Sierra White can withstand before it fails. Equation EQ5-1 assumes that all properties are isotropic, ν = 0.28, and that fracture stress is adequately described by the Brazilian Tensile Test (BTS).

Equation EQ5-1 is the maximum impulsive temperature change before failure:

$$\Delta T_{max} = \frac{(1-\nu)(\sigma_t + UCS)}{\alpha E} = \frac{(.72)(1280+25940)\,psi}{(7.56e^{-6}/^{\circ}C)(7.832e^{6}\,psi)} = 330^{\circ}C \qquad \text{EQ5-1}$$

If the fracture stress is assumed to follow equation EQ5-2 more closely than the BTS value, then the maximum impulse temperature would rise to 356 ° C (673 ° F), and the equation for fracture stress is given by:

$$\sigma_t = \frac{K_{IC}}{\sqrt{\pi C}} \qquad \text{EQ5-2}$$

Given the above calculated temperature, the amount of laser power required to reach that minimum temperature can be given by equation EQ5-3. These calculations are only approximations and could be missing important criteria, so actual results may vary. Equation EQ5-3 is the laser power required for minimum rock fracturing temperature:

$$q = K\frac{\delta T}{\delta x} \rightarrow \left(2.1\frac{W}{m°C}\right)\left(\frac{330°C}{.001m}\right) = 693\frac{kW}{m^2}\left(.00456m^2\right) = 3.2kW \qquad \text{EQ5-3}$$

Experiments were performed to determine how much laser power was required to induce spalling Figure 5-1

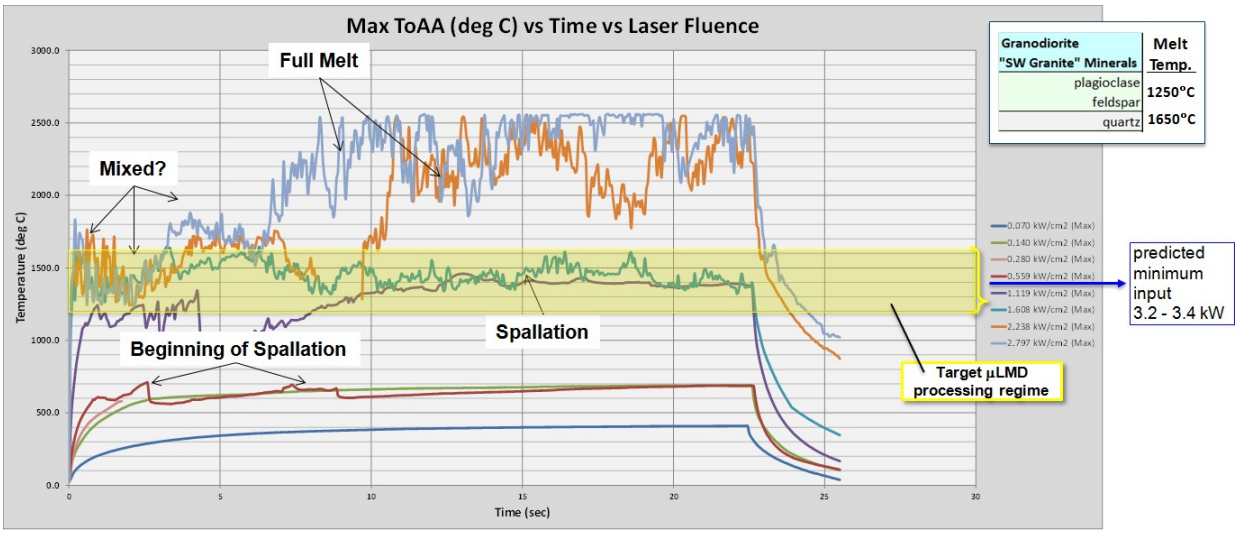

Figure 5-1. Temperature vs. time for various laser fluences

The laser induced damage threshold of Sierra White was compared to Dolomite and Lake Mountain Limestone (Figure 5-2 and Figure 5-3). The testing was performed under atmospheric conditions with a round beam size of 0.85 in. (~2.2 cm) diameter and 60 scfm (1.7 m^3/min) of air through a nozzle pointed at a 45 degree angle to the target.

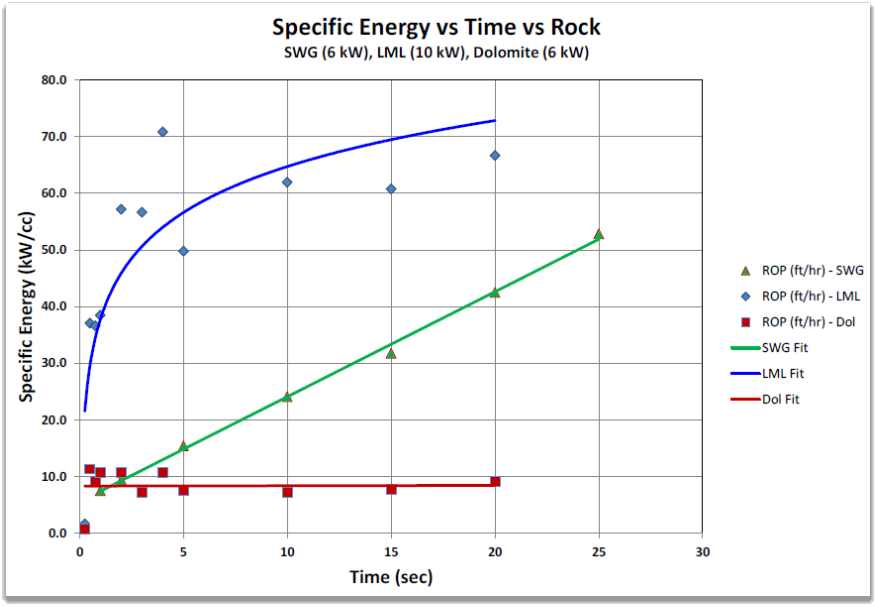

Figure 5-2. Specific energy vs. time vs. rock

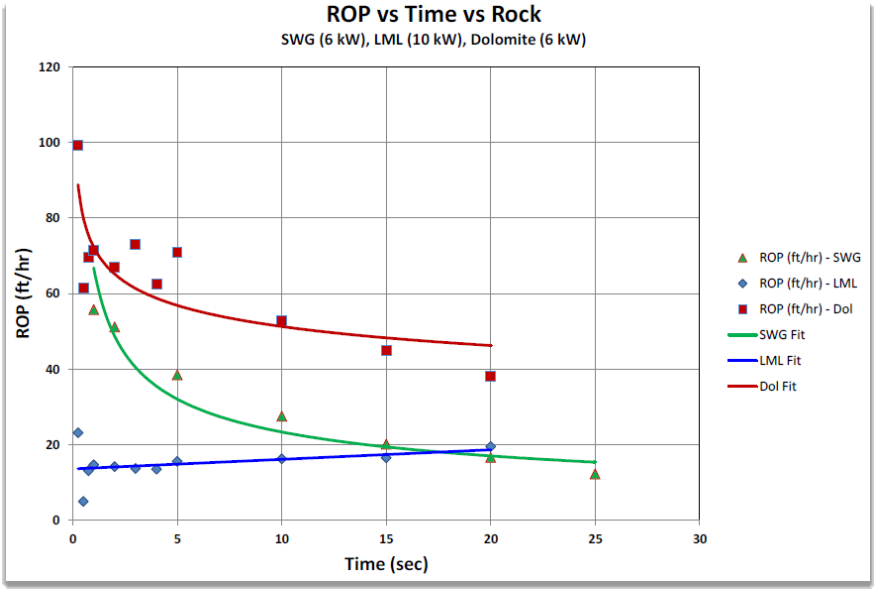

Figure 5-3. ROP vs. time vs. rock

5.4. ROP Scaling Based on Historical Results

A selection of drilling data points, based on Foro Energy's historical work, was chosen to identify potential ROP values for the microhole design. These data points were scaled linearly based on equations EQ5-4 through EQ5-6.

Equation EQ5-4 is for ROP scaling:

$$ROP_{scaled} = ROP_{data} \times \frac{Area_{scaled} / LaserPower_{scaled}}{Area_{data} / LaserPower_{data}} \qquad \text{EQ5-4}$$

Equation EQ5-5 is for torque scaling:

$$Torque_{scaled} = Torque_{data} \times \frac{Radius_{scaled}}{Radius_{data}} \qquad \text{EQ5-5}$$

Equation EQ5-6 is for WOB scaling:

$$WOB_{scaled} = WOB_{data} \times \frac{Area_{scaled}}{Area_{data}} \qquad \text{EQ5-6}$$

Simple scaling of the data shows that ROP in excess of 40 ft/hr (~12.2 m/hr) might be possible, but the linear scaling also makes large assumptions. The first is that all of the data can be scaled linearly. Previous drilling data show nearly linear correlations, as calculated, but this project will be operating in a parameter space that has never been explored. The scaling also assumes that Sierra White will behave similarly during drilling. In addition, the bit is assumed to be capable of surviving the increased power density and subsequent heat loads. The 8.5 in. (~21.6 cm) bit had problems with heat (melting) when using 63.5 kW of power, which equates to an average power density of 6.8 kW/cm^2. The 4 in. (~10.2 cm) bit design operated with a power density of 10.8 kW/cm^2 and also had heat problems. In order to reach the laser powers required, this program

will have to reach a power density of 18.3 kW/cm^2, which is nearly double any previous design.

5.5. Bit Reflected Power Analysis

A two-part analysis was performed to determine how much power might be reflected back to the bit. The legacy 8.5 in. (~21.6 cm) BHA geometry was used for initial comparisons between the two analyses. The analytical analysis predicted 350 W of back-reflected power onto the bit, while the simulation predicted 392 W.

An analysis was also performed for an assumed microhole-scaled configuration using Sierra White properties instead of Dolomite. The amount of energy per surface area impinging on the microhole was found to be similar.

The analytical analysis in Mathcad was performed using Equation 5-7, while the simulation was run in FRED optical engineering software (Figures 5-4 and 5-5).

Equation 5-7 is the governing equations for view factor analysis:

$$F_{1-2} = \frac{1}{(x_2 - x_1)(y_2 - y_1)} \sum_{l=1}^{2} \sum_{k=1}^{2} \sum_{j=1}^{2} \sum_{i=1}^{2} \left[-1^{(i+j+k+l)} G(x_i, y_i, \eta_k, \xi_l) \right] \qquad \text{EQ5-7}$$

$$G = \frac{1}{2\pi} \left\{ (y-\eta)\sqrt{x^2+\xi^2}\,\tan^{-1}(K) - \frac{1}{4}\left[\left(x^2+\xi^2\right)\ln\left(1+K^2\right) - (y-\eta)^2 \ln\left(1+\frac{1}{K^2}\right) \right] \right\}$$

Where $K \equiv \dfrac{(y-\eta)}{\sqrt{x^2+\xi^2}}$

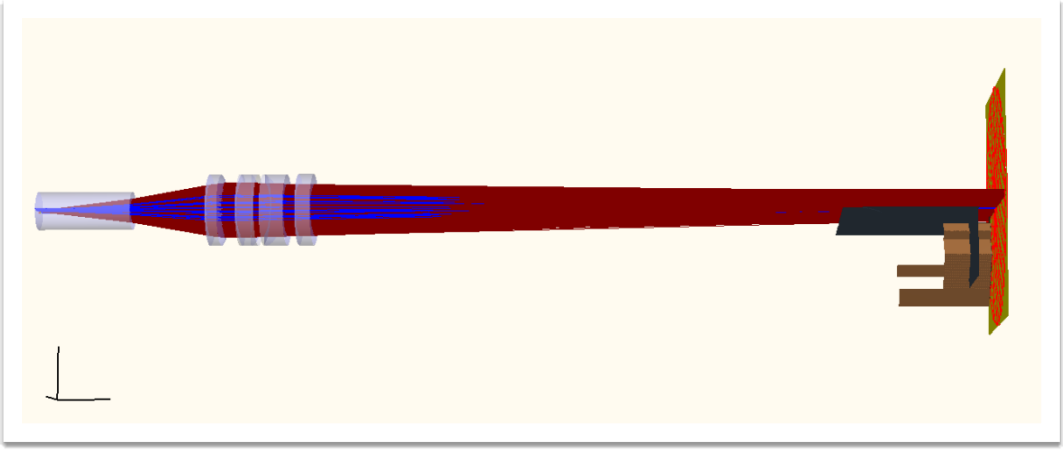

Figure 5-4. FRED simulation side view

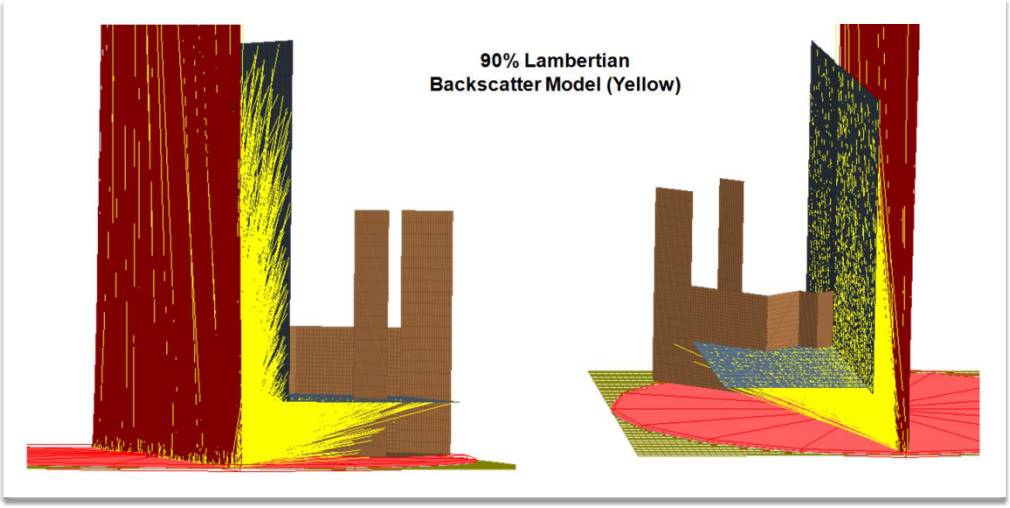

Figure 5-5. Fred simulation Lambertian backscatter

5.6. Component Testing

Preliminary component testing was performed to verify the adequacy of the cooling for the downhole connector and the bearing arrangement. Figure 5-6 and Figure 5-7 show the test setup, and Figure 5-8 and Figure 5-9 show the test results.

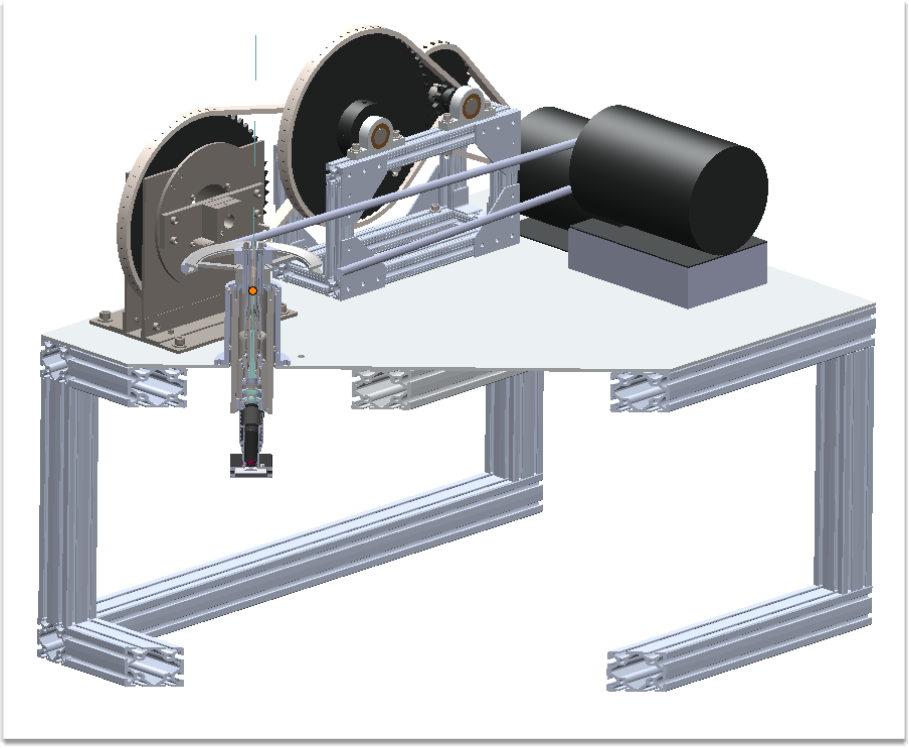

Figure 5-6. Component test setup cross section

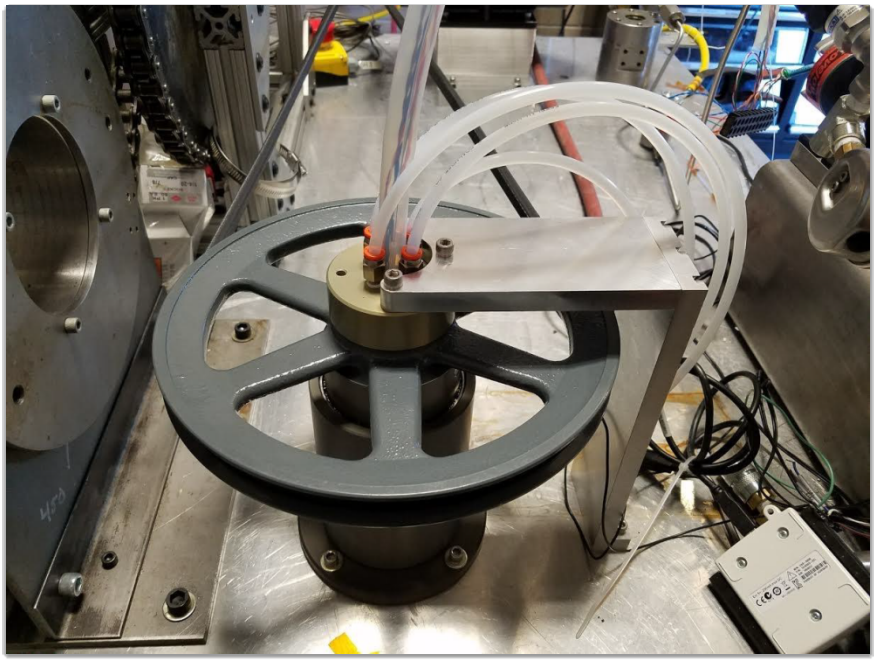

Figure 5-7. Top of component test setup

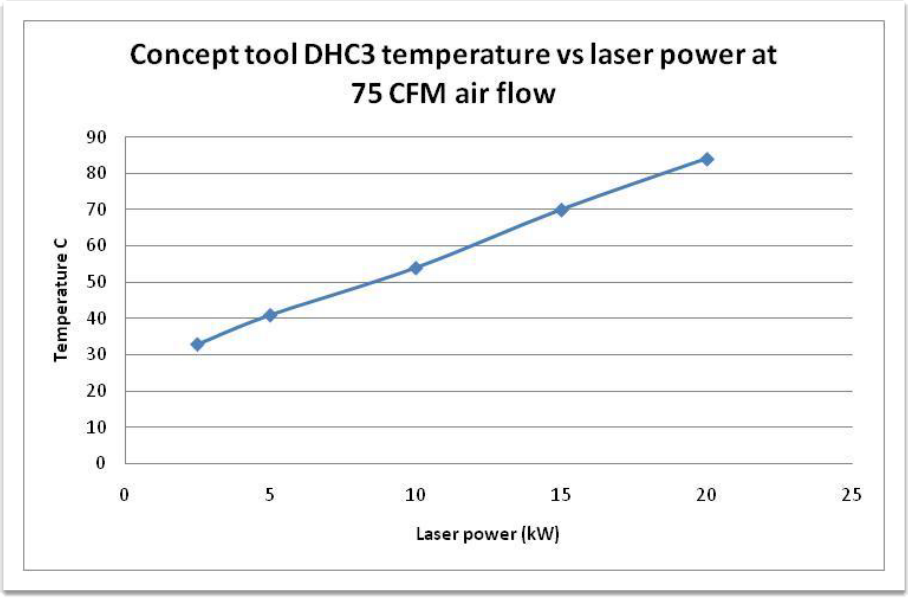

Figure 5-8. Concept tool downhole connector 3 (DHC3) temperature vs. laser power at 75 scfm (~2.1 m^3/min) air flow

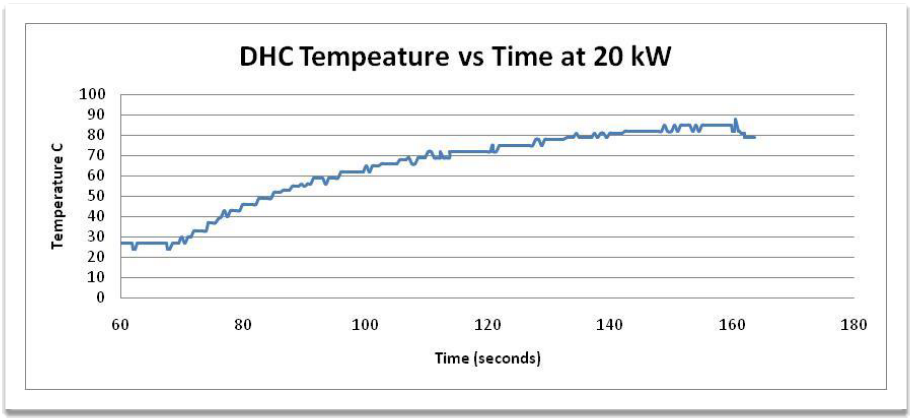

Figure 5-9. Downhole connector (DHC) temperature vs. time at 20 kW (~27 hp)

5.7. Test Rig Integration

The BHA was designed to be operated on Foro Energy's current test drilling rig or a similar test drilling rig as shown in Figure 5-10. An off-axis motor design was chosen to

provide a large parameter space for rapid process development without having to source or design an inline electric drive.

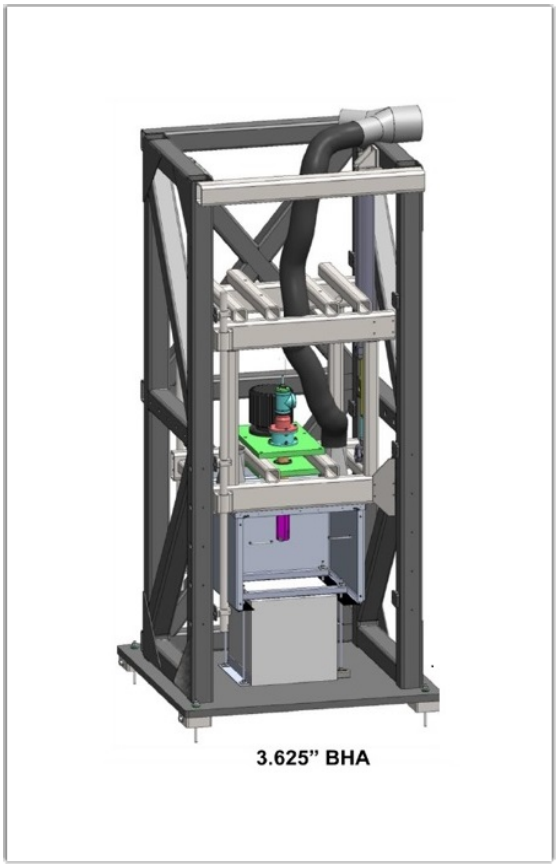

Figure 5-10. Foro Energy test rig with BHA

5.8. Optics Design

The laser power is delivered to the BHA via fiber optic cable. The distal end of the fiber optic cable has an optical connector, also called a downhole connector. Beyond the DHC is a series of optics that shape the beam into the desired bowtie configuration, and the final optic is a protective window. The bowtie style beam profile is generated by a series of three optics and protected by a window. Figure 5-11 through Figure 5-13 summarize the design and performance.

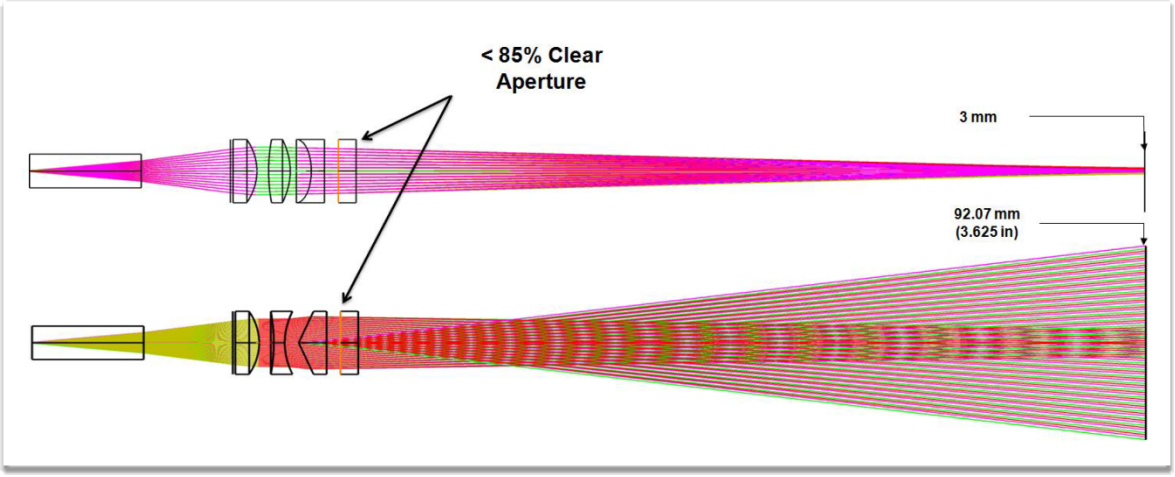

Figure 5-11. Optics and beam profile design

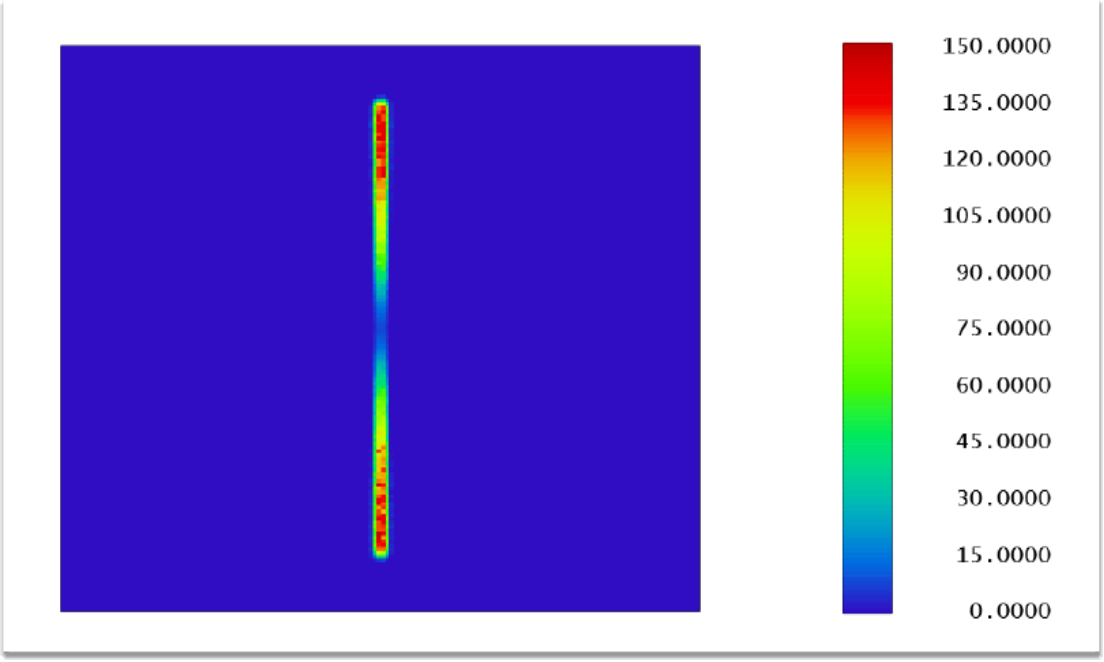

Figure 5-12. Instantaneous power distribution on rock surface

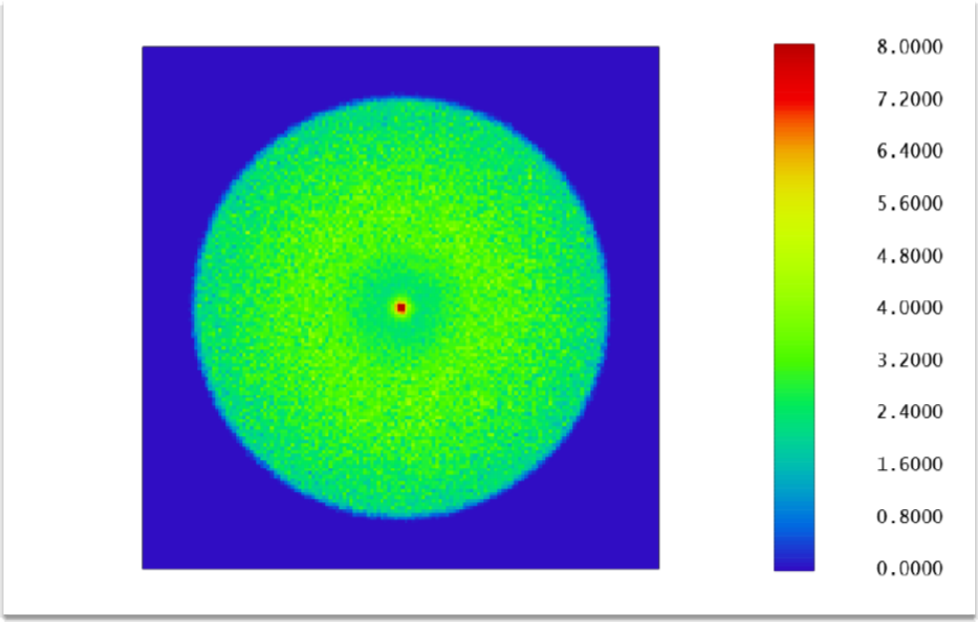

Figure 5-13. Rotationally averaged laser power on rock surface

5.9. Optomechanical Design

The optomechanical design was approached using methods similar to those developed for previous designs. The optics are mounted with spacers and spring-loaded. The spacers are precisely machined to fit the optics with minimal contact stresses to help provide alignment. The nonsymmetrical lenses were designed with flats on the OD to rotationally align them to the housing.

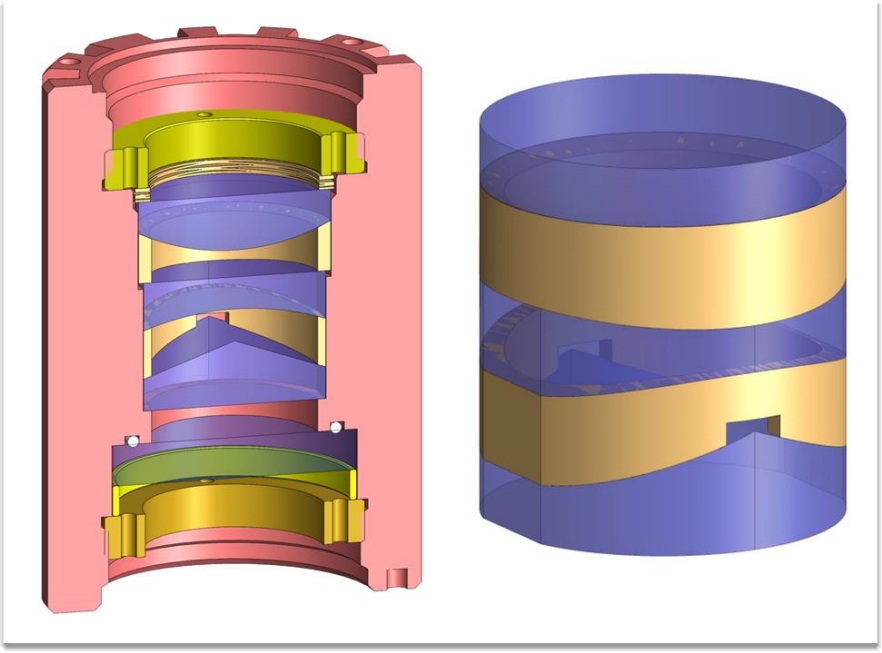

Figure 5-14. Optomechanical design

5.10. Bit Cooling

The design also included active bit cooling due to the anticipated back reflections. Instead of having closed-loop cooling, the design exhausts the water near the top of the bit.

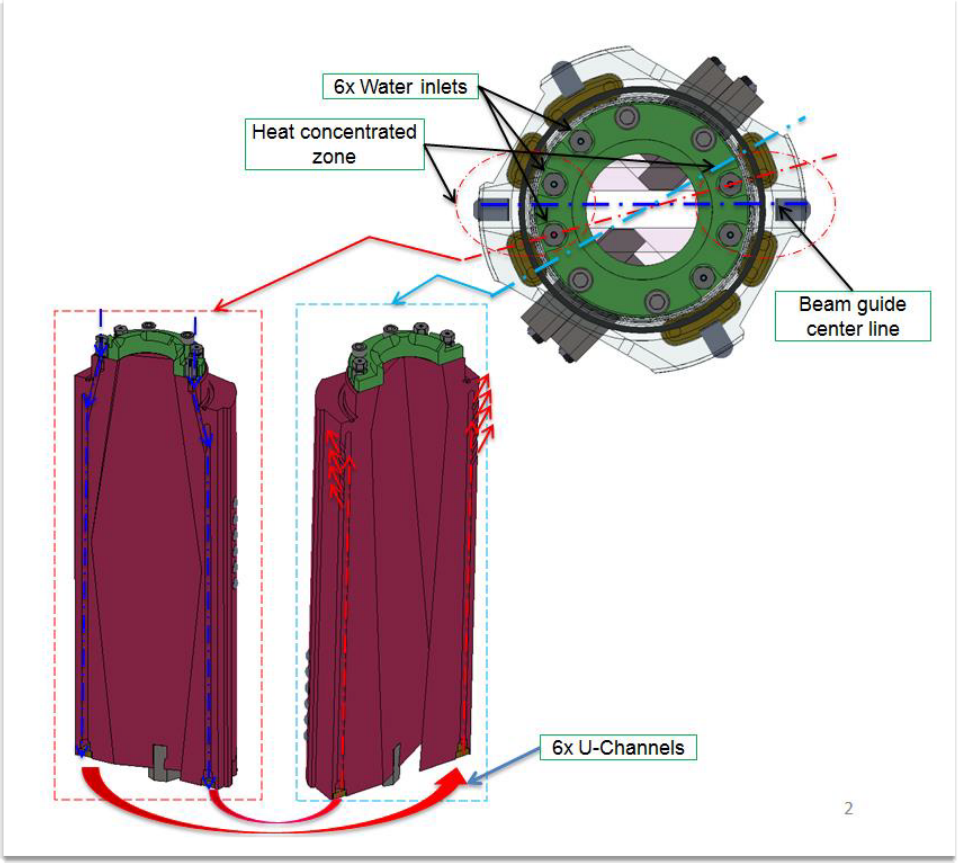

Figure 5-15. Active bit cooling scheme

5.11. Required Airflow

Simple standard calculations were performed to determine a starting point for the flow rate required to clean the hole based on depth and ROP. Based on the assumption of a 3⅝ in. (~9.2 cm) borehole size and 1.5 in. (~3.8 cm) coiled tubing, a flow rate of 300–400 scfm (~8.5–11.3 m^3/min) appeared appropriate.

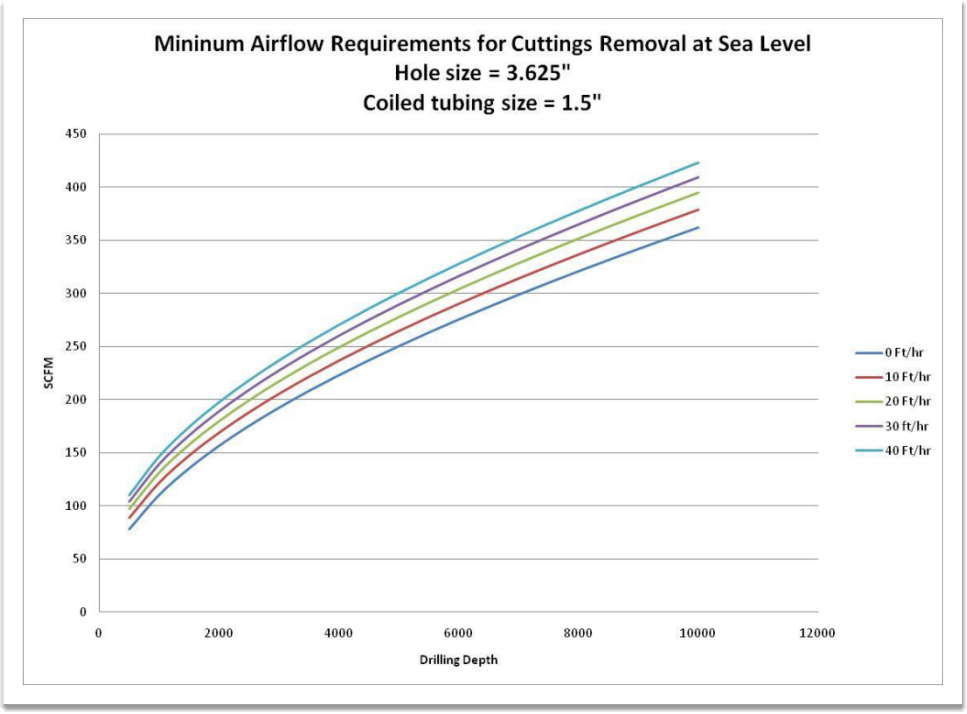

Figure 5-16. Minimum airflow requirements for hole cleaning

The airflow requirements for optics cooling and protection will have to be experimentally determined, but the amount needed for hole cleaning should be sufficient. The airflow capacity of the test rig is 600 scfm (~17 m^3/min).

5.12. Cutting Structure Design

The design of the cutting structure is crucial to the efficiency, ROP, and survivability of the bit. Two fundamentally different cutting structures were conceived. One concept used traditional polycrystalline diamond compact (PDC) bits (Figure 5-19), while the other used knife-shaped inserts with impregnated diamonds (Figure 5-18). The PDC concept was ultimately selected due to the better cutting action. The bit and cutter blades were designed to be easily replaceable in case of damaged cutters, damaged blades, or the desire to test other configurations (Figure 5-19).

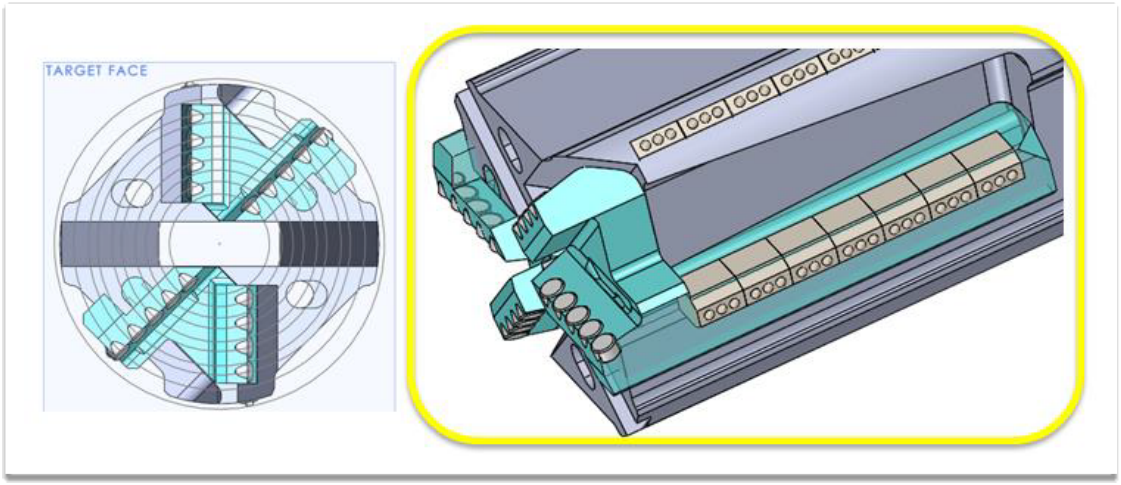

Figure 5-17. Early PDC concept

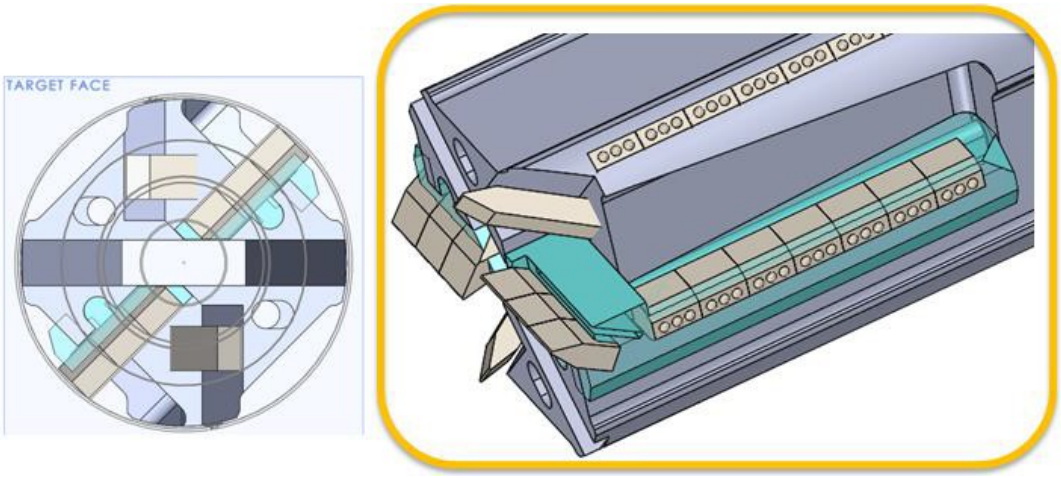

Figure 5-18. Early knife blade concept

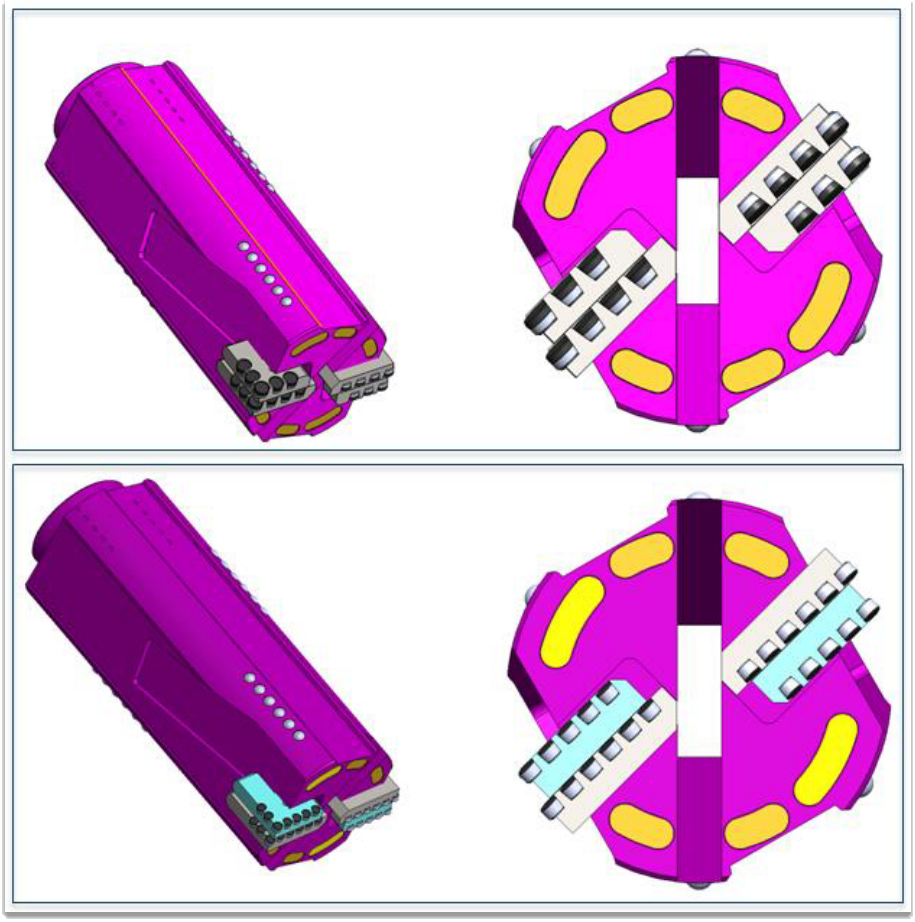

Figure 5-19. Two initial cutting structure designs using different PDC sizes

5.13. Lab Testing of Drilling Tool

Figure 5-19 shows the integration of the BHA into the drill rig, and Figure 5-20 shows the assembled bit.

Figure 5-20. BHA integration into drill rig

Figure 5-21. Assembled bit

Some optimization work was performed with multiple optical configurations. Further optimization work was not performed due to tool reliability. The three optical configurations were a flat window, a window with a 509 mm radius concave cylinder, and a window with a 381 mm concave cylinder. The reason for the different window configurations was to change the balance of laser power across the bottom of the hole. The default flat window configuration was to leave rock in the center of the hole, high-centering the bit and slowing down the ROP. The most extreme window with the 381 mm radius appeared to completely eliminate the mound in the center of the hole but possibly removed too much power from the gage, and the resulting ROP was the slowest of the configurations. The 509 mm radius window left a small mound but still performed the best. Figure 5-22 shows the difference in performance of the different beam profiles for five different test parameters.

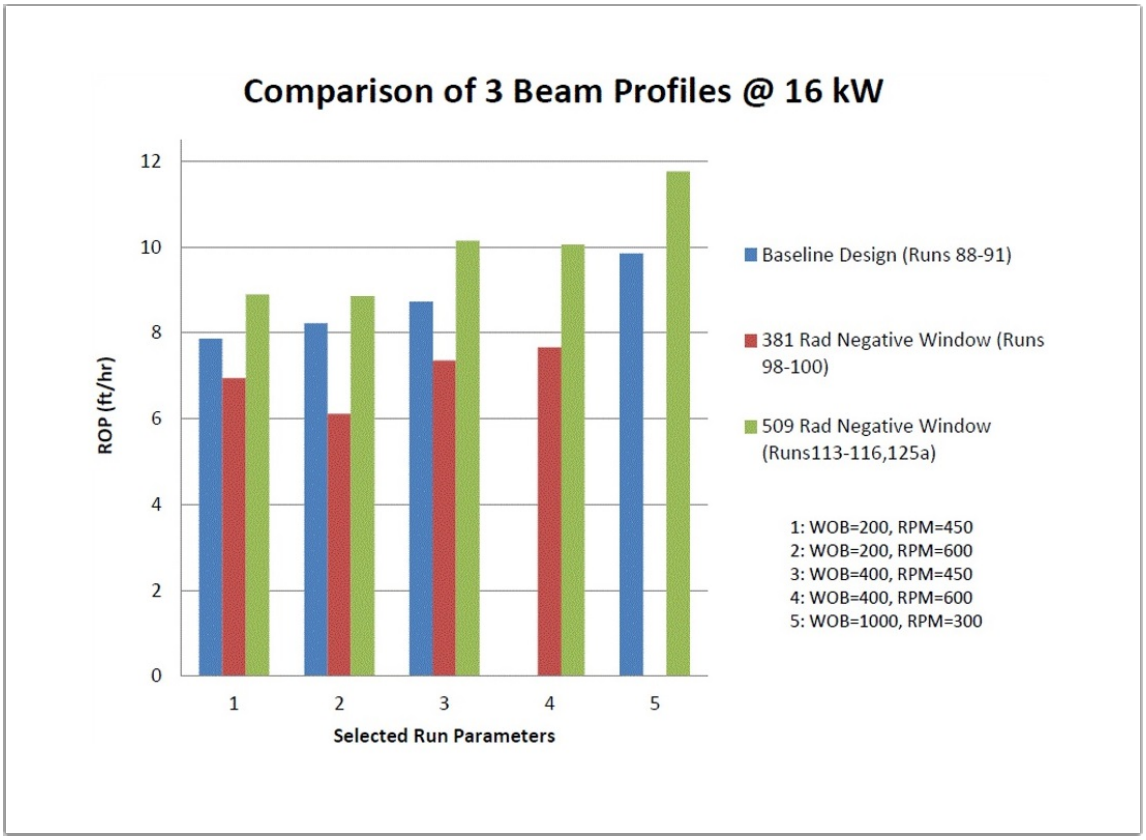

Figure 5-22. Comparison of different optical configurations

Most of the testing was performed with the planer window due to the number of windows in inventory. The maximum ROP achieved in the laboratory was 17 ft/hr (~5 m/hr). This ROP was achieved with 1,000 lbs (~454 kg) WOB, 20 kW (~27 hp) of power, and 200 rpm. The resulting torque was 70 lbf-ft (~95 Nm).

Figures 5-22 through 5-29 are a series of graphs of the test data from the planar window. Some of the trends show what might be predicted based on previous drilling experience, such as higher laser powers resulting in higher ROP (Figure 5-23) or increasing WOB increasing ROP (Figure 5-26 and Figure 5-28). Some of the trends show the opposite of expectations, like increasing mechanical power increasing ROP at 16 kW (Figure 5-24) but not at 20 kW (~27 hp) (Figure 5-25) or higher rpm increasing ROP at 16 kW (Figure 5-27) but not at 20 kW (~27 hp) (Figure 5-29). More data is needed to verify these trends and confirm that variances between runs did not interfere with the results.

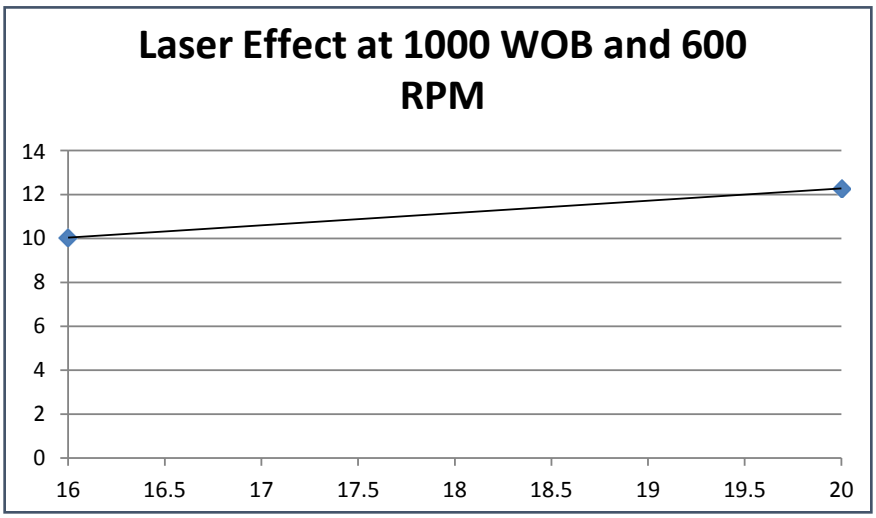

Figure 5-23. Laser effect at 1,000 WOB and 600 rpm

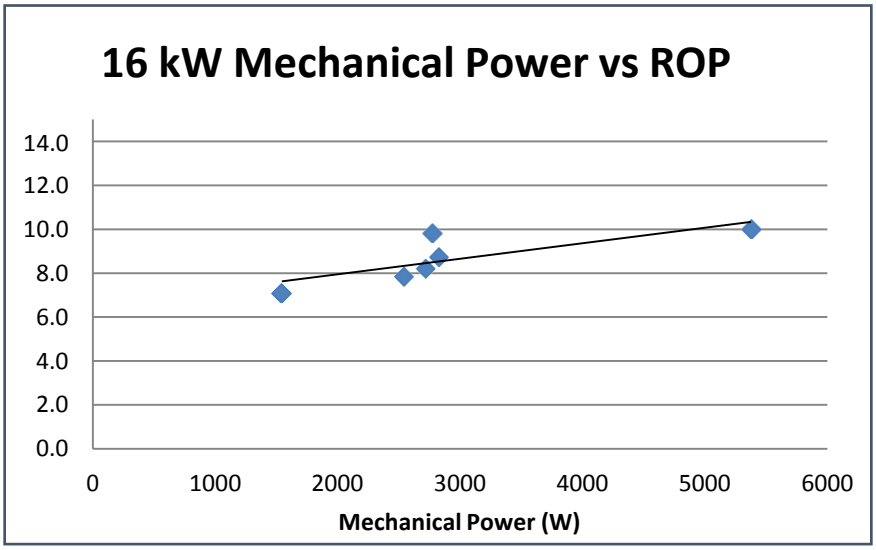

Figure 5-24. 16 kW (~21 hp) Mechanical Power vs. ROP

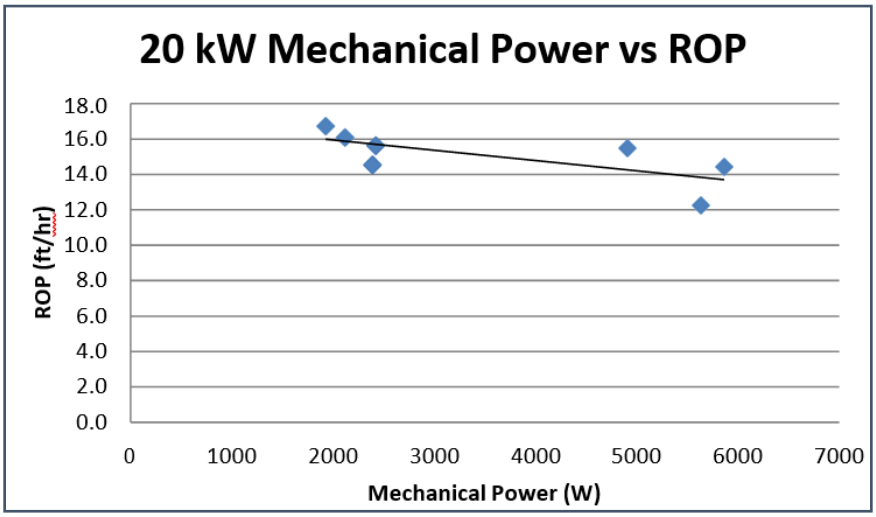

Figure 5-25. 20 kW (~27 hp) Mechanical Power vs. ROP

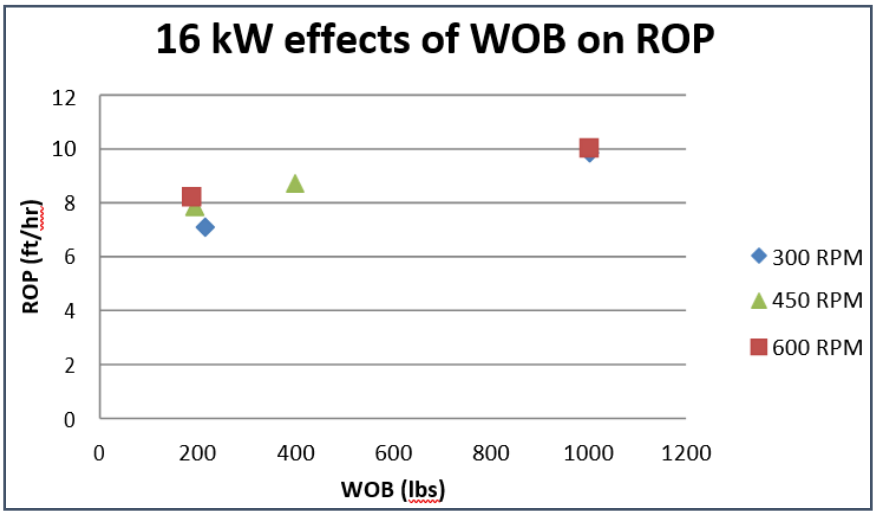

Figure 5-26. 16 kW (~21 hp) effects of WOB on ROP

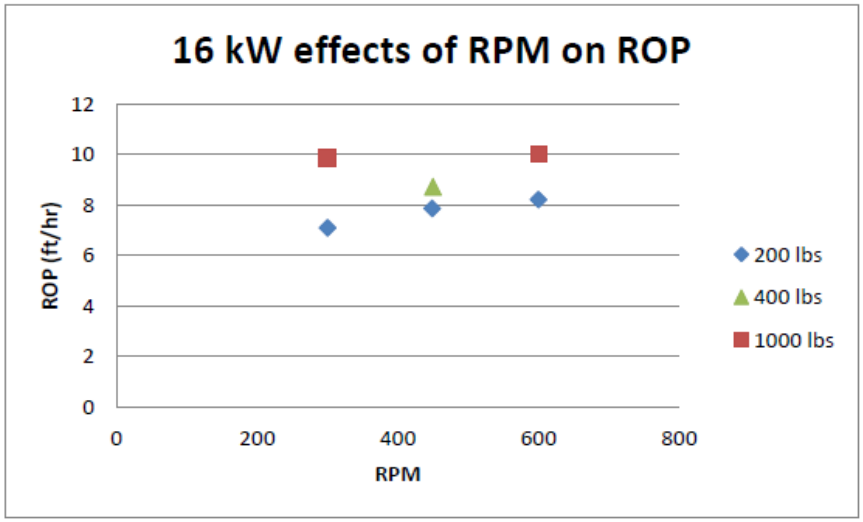

Figure 5-27. 16 kW (~21 hp) effects of RPM on ROP

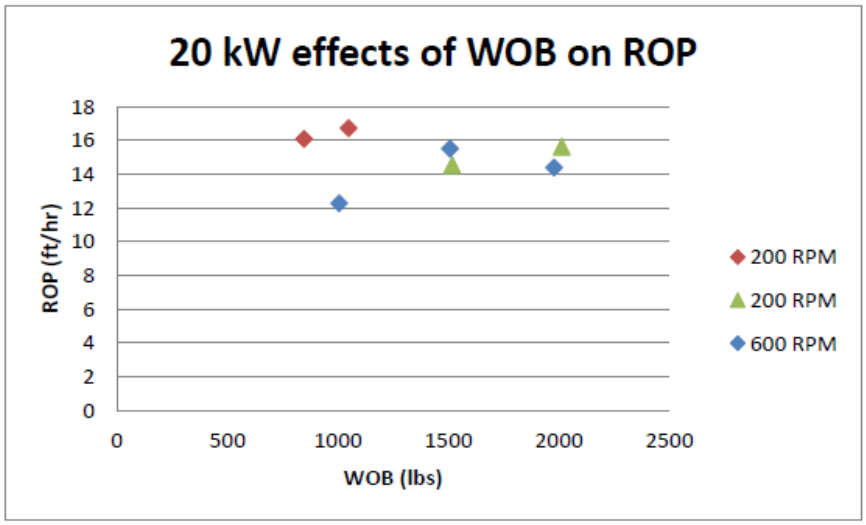

Figure 5-28. 20 kW (~27 hp) effects of WOB on ROP

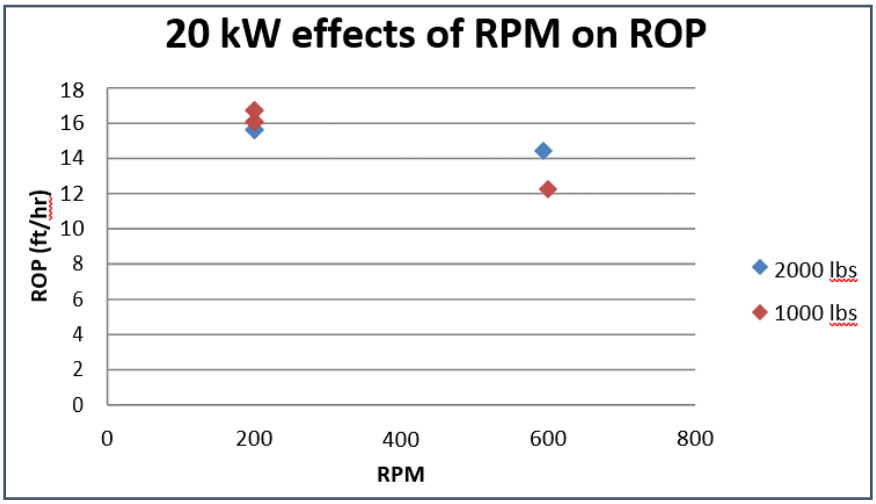

Figure 5-29. 20 kW (~27 hp) effects of rpm on ROP

5.14. Field Integration Requirements

Based on the testing performed and our expert knowledge, we developed a set of requirements for field deployment of a laser-mechanical BHA, described in the following subsections.

5.14.1. Conveyance

Conventional drill pipe or other segmented forms of conveyance cannot be used because a continuous fiber optic cable is needed. Coiled tubing is necessary due to the mechanical requirements of drilling. The coiled tubing should be made of stainless steel and should be kept free of dirt, oil, corrosion, etc. The fiber optic cable should be packaged in a stainless metal tube that can withstand the working pressure. Electrical cabling is also needed to read the connector sensors.

5.14.2. Drive System

5.14.2.1. Physical Dimensions

The maximum OD for a drive system is less than 3.5 in. (~9 cm). An unobstructed borehole needs to exist for the entire length of the drive system with a minimum inner

diameter (ID) of 1.5 in. (~3.8 cm) to allow for airflow, the fiber optic cable, and a water line.

5.14.2.2. Cleanliness

All the components of the drive system that come into contact with the clean airflow must be clean. All connections and joints must be appropriately sealed, and no contamination from the drive system is allowed in the air stream.

5.14.2.3. Performance

The drive system needs to be able to turn in the range of 200–600 rpm and hold the rpm to ±10% rpm at 200 lbf-ft (~270 Nm). The drive system must not stall or drop below 50 rpm at a maximum torque of 200 lbf-ft (~270 Nm).

5.14.3. Air or Nitrogen Flow

An expected range of 400–600 scfm (~11–17 m^3/min) of compressed air or nitrogen is needed for cooling and cuttings removal. The gas flow should be clean, dry, breathable air. Nitrogen is the preferred gas.

5.14.4. Bit Cooling

Due to high back reflections from the laser, the bit needs to be cooled with water.

5.14.4.1. Flow Rate

Proper bit cooling requires a flow rate of 0.5–1.0 gpm (~1.9–3.8 lpm), which must be supplied by an additional waterline from the ground surface to the bit.

5.14.4.2. Cleanliness

The cooling water must be filtered to a maximum particle size of 50 microns and have a maximum total dissolved solids content of 200 ppm.

5.15. Lessons Learned

5.15.1. Mechanical Manufacturing and Design

5.15.1.1. Alignment features

The current design does not include alignment features for all components, producing partial interference between rotating and nonrotating components. This should be considered for all required parts, including the test fixture.

5.15.1.2. Bit design

The current bit design could be improved in several ways. There is not full cutter coverage at the bottom of the hole; a gap exists between the gage cutters and the adjacent outermost cutter. The beam profile requires a gap through the center of the cutting structure, but more work should be done to bring the innermost cutters closer to the absolute center. The bit should also turn clockwise and be made easier to assemble. The effect of different size PDC cutters should also be explored.

5.15.1.3. Fluid slip ring

Several challenges were encountered with the fluid slip ring. The bearings and seals were not designed with disassembly in mind, so repairing these parts is difficult. Although seal sloughing will occur with any rotary seal, the sloughing was migrating into the bearings. This could be partially mitigated by adjusting the seal preload, seal fillers and appropriate hardness, and the finish of the mating surface or by adding labyrinth seals.

5.15.1.4. Water cooling

Overheating caused many problems in the bit. Redesign should include addressing increased water flow through a similarly designed bit and adding cooling options (flowing or spraying) to the cutter blades. The current design uses many small water lines and integrating these lines into the other parts should be considered to lower the pressure drop and greatly improve assemblability.

5.15.1.5. Thread locking

Several different threaded joints backed out during testing, occasionally causing failure. Failure would likely have occurred in all cases if testing had continued long enough. Several threaded joints could be eliminated due to design changes, such as eliminating

the external waterlines. Better locking strategies would be needed for threads that cannot be removed, such as the window retainer and fiber connector retainer. Several of the threaded connections also had fretting damage, which made assembly and disassembly difficult and created particles.

5.15.2. Optical Design

A custom fiber optic cable assembly had to be constructed so it would work with the YLS-60000 laser and the BHA, as currently designed. This created a series of challenges associated with replacement lead times and inventory. A redesign should focus on a more conventional connector and fiber build. With the exception of vibrations, the laboratory environment is a rather benign environment for the fiber optic connector. A much simpler and less expensive fiber optic connector should be used for testing.

The original optical system was designed for a numerical aperture of 0.18, while the actual system measured 0.16, and the optomechanical design did not include a simple method to adjust for this. A redesign should be optimized toward a balanced power distribution on the rock with possible additional power in the center. Any new design should also incorporate the ability to add additional lenses for further optimization. The design and tolerancing of the optics needs to be revisited because it is extremely difficult to assemble the prism and bicylinder lens due to the tight fit, which resulted in several cracked lenses.

5.15.3. Component Testing

The fluid slip ring of the redesign should be thoroughly tested before integration into the final design and assembly.

5.15.4. Reliability

Reliability was a significant problem with this system. Most of these problems are likely associated with the complex design and assembly, insufficient analysis, and lack of adherence to internal best practices for design and component testing. Most of the downtime was related to failures due to contamination affecting the connector, collimator, and window. The contamination of the window was due to a design error on the airflow coming out of the bit. This was mostly addressed with a redesign of a part

that controls the airflow near the window, but the whole area should be further analyzed and redesigned. Two of the connector and collimator failures can be linked to failing fluid slip rings and the rest to contamination. The collimator contamination stemmed mostly from a difficult assembly of the connector into its receptacle in a very dirty environment. Nearly all of the remaining downtime was due to vibration-related failures of the fiber optic connector. The stiffness of the test setup should be revisited.

5.15.5. Measurement and Control System

The greatest concern in the measurement and control system was WOB management and control. Most of the problems were due to placement of the WOB sensors. Originally, the WOB sensors were placed between the hydraulic rams and the carriage, which was not a good location due to friction from the carriage as it moved up and down. The ideal location would be between the BHA and the carriage, which would be the simplest and most direct method of measurement, but this was not used because it required a change to the BHA housings. Instead, load cells were placed below the rock. This created a series of challenges because the rock had to be preloaded against the loadcells and would then be measuring rock preload in addition to WOB. Any change in the preloading of the rock would affect the WOB measurement and control. These problems were mostly mitigated by using large load cells and preloading the rock to well above the potential WOB. Due to these problems, any further work should include load measurement in between the BHA and carriage.

More effort should also be devoted to the control logic and interlocks to make drilling preparation easier, and less common interlock possibilities should be considered. Several failures occurred due to various conditions that were not anticipated by the project.

5.15.6. Alternate Beam Profiles

Laser beam profiles, other than the bowtie, have been investigated outside the scope of this program but have never been fully integrated into a laboratory tool. The basis of the alternate approach would be to greatly increase the laser power density on the rock by cutting kerfs, stripes, swirl patterns, or a series of perforations (Figure 5-30).

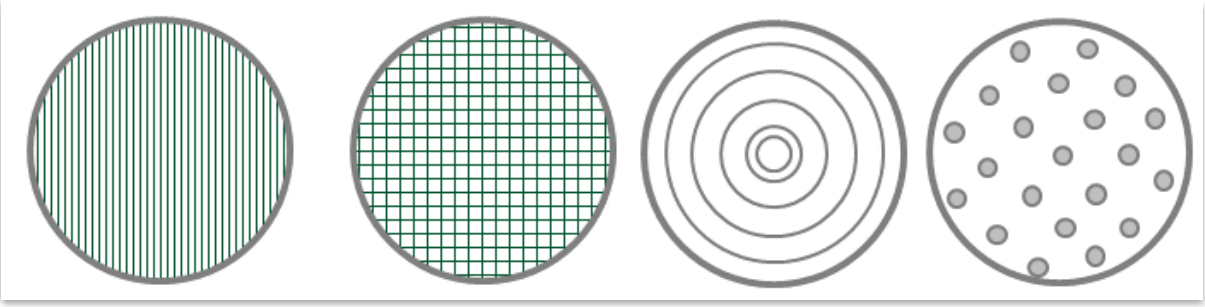

Figure 5-30. Example of potential laser processing patterns

Using the laser to cut a geometric pattern in the rock would not only create a layer of laser-damaged rock but would also create stress risers due to the geometry of the pattern. Once a pattern is created by the laser, a mechanism would be needed to scrape, crush, impact, etc., the damaged surface and remove the affected layer of rock (Figure 5-31). These alternate methods were not explored for this project because they were deemed unnecessary, the ideas were not mature enough, and the implementation would be too complex and difficult.

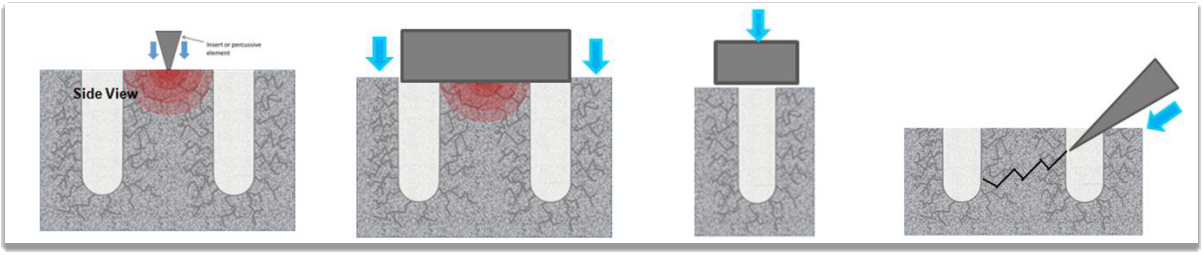

Figure 5-31. Potential rock destruction methods

5.16. Next Steps

Challenges related to the reliability of the drilling system have not allowed a full exploration of the originally planned parameter space. The suboptimum beam profile also created challenges and slowed the drilling process. Due to these problems and because the desired ROP was not achieved, the BHA should be redesigned based on the lessons learned, and the originally proposed parameter space should be re-explored to advance the state of the technology.

6. PERCUSSIVE HAMMER DRILLING

Pneumatic DTHH are used extensively in the mining, construction, and water well drilling industries. They are arguably the best performing drilling technology for hard rock drilling. Percussive hammers are compatible with existing drilling hardware and do not require any specialized equipment for operation. Typical pneumatic hammers operate with a supply pressure up to 350 psi (~2,400 kPa), which is delivered by portable compressors like the one shown in Figure 6-1.

Figure 6-1. Portable air compressor

Established research has shown that percussive devices have among the lowest mechanical specific energies (energy required to remove a given volume of rock) of any drilling method and an industry reputation for reliably drilling hard rock.[6] Research at Sandia in the 1980s demonstrated ROP greater than 20 m/hr in granite. The Sandia tests also showed greater penetration rates compared to conventional drilling under comparable conditions.[7] Pneumatic drilling is particularly advantageous in highly

[6] Kahraman, S., N. Bilgin, and C. Feridunoglu, Dominant rock properties affecting the penetration rate of percussive drills. *International Journal of Rock Mechanics and Mining Sciences*, 2003. 40(5): p. 711–723.
[7] Finger, J.T., Investigation of Percussion Drills for Geothermal Applications. *Journal of Petroleum Technology*, 1984. 36(12): p. 2128–2136.

fractured and cavernous rocks where lost circulation is a concern. It is also well suited to hard, dry formations with relatively small amounts of formation liquids.

As a complement to the laser-assisted mechanical drilling, we also pursued a more conventional approach to rock reduction to minimize overall project risk. One of the low WOB drilling technologies suitable for geothermal drilling is percussive DTHH. Percussive hammers are a promising advanced exploratory drilling technology for geothermal applications since they rely upon rock reduction mechanisms that are well-suited for use in the hard, brittle rock characteristic of geothermal formations. DTHH are also compatible with low-density fluids that are often used for geothermal drilling. Experience in mining, as well as oil and gas drilling, has demonstrated their utility for penetrating hard rock. Percussive hammers have the potential to reduce overall well construction costs by significantly improving the penetration rates in the hot, hard, abrasive environments typical of geothermal drilling.

There are two main varieties of percussive drilling with the primary difference being the source of the percussive action. In a top hammer, sometimes called a drifter drill, the percussive action occurs at the top of the drill string. These hammers are hydraulically operated, with circulated air used to remove cuttings. Top hammers are depth-limited due to energy losses of 4–6% between drill pipe joints.

In a DTHH, the hammer action takes place at the end of the drill string. A fluid driven piston oscillates within an outer shell. The piston strikes the bit delivering the energy required to produce rock reduction (Figure 6-2). Unlike the top hammer, the DTHH can use the same fluid for rock reduction and hole cleaning. One of the primary advantages of the DTHH is that the ROP is proportional to the supplied pressure (i.e., higher pressure results in higher ROP). The limiting factor in penetration rate then becomes the durability of the hammers and bits.

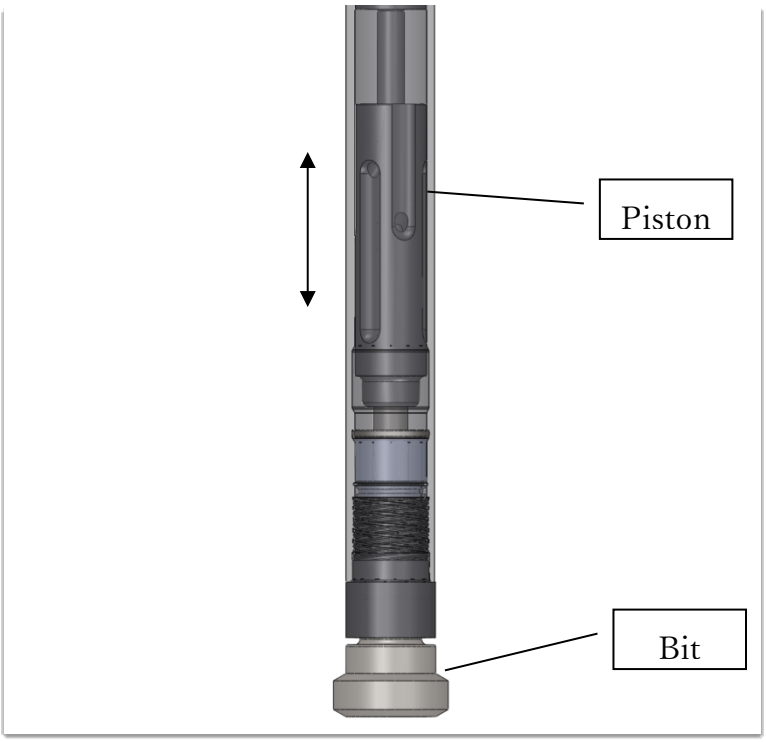

Figure 6-2. DTHH illustration

We explored several small-diameter DTHH hammers for use in this project. The first was an Atlas Copco COP 20 DTHH (Figure 6-3). The COP hammers are designed for use in construction, quarrying, and exploration drilling. It operates on air pressures between 100 and 175 psi (~690 and 1,200 kPa). The hammer uses a BR2 bit shank that does not require a foot valve. The foot valve is a tubular feature that sits on the struck end of the bit. It is part of the compressed air flow path that controls the motion of the piston. It is typically made from a tough plastic, such as nylon or Delrin.

Figure 6-3. Atlas Copco COP 20 percussive hammer

Preliminary drilling tests were conducted using the COP 20 DTHH with a 3 in. (~7.6 cm) bit. Figure 6-4 assesses the performance of the small-diameter valveless foot design.

The tests were conducted at the Sandia High Operating Temperature (HOT) drilling facility using an external 175 psi (~1,200 kPa) compressor. Sierra White granite, which has a published unconfined compressive strength (UCS) of 22 ksi (~150 kPa), was used for the tests.

Figure 6-4. Percussive hammer bit engaged with rock

We encountered reliability issues with the hammer related to inconsistencies in piston cycling. There were several occasions when the hammer would not operate consistently on startup. Consequently, we decided to use more mainstream hammer designs for the remainder of the percussive hammer tests.

6.1. Weight-on-Bit Optimization Routine

In addition to basic hammer functionality, we also developed a WOB management algorithm to optimize WOB while drilling. In conventional rotary drilling, increasing WOB results in a proportional increase in ROP. However, with percussive drilling, this is not necessarily the case. Our experience with percussive hammers has shown that continually increasing WOB does not lead to increasing ROP. This has been shown in

the literature, as well—Song et al.[8] demonstrated that increasing WOB does not lead to higher ROP in percussive drilling (unlike in rotary drilling). There is a sweet spot in the ROP/WOB relationship that does not exist at maximum WOB.

We implemented an optimization algorithm—called a golden section search (GSS)—to systematically identify the preferred WOB for a given set of conditions. The GSS algorithm assumes that the global extrema lies within a search interval (a,b) and that the objective function is unimodal between (a,b).[10] The search space is sequentially searched with decreasing intervals based on the golden ratio. This approach is well suited for ROP optimization because the limits (a,b) may be determined analytically using Hustrulid's[9] model of the physics of percussive drilling, which defines the bounds of drilling phases based on parameters of the drilling medium and the drilling process. The GSS algorithm may then be performed within this smaller interval.

The GSS was implemented in LabVIEW as part of the Sandia HOT facility control software. Sampling intervals in the range of 10 to 20 seconds were used to ensure that parameters stabilized and provided a large signal-to-noise ratio for an average ROP estimate. The average ROP was calculated by dividing the change in depth from the beginning to the end of the calculation interval by the time interval. This substantially smoothed the rate calculation. In addition, a shorter interval (or measurement interval) was used after a fixed delay. The fixed delay was introduced to allow the WOB to converge to the setpoint and eliminate the effects of elasticity in the drill rig or test fixture components. Elasticity in the drill rig or test fixture can show up as drill depth changes when WOB is modulated. Once the search was completed, the best setting was chosen from all the settings that were sampled.

---

[8] Song, X., Aamo, O.M., Kane, PA. et al. Influence of Weight-on-Bit on Percussive Drilling Performance. *Rock Mech Rock Eng* (2020). https://doi.org/10.1007/s00603-020-02232-x

[9] W.A. Hustrulid, C. Fairhurst, A theoretical and experimental study of the percussive drilling of rock part I—theory of percussive drilling, *International Journal of Rock Mechanics and Mining Sciences & Geomechanics Abstracts*,
Volume 8, Issue 4, 1971, Pages 311–333.

[10] J. Kiefer (1953) "Sequential minimax search for a maximum," *Proc. Amer. Math. Soc.* 4:502-506.

The results of the WOB optimization algorithm implementation are shown in Figure 6-5, which shows that the maximum ROP is achieved at an intermediate level of WOB. This optimized value would likely be missed using the standard WOB step test (incremental increases in WOB) used in rotary drilling.

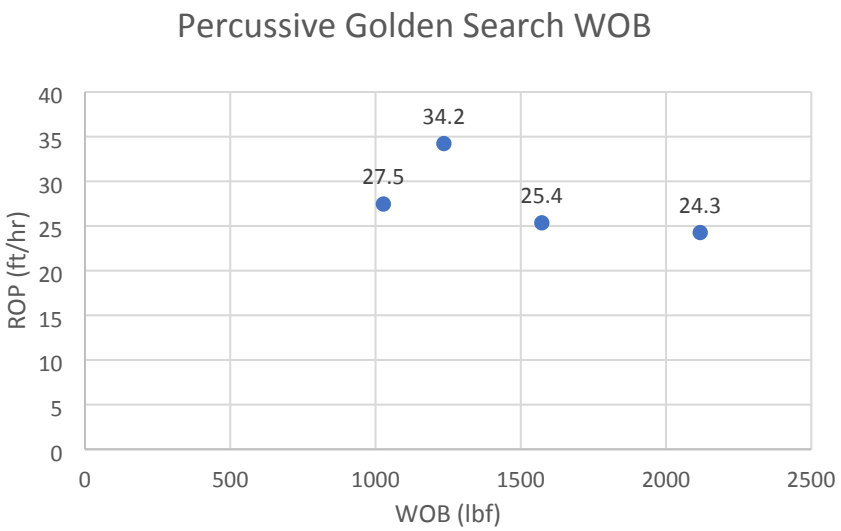

Figure 6-5. WOB control optimization algorithm results

A drill-off test (man vs. machine) was conducted to compare the results of the optimization algorithm versus a static WOB setpoint. For the comparison, the same hammer was used to drill 39 in. (~1 m) using external compressed air set at 175 psi (~1,200 kPa). The static WOB setpoint was 4,000 lbf (~18,000 N). The machine WOB was allowed to execute the GSS algorithm described previously. The results of the test showed a nearly 20% improvement in ROP (27 ft/hr vs. 33 ft/hr [~8 m/hr vs. ~10 m/hr]) using the GSS-optimized WOB selection versus the static value.

6.2. Tool Selection

After the initial problems with the COP 20 hammer, we consulted the factory for a better choice of DTHH for our application. It was recommended that we use the QLX line of hammers based on the expected operating conditions. The QLX 35 (Figure 6-6) was chosen for its performance characteristics and size.

Figure 6-6. Atlas Copco QLX 35 percussive hammer

Conventional operation of percussive hammers requires adding petroleum-based lubricants to the compressed air stream to lubricate the moving parts of the hammer. However, those lubricants break down under expected geothermal temperatures. To address the tribology challenges—friction, wear, and lubrication—we leveraged lessons learned from the previous high-temperature percussive hammer development effort. From that effort, internal components were coated with a solid lubricant to replace the injected rock oil lubricant. The key component that requires lubrication is the piston shown in Figure 6-7. Three key contact surfaces (see Figure 6-8) have been lubricated to prevent galling—wear caused by adhesion between sliding surfaces—and premature damage.

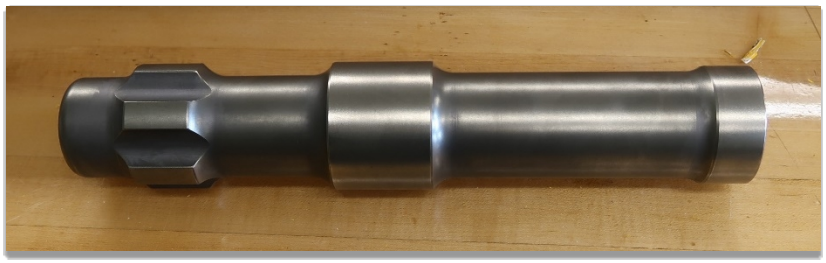

Figure 6-7. QLX 35 uncoated piston

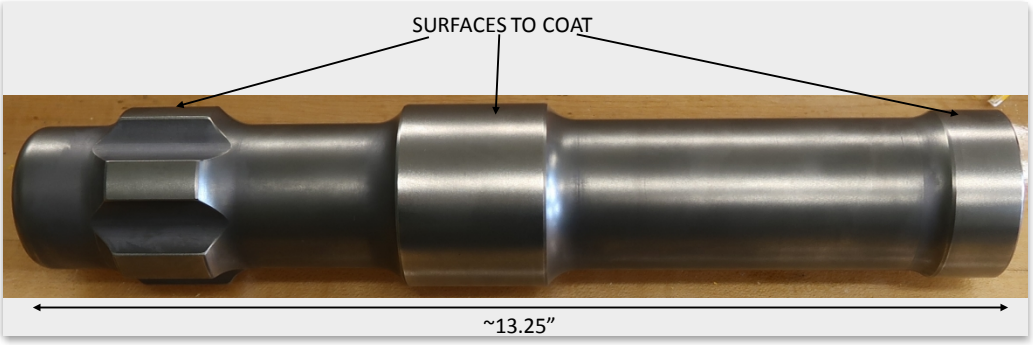

Figure 6-8. QLX 35 piston coated with diamond-like carbon (DLC) for solid lubrication

Sandia worked with a commercial vendor to apply the DLC solid lubricant coating to the piston. The coating is a multi-layer lubricant that protects against adhesive wear. It also reduces the surface tribo-oxidation and increases the load-carrying capacity of the contacting surface.

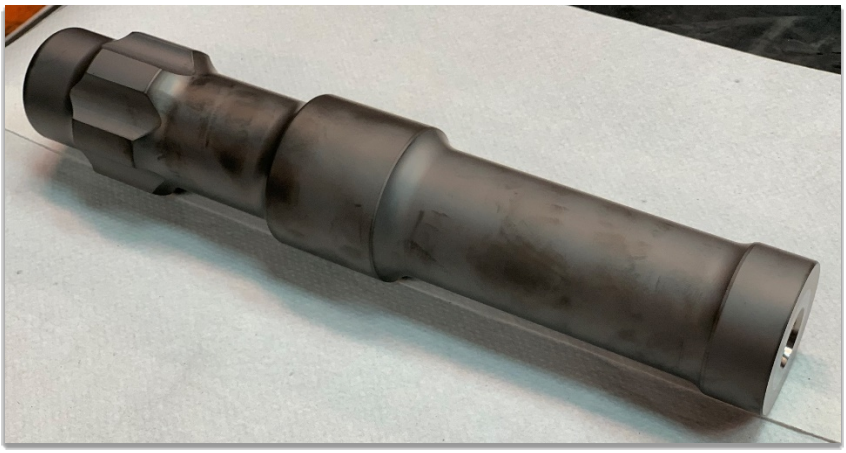

Figure 6-9. QLX 35 piston coated with DLC for solid lubrication

6.3. Summary

In summary, the percussive hammer development described in this section largely focused on identifying gaps between existing commercial off-the-shelf (COTS) hardware and the requirements of the low WOB microhole drilling system developed for this project. The tools were used to refine a WOB control algorithm for the overall system controller. The percussive hammers used in this project were either COTS or lightly

modified COTS components. This was done to provide a path towards commercial adoption since the tools have been proven and are already at a high TRL.

7. DOWNHOLE ROTATION

7.1. Introduction

There are a wide range of potential methods for providing bit rotation downhole, but conventional oil and gas drilling has utilized four primary methods:

1. Rotating the drill string from the ground surface using either a rotary table or top drive.
2. PDM.
3. Turbodrills (turbine motor).
4. Electro-drills (electric powered motor).

The first two methods are by far the most widely used for providing drilling torque. When surface rotation is not practical, PDM is the most prevalent method followed by the turbodrill. Electro-drilling has not attracted worldwide acceptance but has been used by Russian and Ukrainian drillers since the mid-1960s to drill over twelve million meters of rock in Turkmenistan, Azerbaijan, Ukraine, and Russia.

PDMs and turbodrills are available in the U.S. from most suppliers of oil and gas tools and come in standard sizes ranging from approximately 1⅜ in. (~3.5 cm) OD to 11¼ in. (~28.6 cm) OD. Electric drills designed specifically for well drilling are produced by a single company in the Ukraine—Joint Stock Company (JSC) Plant Potencial—in which the smallest size available is 5 in. (12.7 cm) OD.

7.2. Operational Requirements

Developing a set of operational requirements requires a target well. If the maximum well depth does not exceed 5,000 ft (~1,520 m) and the well is drilled from the surface, it is reasonable to assume that the average compressive strength of rock encountered is medium-hard. For our purposes, the maximum uniaxial compressive strength expected is assumed to be 15,000 psi (103,400 kPa). If traditional drill bits are used, a combination of mill-tooth and PDC bits is expected to provide an acceptable level of drilling performance. Of the two bits, the PDC exacts more stringent requirements on both torque and weight and is thus considered below. Assuming a maximum bit diameter of 2.5 in. (~6.4 cm) allows a range of penetration rates and rotary speeds to be considered.

From PDC cutter scratch tests conducted by Richard et al. [1], it is known that the energy required to cut a unit volume of rock is very nearly the same as the rock's uniaxial compressive strength.[10] A relationship can then be developed using an energy approach that relates torque (T), rate of penetration (ROP), rotary speed (N), bit radius (r), and UCS:

$$T = UCS\frac{r^2}{2} \times \frac{ROP}{N} \qquad \text{EQ7-1}$$

This scenario represents an idealized case where the bit is engaged in pure cutting, which is impractical if not impossible. On the other hand, pure cutting for today's typical PDC bits produces mostly reactive torques that must be overcome by the rotational mechanism selected for drilling. For a range of rotational speeds typical of PDM operating speeds, the required torques to drill at select penetration rates with a PDC bit are shown Table 7-1.

Table 7-1. Required Torque for Various ROP

Torque (lbf-ft)[1]		ROP (ft/hr)[2]					
		25	50	75	100	125	150
N (rpm)	100	7.8	15.5	23.3	31.1	38.9	46.6
	150	5.2	10.4	15.5	20.7	25.9	31.1
	200	3.9	7.8	11.7	15.5	19.4	23.3
	250	3.1	6.2	9.3	12.4	15.5	18.7
	300	2.6	5.2	7.8	10.4	13.0	15.5
	350	2.2	4.4	6.7	8.9	11.1	13.3
	400	1.9	3.9	5.8	7.8	9.7	11.7
	450	1.7	3.5	5.2	6.9	8.6	10.4
	500	1.6	3.1	4.7	6.2	7.8	9.3
	550	1.4	2.8	4.2	5.7	7.1	8.5
	600	1.3	2.6	3.9	5.2	6.5	7.8

[1] Multiply lbf-ft by 1.36 to obtain Nm

[2] Multiply ft/hr by 0.305 to obtain m/hr

[10] Confining stresses are here neglected, and perfect cuttings removal is assumed.

Assuming no other torque requirements, a PDC drill bit in a microhole application would require approximately 50 lbf-ft (~70 N/m) from its rotational source. This may generally be the case in an ideal situation provided that sufficient weight can be applied to the bit, but a problem arises in the scaling of drill string strength in a microhole. In a generic drilling situation, it becomes difficult to specify a particular WOB requirement. As a proxy, the minimum WOB is set at 1,000 lbf (~4,450 N).

The following subsections discuss the feasibility of using each of the four rotational methods within the constraints of the general requirements outlined above.

7.3. Surface Rotation (Rotary Table, Top Drive)

Historically, the most popular method for drilling a vertical hole involves rotating the entire drill string from either of two locations at the ground surface: 1) the drill floor or 2) between the drill floor and the traveling block. The first location requires a rotary table to provide torque to a kelly (polygonal-shaped tubing) through the kelly bushing. The second location is preferred. The top drive allows longer drilling intervals before stabbing in another joint (or stand) of pipe and is essentially a hydraulic AC or DC powered motor attached near the traveling block that provides torque to the drill string. Because of this configuration, stands of drill pipe can be dealt with instead of individual joints.

Rotating a long string of drill pipe from one end to provide torque and weight to the bit on the other end for a typical sized borehole has been used to drill countless wells. This implementation is well understood for vertical wells under most conditions. The difficulty of using this scheme for a microhole (even a vertical microhole) is scaling. For instance, buckling of the drill pipe is exacerbated by the reduced pipe diameter and thickness.

If the drill string connections are treated as fixed-free, then buckling in the primary mode is expected at a critical load (P_{cr}) of:

$$P_{cr} = \frac{\pi^2 EI}{4L^2} \qquad \text{EQ7-2}$$

where for a thick tube:

$$I_x = I_y = \frac{\pi}{4}\left(r_o^4 - r_i^4\right) \qquad \text{EQ7-3}$$

All other quantities being equal and using TSC grade drill pipe [2], a standard 2⅞ in. (~7.3 cm) drill pipe will buckle at 1/19th the load of a 6⅝ in. pipe, despite being approximately 43% the diameter and 66% the thickness of larger pipe. For a 5,000 ft (1,520 m) long drill string, the critical load on the 2⅞ in. pipe is approximately 0.3 lbf (~1.3 N) using a standard elastic modulus for steel of 3.0 x 10^7 psi (~2.1 x 10^8 kPa). Indeed, the string is expected to buckle approximately 58 times along the length of a 5,000 ft (1,520 m) borehole. This certainly adds a great deal of undesirable friction during rotation of the drill string and accelerates pipe wear.

A similar exercise may be performed for torsional failure or *twist-off* of the pipe in which shear failure during torsion scales according to the polar moment of inertia or the radius raised to the fourth power:

$$\tau_{max} = \frac{Tr}{J} = \frac{2Tr_o}{\pi\left(r_o^4 - r_i^4\right)} \qquad \text{EQ7-4}$$

Using the same example TSC grade drill pipe with a PDC bit and pure cutting with no pipe buckling, the 2⅞ in. (~7.3 cm) diameter pipe is approximately 1.6 times stronger in torsion when taking into account the rough torque requirement given by equation EQ7-1 and scaled for diameter. In other words, the torsional stiffness of the drill pipe does not decrease linearly with the diameter. This is a highly idealized situation but nonetheless insightful. If TSC drill pipes are indicative of the standard drill pipe, then it is actually the friction induced by buckling of a smaller pipe that tends to exacerbate small pipe torque limitations and not the absolute diameter of the pipe.

Development of friction in the surface rotation setup is further bolstered by annular clearances. Even for slimholes, the annular clearance is generally on the order of ½ in. (~1.3 cm) compared to the typical 1.5–9 in. (~3.8–23 cm) clearance in conventional wells [3]. The anticipated effect of reduced annular clearance is increased contact area between drill pipe and borehole, greater frictional force on the pipe due to increased

lateral force, or both. On the other hand, buckling of the pipe will tend to be reduced in terms of the number of instances. Moreover, rotation of the entire string will reduce the sliding friction of the pipe at the expense of accelerated wear. Nevertheless, high frictional forces are likely to develop that will make surface rotation difficult to implement.

The latter discussion only considers the possibility of a vertical hole. Highly deviated or horizontal holes can be drilled using rotary steerable systems or by combining downhole rotational tools with surface rotation. While this is an option, given the previous discussion regarding clearance and buckling, surface rotation does not appear to offer an advantage in a microhole application.

7.4. Positive Displacement Motors

The use of PDMs in the oil and gas industry has accelerated since the motor's introduction in the late 1950s, and they are now the predominant form of downhole rotation. In comparison to turbines, PDMs can achieve higher torque outputs for a given flow rate with shorter power sections. Depending on the characteristics of the formation being drilled—namely hardness—motors with the same OD but different lobe ratios can be swapped to transition from high torque to high rotational speed. PDMs are also available in a variety of sizes at low relative cost although the smallest OD found in any manufacturer's handbook is $1^{11}/_{32}$ in. (~3.4 cm). PDMs operate according to the Moineau principle to convert hydraulic power to mechanical power (See Figure 7-1).

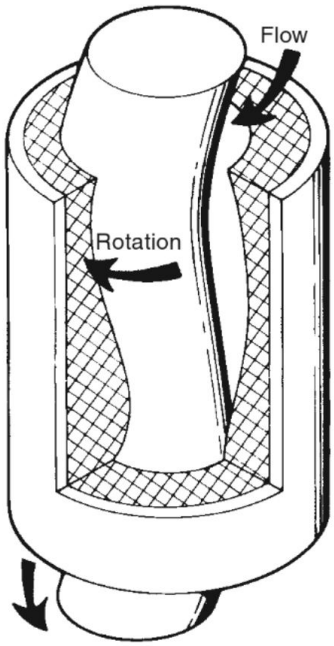

Figure 7-1: Single-lobed PDM [6]

Fluid entering the top of the PDM progresses through a sequence of cavities as the motor rotates. The cavities form between the motor's metal rotor and elastomeric stator, both of which are helically shaped but contain a different number of lobes. The difference between rotor lobe count and stator lobe count is always one. The difference in cross-sectional cavity shape provides an interface for the entering fluid to act against to rotate the stator. Due to the geometry, increasing the number of lobes in both the rotor and stator causes a transition from a high rpm/low torque motor to a low rpm/high torque motor.

Characteristically, torque is linearly related to the differential pressure across the motor. The available operating torque recommended by manufacturers is more than sufficient to effectively drill in most environments. For example, a commercially available 2⅛ in. (~3 cm) OD, 5:6 lobe PDM produces a maximum recommended torque of 340 lbf-ft (~460 Nm) and 620 rpm at a flow rate of 65 gpm (~250 lpm). For comparison, the smallest OD having a 1:2 lobe configuration from the same manufacturer has a rated rotary speed of 990 rpm at 90 gpm (~340 lpm). An example performance chart for a 6¾ in. (~17 cm) OD, 1:2 lobe motor is shown in Figure 7-2 [6].

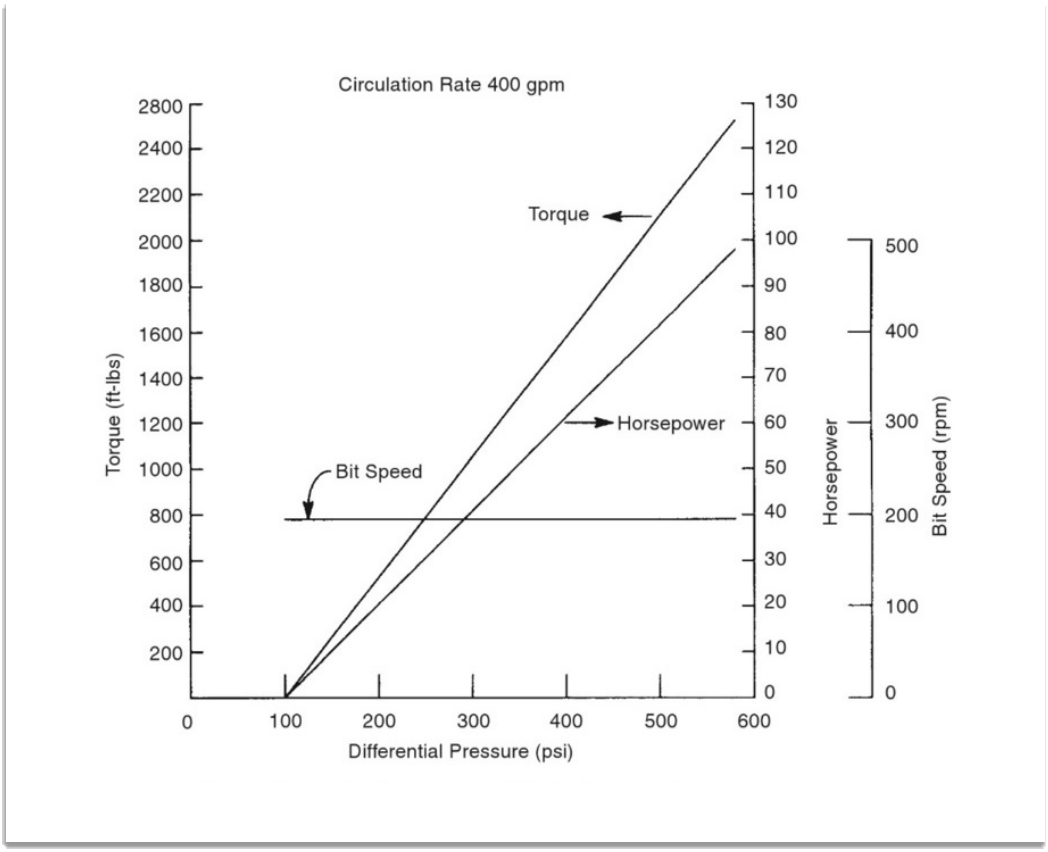

Figure 7-2: Idealized performance for a 6¾ in. (~17 cm) OD, 1:2 lobe PDM

The performance chart shown in Figure 7-2 is instructive but idealized. In actuality, the rotational speed of the rotor responds in a decreasing, curvilinear fashion with differential pressure due to leakage (or blow-by) across the power section. Because of such leakage, horsepower tends to increase at a decreasing rate as differential pressure is increased.

PDMs have a variety of disadvantages, especially in a microhole application. The geometry of the power section, particularly the eccentricity of the rotor's cross-sectional centroid relative to that of the stator, creates eccentric motion in the direction perpendicular to length of the motor. In a borehole with restricted annular clearance, the eccentric motion may translate into impact between motor and formation—a product that is aggravated with low WOB that would tend to anchor the drill string at the bit.

Another major limitation of the PDM is that it requires an elastomer in construction of the stator. Its primary purpose is to create a seal to form cavities with the rotor. Its compliant nature is also the source of problems. One of the primary considerations in the specification of a power section is the fit between the rotor and stator. Greater interference affords better fluid to mechanical power transfer at low speeds by limiting drilling fluid leakage, but a more effective seal exacerbates stator wear and thus limits motor run time and operational speeds. Another consideration is the type of drilling fluid used and the formation fluids encountered. For instance, natural rubber is not particularly compatible with oil-based mud or oxidizing chemicals and tends to become inelastic. If a nitrile elastomer is subjected to most acids, it tends to swell.

Elastomers perform poorly in the presence of high temperatures. Heat induces increased compliance and expansion of any material, causing greater interference of fit in the motor section and promoting greater blow-by. Research into using a metal-metal rotor/stator fit is currently being conducted, but currently no such motors are available.

Further limitations of the PDM in a microhole application were encountered by LANL in their microhole field testing. LANL noted that the flow rates needed to rotate the bit and facilitate cuttings transport caused exaggerated lost circulation and severe washouts in several of the holes drilled [4]. This situation occurred in soft formations encountered at low drilling depths. LANL's drilling results should be similar to other microholes drilled at shallow depths. As mentioned previously, restricted annular clearance limits the maximum cuttings size produced by the bit. LANL estimated that volumetric cuttings concentrations in the annulus must be kept below 5% to avoid particle buildup. Implementation of this requirement naturally introduces a tradeoff: either keep ROP low or increase annular velocity. As a third alternative, foamed drilling fluid may be used with the PDM and may prove effective in addressing the particular problems encountered by LANL.

As a final consideration, PDM efficiency is dependent on the interaction between friction from elastomer sealing and the efficacy of the seal. In other words, interference between the rotor and stator reduces the energy available in the drilling fluid to power the bit. On the other hand, the interference between rotor/stator determines the level of leakage across the motor to a large extent. The expected efficiency (η) of the motor at

maximum recommended differential pressure (p) is easily calculated from the ratio of mechanical power output (P_m) to hydraulic power input (P_h):

$$\eta = \frac{P_m}{P_h} = \frac{(T)(N)}{(p)(Q)} \qquad \text{EQ7-5}$$

where (T) is torque, (N) is rotary speed, and (Q) is flow rate. Based on the one published reference table[11] for a 5/6 lobe, 2.3 stage, $1^{11}/_{16}$ in. (~4.3 cm) PDM, the expected efficiency at maximum operating pressure for their hard rubber section is approximately 73%. The standard elastomer in the same motor at maximum recommended differential pressure yields an efficiency of 66%. Interestingly, the manufacturer reports additional motor efficiency as more stages are added to the motor. For the same hard rubber motor with 2.1 additional stages, the calculated efficiency at maximum recommended differential pressure is just shy of 85%. This result is consistent with calculations, suggesting that additional stages act to provide a better "dynamic seal against leakage" [5]. Yet, the lack of fit and temperature information likely makes the above efficiencies limiting values.

A variety of advantages are afforded by PDM usage including:

1. All types of commonly used bits can be run with a PDM.
2. For a given borehole ID, varying torque/rotary speed configurations are available because performance is related to lobe count.
3. Foamed muds and air mist can be used.
4. Motor performance is easily monitored from the surface via a standpipe.

In light of the results from LANL, drilling systems that rely solely on hydraulic power may undermine drilling campaigns. On the other hand, in the roughly 22 years since LANL's work, motor performance has no doubt improved and with lower flow rate requirements. Included among these improvements—which presumably was not available at the time—is the capability for foamed and misted drilling fluids to be deployed with PDMs. Given the improved performance and wide availability of small

[11] No indication of temperature or fit is provided for the numbers reported.

diameter PDMs, their use in microhole applications as either standalone rotational devices or within rotary steerable systems appears reasonable.

7.5. Turbodrills

First introduced in 1873 as a method of rotating the bit downhole via hydraulic power, the turbodrill, or turbine motor, was one of the first concepts for providing rotational energy to the drill bit downhole. However, it was not until 1934 that drilling mud-operated turbodrills were developed by the Soviet Union. Over the next several decades, turbodrills were not extensively deployed by any group other than the Soviet Union, which invested heavily in development, drilling almost 80% of their wells with the motor.

The mechanics of the turbine are easy to understand on a basic level (See Figure 7-3).

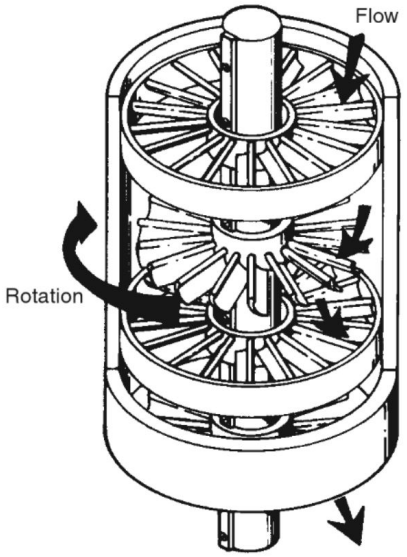

Figure 7-3: Typical turbine motor design [6]

Fluid is pumped at high speed through the upper motor section, causing the angled turbine blades to rotate. Thus, hydraulic power is converted to mechanical power by exploiting the differential pressure that develops across the motor. Based on operational requirements, typical turbodrills have between 25 and 300 rotor/stator stages. For a given geometry and flowrate, increasing the number of stages increases torque output

and peak power at the expense of increased differential pressure and overall motor length.

In general, turbine motors tend to operate at high rotary speed and low torque. While these characteristics can be dealt with by installing a gear train below the motor, the high rotary speeds of the turbine often preclude the use of roller cone bits. PDC bits can achieve high ROP when deployed with turbines but are prone to durability issues, especially if the formation being drilled is especially abrasive or if it is difficult to provide weight on the bit. The latter issue can be addressed partially by using thermally stable diamond bits. Because of potential durability issues, diamond impregnated bits have historically been deployed with turbine motors and only in formations with extremely high compressive strengths, especially abrasive formations, or both hard and abrasive formations.

Typical turbine performance is characterized by a quadratic curve like the one shown in Figure 7-4 for a 6¾ in. (~17 cm) OD, two motor section, 212 stage motor [6].

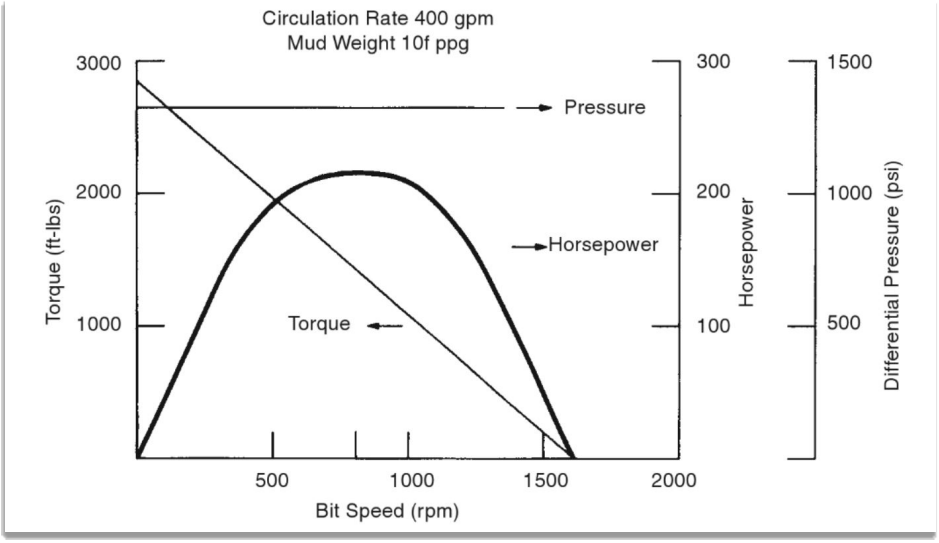

Figure 7-4: Performance curves for an example 6¾ in. (~17 cm) OD, two motor section, 212 stage turbine motor

Peak power is developed at half the runaway speed—the speed the motor will reach if flow is provided to the motor and WOB is zeroed. Additionally, pressure is

approximately constant at a given mud weight and flow rate; if either flow rate or mud weight are changed, the following relationship is generally accepted:

$$A_2 = \left(\frac{q_2}{q_1}\right)^2 A_1 = \left(\frac{\gamma_2}{\gamma_1}\right)^2 A_1 \qquad \text{EQ7-6}$$

In equation EQ7-6, A can represent torque, power, or differential pressure, q is the flow rate, and γ is the mud weight. For rotary speed, only the above relationship involving flow rate holds. It is also important to note that torque increases and speed decreases linearly as weight is applied. Based on the above example motor, it is interesting to note that peak efficiency—as measured by the ratio of mechanical to hydraulic power—is on the order of 70% for flow rates between 200 and 500 gpm (~757 and 1,900 lpm). Additionally, power decreases quadratically with decreasing flow rate at an average decay rate of slightly over 50% when flow is reduced by 20%.

Among the advantages of the turbodrill are:

1. High rotational speeds that are well suited to drilling hard formations.
2. Circulation can occur at zero torque.
3. Construction is entirely metal, making it deployable in thermally challenging environments.

Disadvantages include:

1. Comparatively high flow rates and differential pressures necessitate large surface pump systems.
2. Turbine performance cannot be determined without a measurement while drilling (MWD) system.
3. Relatively clean drilling mud is the only fluid that can be deployed with a turbodrill.
4. Efficiency is relatively poor, especially when running off-peak.
5. Motor sections tend to be relatively long when compared to alternative motors.
6. Lack of historic demand in the U.S. has limited off-the-shelf sizes available, and the motors are relatively expensive.

In a microhole application, several characteristics stand out that would tend to exclude turbodrills from consideration. Depending on the type of deployment type (e.g., rotary, coiled-tubing, etc.), WOB available to the bit may be a limiting factor. If only low WOBs are available, a turbodrill will tend to produce very low torques and very high speeds. Such performance may be acceptable if drilling very hard formations, but in unconsolidated or medium hardness formations at relatively low depths, the resulting speed may simply be too high without an appropriate gear train installation to produce reasonable bit wear rates. Moreover, smaller turbines tend to produce higher speeds and lower torques than their larger counterparts. For example, a commercially available 2⅛ in. (~5.4 cm) OD turbodrill has an optimum rotary speed of approximately 4,000 rpm at a flow rate of 65 gpm (~250 lpm).

Other major considerations involve the need to deploy an MWD system to monitor performance, the restriction on compressible fluids, the limited bits deployable with the turbodrill system, and the relatively clean mud that must be supplied to the motor.

7.6. Electric Drills

Drilling the first well with a downhole, electrically powered motor was accomplished in 1940 by the Soviet Union. Development continued intermittently for about the next three decades, but performance inconsistencies—especially in comparison with hydraulically powered motors—disrupted any major development work since that time. Electro-drills have been used and continue to be used almost exclusively by Russian drillers in specific geographic locations, having drilled an estimated 12 million meters between 1997 and 2005 [7].

Currently, only one company in the world (JSC Plant Potencial located in Ukraine) is known by the authors to produce electro-drills commercially, although recent pushes have been made by DOE to reexamine the potential of electrically driven, ultra-high speed motors. The electro-drill design used by JSC Plant Potencial appears to be largely unchanged since the last development push in the 1970s. The smallest motor they produce is a 3-phase asynchronous squirrel-cage induction motor design capable of producing approximately 2,200 lbf-ft (~2,980 Nm) of torque and a maximum rotary speed of 145 rpm at 126 mm OD. The nominal rotary speed for the same motor without

a planetary gear reducer is 1,297 rpm. At just over 33 ft (10 m) in length, the motor is quite long.

The most recent research into electric motors resulted in several low speed (1,000 rpm) prototype motors with 3 in. (~7.6 cm) OD. Of the various motor designs considered, an inverted configured Permanent Magnet Synchronous Machine (PNSM) design was found to have the highest power density per unit motor length. The proposed PNSM motors were designed as AC/DC radial electric motors with an inner hollow stator to allow circulation of drilling mud through the motor and an outer rotor that connects to the bit.

The potential advantages of the inverted electric motor as a substitute for hydraulically powered downhole motors are numerous. A select few include:

1. Decoupling of bit mechanical power and hydraulic power.
2. Ability to use an expanded set of drilling fluids (i.e., compressible, abrasive, energized, acidic, etc.).
3. Ability to rotate bit forward or in reverse.
4. Quickly scalable power delivery to the bit.
5. Use of high energy drilling systems, such as laser drilling.
6. Ability to incorporate MWD and "logging while drilling" (LWD) systems located near the bit, transmitting data to the surface in real time.

While the potential upside to electric drilling is strikingly evident, implementation has proven to be particularly difficult. One of the major roadblocks in utilizing electro-drills with conventional drill pipe is making a reliable connection between tool joints. In fact, this problem is largely the reason that mud pulse telemetry has persisted, and to the knowledge of the authors, no reliable wired tool joint connections are commercially available. The only related technology applied to segmented drill pipe is an inductive coupler embedded in the tool joint that links wired pipe segments for telemetry purposes, but it cannot be applied to the powering of electro-drills downhole [8].

7.7. Microhole Downhole Motor

The microhole motor concept is an amalgamation of the various drive types described in the previous sections. This is derived from a previous GTO-funded tool development

(the auto indexer) and a commercial pneumatic impact wrench. The tool differs from the auto indexer in that it uses a multi-stage gearbox to drive the output shaft rather than an impulsive loading mechanism.

The motor is designed primarily to operate in conjunction with a percussive DTHH for drilling hard rock formations with the output speed and torque tailored for those applications (~30 rpm). The free-spinning speed is 62 rpm, while the stall torque is 890 lbf-ft (~1,200 Nm). The motor is designed to operate with both compressed air and foam (to help with cuttings removal).

The motor is a modified pneumatic torque wrench, sized to fit in the inline form factor used in a BHA. The motor consists of two primary components: power section and bearing section. The power section consists of a pneumatic vane motor coupled with a 3-stage gear box. An internal flow passage allows the compressed air supply that drives the motor to also drive the percussive hammer.

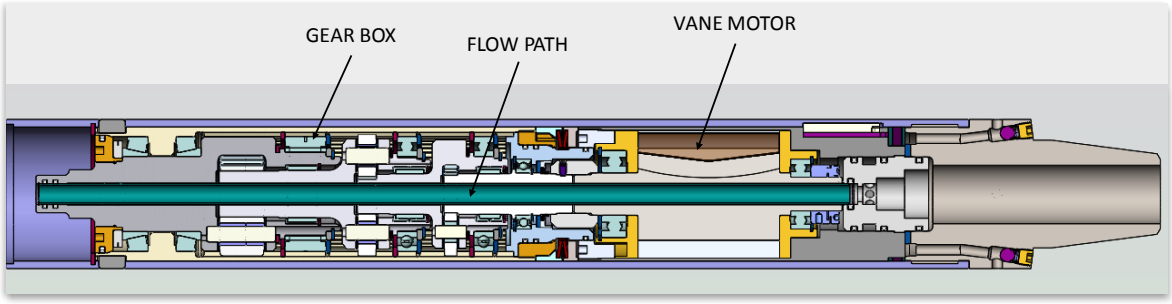

Figure 7-5. Power section cross-sectional view

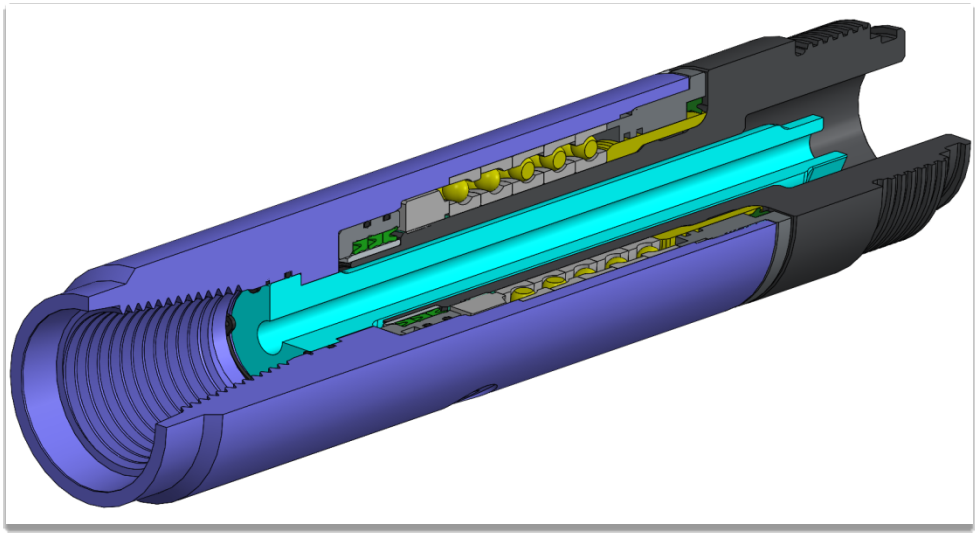

Figure 7-6. Bearing section cross-sectional view

The bearing section consists of stacked angular contact bearings within a steel housing (Figure 7-6), which is a modified commercial part produced by Ditch Witch®. It was designed and built as part of the Technology Commercialization Fund (TCF) collaboration with The Charles Machine Works, Inc.

Initial tests of the motor design were conducted on the Sandia Dynamometer Test Stand. The test stand consists of a Magtrol dynamometer (4PB15-DG-0600), controller, and various interfaces into the input shaft (Figure 7-7). Compressed air up to 100 psi (~690 kPa) is fed into the motor, and an electronic adjustable regulator controls the actual air pressure reaching the motor during the tests.

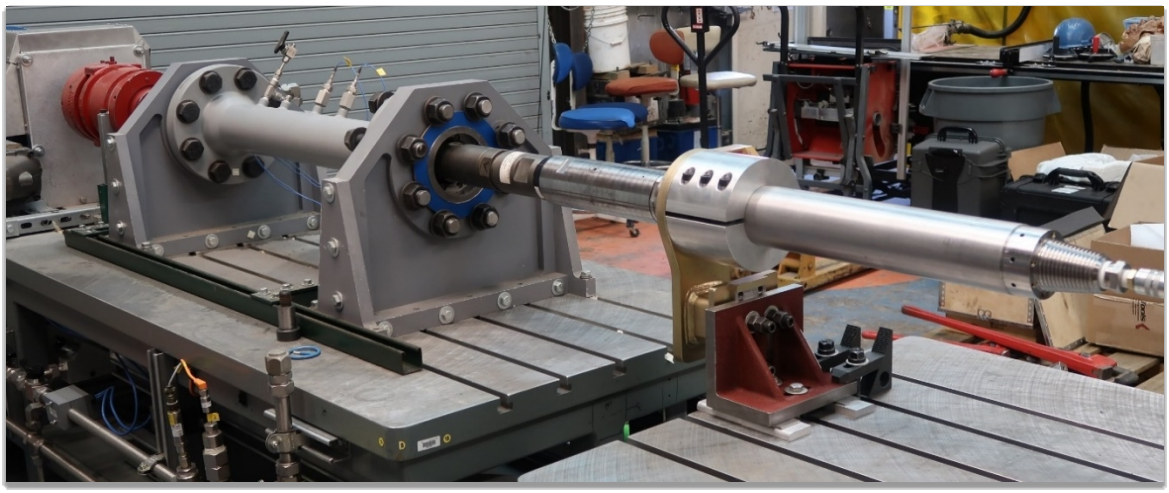

Figure 7-7. Sandia Dynamometer Test Stand

Tests were conducted at two levels of inlet pressure (40 psi [~275 kPa] and 80 psi [~550 kPa]) to assess the performance of the motor under a load. Plots of the test results are shown in Figure 7-8 and Figure 7-9. Tests were conducted until the motor was no longer able to turn the dynamometer (stall torque).

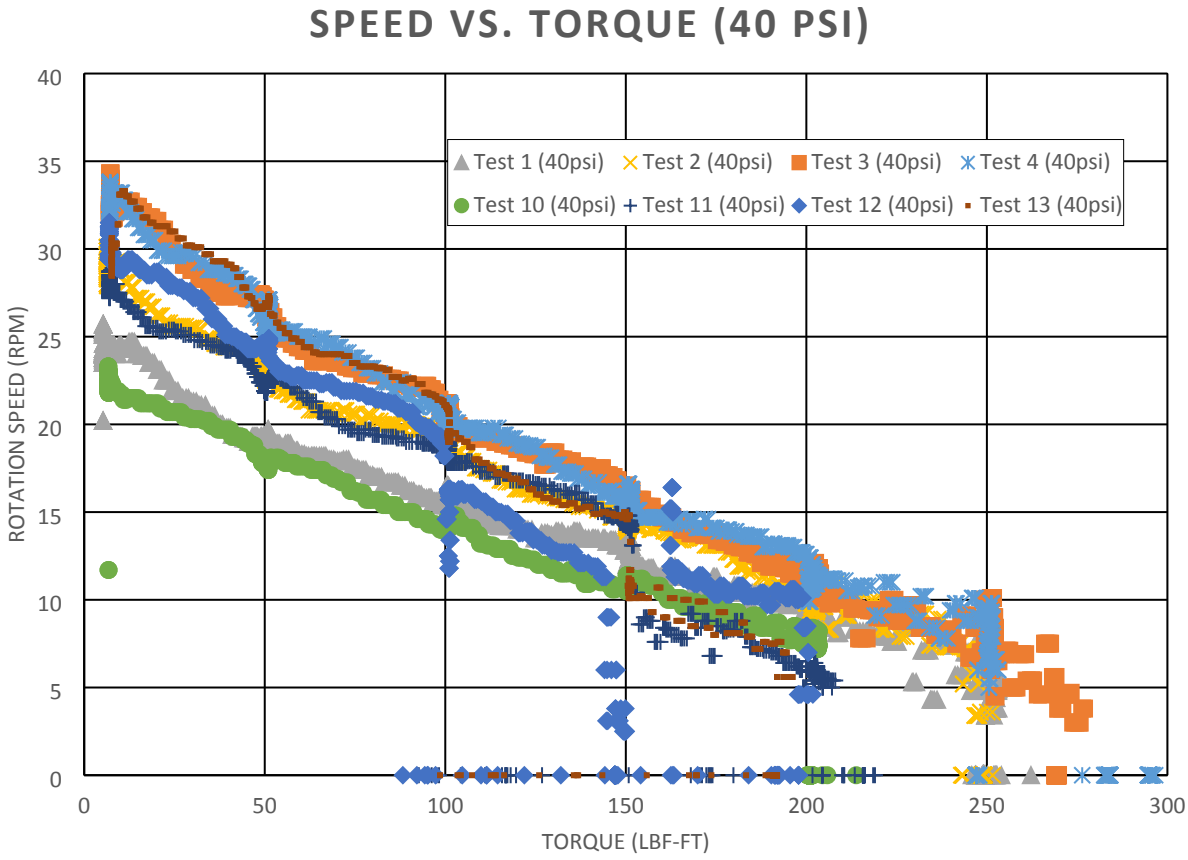

Figure 7-8. Sample dynamometer results for the microhole downhole motor (40 psi [~275 kPa] inlet pressure)

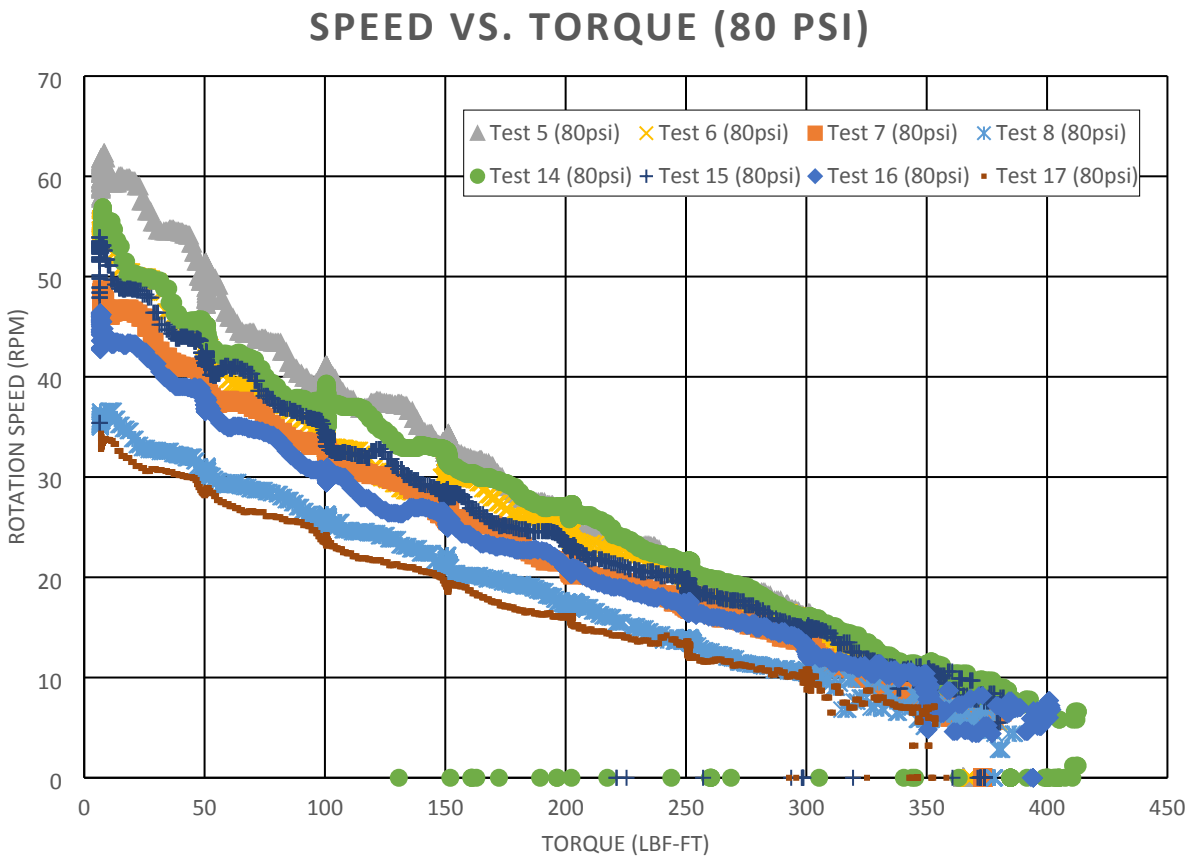

Figure 7-9. Sample dynamometer results for the microhole downhole motor (80 psi [~550 kPa] inlet pressure)

Volumetric flow rates for the compressed air were also measured during the tests. The flow rates ranged from approximately 20 to 50 scfm (~0.6 to ~1.4 m^3/min). One of the observations from the tests was that the stall torque was lower than the expected stall torque for the inlet pressure because of choked flow in the house air supply line. A larger compressor and/or supply line are needed to reach the predicted stall torque when air is flowing.

Lab-scale drilling tests were conducted at the Sandia HOT drilling facility to test the tool under more realistic drilling conditions (Figure 7-10.) Tests were conducted with a 3 in. (~7.6 cm) percussive hammer attached to the end of the motor. Compressed air from an external compressor was used to drive both the motor and the hammer. Two drilling tests of 24 in. (~61 cm) were conducted in the Sierra White granite block as shown in

Figure 7-10. Post-test inspection of the internal motor components revealed no obvious signs of accelerated wear or damage.

Figure 7-10. Motor testing at the Sandia HOT facility

7.8. References for Section 7

[1] Richard, T., Fabrice, D., Edmond, P., and E. Detournay. 2012. "Rock Strength Determination from Scratch Tests," *Engineering Geology*, 147–148 (October 2012), pp. 91–100.

[2] TSC Drill Pipe. *API New Drill Pipe*. TSC Drill Pipe. Available at http://www.drillpipe.com/products/drill-pipe-api-grades.html.

[3] Randolph, S., Bosio, J., and B. Boyington. 1991. "Slimhole Drilling: The Story So Far," *Oilfield Review*, 1(1) (July 1991), pp. 46–54.

[4] Albright, J., D. Dreesen, D. Anderson, J. Blacic, J. Thomson, and T. Fairbanks., T., 2005. Road Map for a 5000-ft Microborehole. Technical Report, Los Alamos National Laboratory, Los Alamos, New Mexico.

[5] Lowe, K.T., Selection and Integration of Positive Displacement Motors into Directional Drilling Systems. Honors Thesis, University of Tennessee, 2004.

[6] Lyons, W.C., and G.J. Plisga. *Standard Handbook of Petroleum & Natural Gas* (2nd ed.) Houston, TX: Gulf Professional Publishing, 2005.

[7] Mauer, William C. *Electro Drilling*. Presentation.

[8] Pixton, D.S. 2005. "Very High-Speed Drill String Communications Network." Report # 41229R14. Available at https://netl.doe.gov/sites/default/files/2018-04/Final-Report-FG123104.pdf.

8. WEIGHT-ON-BIT MANAGEMENT

8.1. Abstract

Drilling systems that use downhole rotation must react torque either through the drill string or near the motor to achieve effective drilling performance. Problems with drill string loading, such as buckling, friction, and twist, become more severe as borehole diameter decreases. Therefore, for small boreholes, reacting torque downhole without interfering with the application of WOB is preferred. We present a novel mechanism that enables effective and controllable downhole WOB transmission and torque reaction. This scalable design achieves its unique performance through four key features: 1) mechanical advantage based on geometry, 2) direction-dependent behavior using rolling and sliding contact, 3) modular scalability by combining modules in series, and 4) torque reaction and WOB that are proportional to the applied axial force. As a result, simple mechanical devices can be used to react large torques while allowing controlled force to be transmitted to the drill bit. We outline our design, provide theoretical predictions of performance, and validate the results using full-scale testing. The experimental results include laboratory studies, as well as limited field testing using a percussive hammer. These results demonstrate effective torque reaction, axial force transmission, favorable scaling with multiple modules, and predictable performance that is proportional to the applied force.

8.2. Introduction

Small diameter boreholes, such as those less than 120.7 mm (4.75 in.) in diameter, have the potential to significantly enhance geothermal energy extraction, exploration, and monitoring [1–3]. The small diameter of the holes enables lower costs, the use of more compact equipment, lower environmental costs, and easier handling [4]. We are particularly interested in decreasing the cost and time to drill exploratory holes by creating compact, portable, small-diameter drilling systems. Replacing heavy drill pipe with more flexible tubing can dramatically reduce system footprint, particularly for deeper holes, but it necessitates downhole rotation.

A common challenge associated with downhole rotation in drilling is achieving sufficient reaction torque while simultaneously delivering controlled WOB [1]. Drilling

dysfunction can be caused by drill string twist and the inability to manage WOB. This is especially true when drill string torsional stiffness is low (i.e., long drilling distances, small diameter drill pipe, etc.). Cable-suspended drilling systems, such as wireline-deployed designs, can simplify drilling operations and have emerged as an approach for Arctic ice and bedrock drilling [5, 6]. These cable-suspended systems cannot rely on surface-derived torsional stiffness and therefore require downhole torque reaction systems [7]. The small borehole diameters, combined with large drilling depths (~5,000 m), make it desirable to drill using a cable-suspended downhole rotation/drilling system, such as the one illustrated in Figure 8-1. Figure 8-1 shows how the drilling and rotation motor are configured at the bottom of the drill string. The downhole rotation motor generates considerable torque to drill, and this must be reacted. In addition, proper downhole WOB must be maintained because if it is too low, drilling performance tends to be poor, and if it is too high, the drill motor may stall.

Some approaches to react torque in cable-suspended drilling systems include friction blades [7], leaf springs [8, 9], side milling cutters [10], and U-shaped blades [11]. Comparative studies of various techniques have shown that achieving a good combination of high torque reaction and low axial resistance remains challenging [7]. Techniques such as coiled tubing and wireline drilling can also be used to provide downhole forces and torques. Options include downhole tractors using a variety of mechanisms, including wheeled approaches, inchworm type configurations, and corkscrew drives [12, 13]. For example, the MaxTRAC downhole tractor uses toothed cams to adaptively grip the borehole wall for inchworm-like motions [12]. The ReSolve device uses a hydraulically powered tractor in combination with a drilling module to resist torque and provide downhole WOB [14].

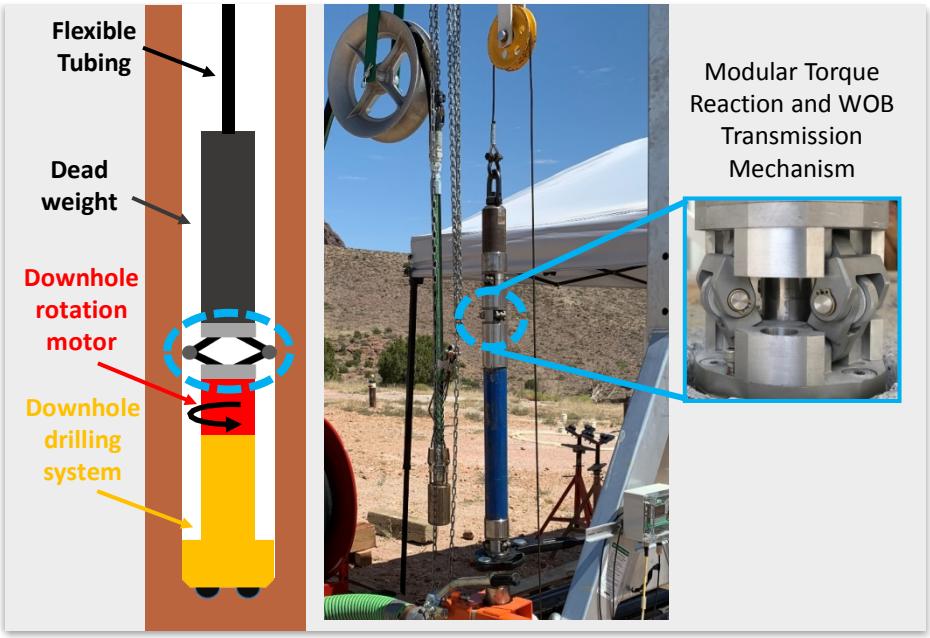

Figure 8-1. Diagram illustrating the drilling concept, the modular asymmetric torque reaction mechanism, and the mechanism integrated into a cable-suspended drilling system

In this section, we outline a novel mechanical module that can be deployed above the downhole motor. This design differsfrom previous tractor, centralizer, and cable-suspended approaches through its use of mechanical advantage, anisotropic friction, and modularity to achieve continuous motion, effective WOB transmission, and scalable torque reaction capacity. We provide a description of the new design, performance analysis for single and multiple units, bench-level measurement of performance with multiple modules, and validation in percussive drilling systems.

Our design, shown in Figure 8-1, uses the vertical force from dead weight to create frictional forces for gripping the walls of the borehole and reacting the torque from the downhole motor. The design uses mechanical advantage to produce large radial forces at the borehole wall. Rolling elements that contact the borehole wall provide vastly different coefficients of friction for different directions of motion. This enables torque reaction (high friction against rotation) while still allowing WOB transmission and continuous penetration (low friction against vertical motion). Increased reaction torque can be achieved by using multiple modules in series without a substantial WOB penalty. The reaction torque limit is proportional to WOB, which is valuable because drilling torque

generally increases with WOB. The design shown in Figure 8-1 has been experimentally validated in both hard and soft rock samples and has been shown to effectively react torques while transmitting WOB under continuous motion. The techniques outlined in this work have applicability beyond microhole drilling. For example, this design holds promise for drilling approaches that involve down-hole rotation and effective torque control, such as directional or cable-suspended drilling [15, 16].

Section 8 begins by outlining the unique and challenging requirements that stem from small borehole drilling. This is followed by an introduction to our mechanism design and a description of the kinematic and static performance of the design. We demonstrate how multiple modules provide favorable scaling, enabling the system to react large torques with relatively modest forces. Our custom dynamic testbed is described in detail, and experimental results are used to illustrate the promise and effectiveness of our design. Results of further testing indicate how the friction properties change in the presence of vibration due to percussive drilling. Field drilling experiments are also described along with preliminary field testing results. This section concludes with a discussion of potential applications of the mechanism.

8.3. Small Diameter Drilling Overview

Scaling analysis reveals the need for new approaches to microhole drilling when the borehole diameter is very small. Specifically, using drill pipe to transmit or resist torsional loads creates a high risk of large torsional wind-up. If we model drill pipe as a solid cylinder, we can examine the torsional stiffness in relation to the hole radius. We use D to denote the hole diameter, L to denote the hole depth, and G to denote the shear modulus:

$$K_{torsion} = \frac{G\pi D^4}{32L} \qquad \text{EQ8-1}$$

Torsional stiffness, $K_{torsion}$, for a solid cylinder is proportional to D^4. This means that torsional deformations become much larger when drilling smaller holes. Therefore, we seek a new solution such as the one shown in Figure 8-1, which reacts torque near the

downhole motor using dead-weight to generate WOB and using flexible tubing rather than continuous lengths of drill pipe. Based on our downhole motor design and prior drilling experiences, we seek a torque reaction and WOB transmission system that meets the following functional requirements:

- System has torque reaction capacity for resisting up to 450 Nm (330 lbf-ft) torque at the downhole motor. This prevents any large rotations of the components above the downhole motor.
- System achieves torque reaction capacity while achieving nominal downhole WOB of 2,225 – 4,450 N (500 – 1,000 lbf).
- System is capable of continuous drilling in order to improve drilling speed and simplify operations.

Our survey of the existing literature and techniques did not provide a solution that combines large downhole torque resistance at relatively low WOBs and continuous motion. Therefore, we developed a mechanism module that can be used independently or combined in series to better meet the unique needs of small-diameter drilling.

8.4. Modular Torque Reaction System

The following subsections provide force calculations, scaling analysis, and performance predictions for the proposed torque reaction system. A sketch of one mechanism module is shown in Figure 8-2. The unique performance of this design stems from four key features: mechanical advantage, anisotropic friction, modular scalability, and proportionality of WOB and maximum reaction torque to applied axial force.

8.4.1. Mechanical Advantage

The ability to react torque is derived from the application of WOB forces. Based on the coordinate system shown in Figure 8-2, this involves producing radial (r) normal forces and corresponding frictional holding forces from applied vertical (z) forces. The mechanism shown in Figure 8-2 uses geometry to convert z direction forces into r direction forces. The mechanism can have two or more linkages that transmit vertical forces to the borehole. We use n to denote the number of linkages. The net radial force, F_r, is the scalar sum of the force across all linkages. This can be determined from the

configuration of the mechanism. In this analysis, we assume the revolute joints are frictionless and the system is quasi-static (not accelerating). We also assume the applied loads are far larger than any internal gravitational loads on the links/wheels. The applied force $F_{in,z}$ is controlled via the drilling rig, and $F_{out,z}$ is the actual WOB.

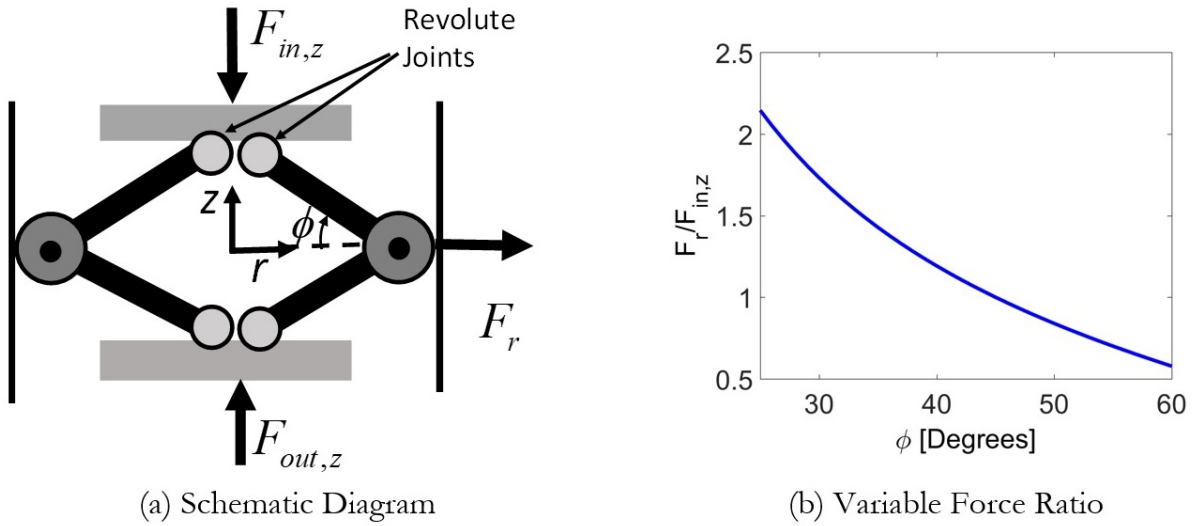

(a) Schematic Diagram (b) Variable Force Ratio

Figure 8-2. Schematic diagram illustrating the torque reaction mechanism design (a) and a plot of the predicted output force ratio as a function of the engagement angle, φ (b)

The equation for the radial force, F_r, is given by:

$$F_r = \sum_{i=1}^{n} \frac{1}{n} \frac{F_{in,z}}{\tan \phi} = \frac{F_{in,z}}{\tan \phi} \qquad \text{EQ8-2}$$

The expressions in EQ8-2 reveal three important features. First, the ratio between the radial force, F_r, and the applied vertical force, $F_{in,z}$, is dependent on the engagement angle, ϕ. Since the nominal borehole diameter is known (equal to the bit diameter), the design can be tuned to give a specific ratio of forces. Second, for angles $\phi < \pi/4$, the radial force will exceed the applied force. For example, if $\phi = \pi/6$, $F_r = 1.73 F_{in,z}$. This mechanical advantage is particularly relevant for cases where the applied force, $F_{in,z}$, is relatively low. Lastly, the net radial force is independent of the number of linkages.

8.4.2. Anisotropic Friction

The outlined mechanism can produce radial forces at the borehole wall as described previously. Figure 8-3 shows that when the wheels contact the borehole wall, these radial forces act as normal forces for friction in the z and θ directions. The net radial force, F_r, can be used to find the net vertical friction force, $F_{f,z}$, and the net tangential friction force, $F_{f,\theta}$. Note that all the net forces are scalar quantities.

$$F_{f,z} = F_r \mu_z \quad \text{EQ8-3}$$

$$F_{f,\theta} = F_r \mu_\theta \quad \text{EQ8-4}$$

The tangential friction force, $F_{f,\theta}$, reacts the torque from the downhole motor, and the translational friction force, $F_{f,z}$, resists the transmission of force from $F_{in,z}$ to $F_{out,z}$. A force and torque balance analysis of the mechanism produces the following expressions. We use the variables μ_z, μ_θ to represent the coefficients of friction for motions in the axial and tangential directions, respectively.

$$\tau_{in} \leq \frac{F_{in,z}}{\tan\phi}\frac{D}{2}\mu_\theta \quad \text{EQ8-5}$$

$$F_{out,z} = F_{in,z} - \frac{F_{in,z}}{\tan\phi}\mu_z \quad \text{EQ8-6}$$

In order to effectively transmit WOB to the bit while simultaneously reacting torque, a design objective is $\mu_z << \mu_\theta$. Rolling contact may be used to enable this direction-dependent behavior. The wheels shown in Figure 8-3 employ rolling contact when moving in the z direction but use sliding motion to move in the θ direction. With this design, we anticipate that μ_θ may be tailored to be roughly an order of magnitude larger than μ_z.

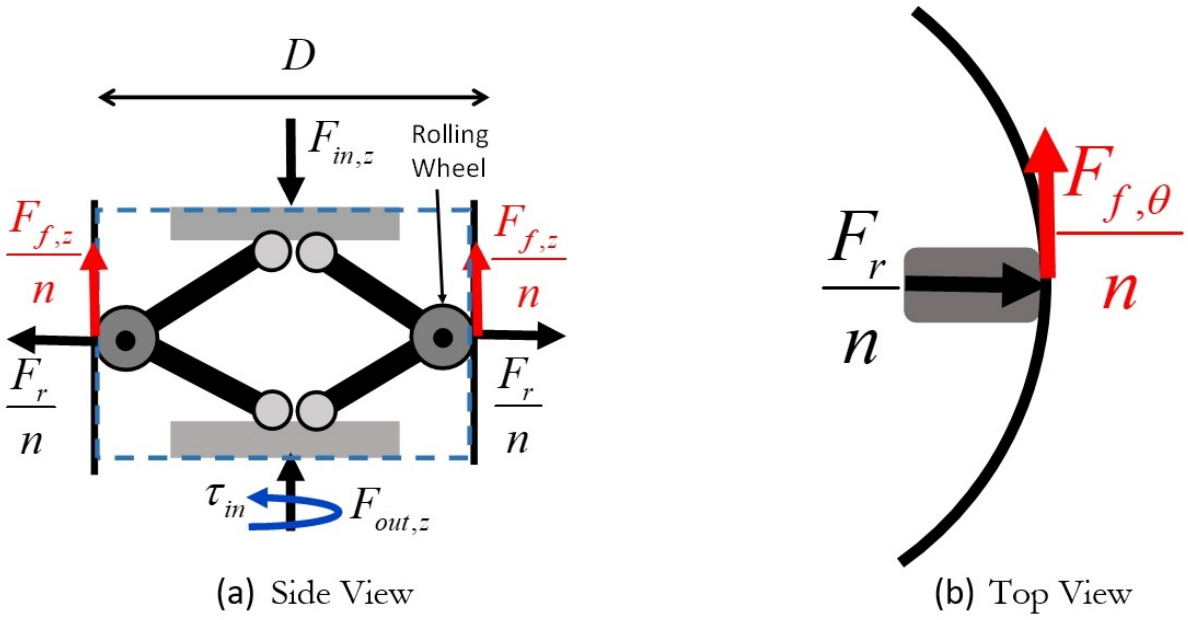

Figure 8-3. Diagrams illustrating directionally dependent behavior through rolling elements

8.4.3. Modular Scaling

If low rolling friction, μ_z, can be achieved, very favorable scaling can be achieved by using multiple modules in series. This concept, depicted in Figure 8-4, enables increased torque reaction and robustness with only small reductions in output force, $F_{out,z}$. As long as μ_z is small (e.g., 0.1), most of the vertical force will be transmitted to the next module. Therefore, each set of rollers pushes out with only slightly reduced radial force. In the case of multiple modules, we use the nomenclature shown in Figure 8-3. In this case, $F_{in,z}$ is still applied at the top, but $F_{out,z}$ is the output force through all the modules. Similarly, the tangential friction force, $F_{f,\theta}$, is the net force associated with all the modules. The performance of a system with N modules is predicted by the following expressions which consider the forces at each module:

$$F_{out,z} = F_{in,z}\left(1 - \frac{\mu_z}{\tan\phi}\right)^N \qquad \text{EQ8-7}$$

$$F_{f,\theta} = \sum_{i=1}^{N} \frac{\mu_\theta F_{in,z}}{\tan\phi}\left(1 - \frac{\mu_z}{\tan\phi}\right)^{i-1} \qquad \text{EQ8-8}$$

The torque needed to induce the start of slipping, τ_{slip}, can be computed from the net tangential friction force:

$$\tau_{slip} = \frac{F_{f,\theta} D}{2} \qquad \text{EQ8-9}$$

We visually demonstrate the favorable scaling performance of multiple modules by predicting nominal performance based on a desired output force, $F_{out,z}$. We use coefficients of friction of 0.1 and 1 for μ_z and μ_θ, respectively. In Figure 8-4-b we show how the normalized predicted input force, $F_{in,z}$, and slip torque, τ_{slip}, scale with multiple modules. The input force and slip torque are normalized by dividing by the value associated with the single-module case. The plot clearly illustrates how the torque reaction capacity increases at a far faster rate than the applied load. Use of multiple modules also affords greater performance in boreholes with deviations or blowouts. Multiple modules spaced apart can still react torque even if a single module does not perform well due to local problems in the borehole.

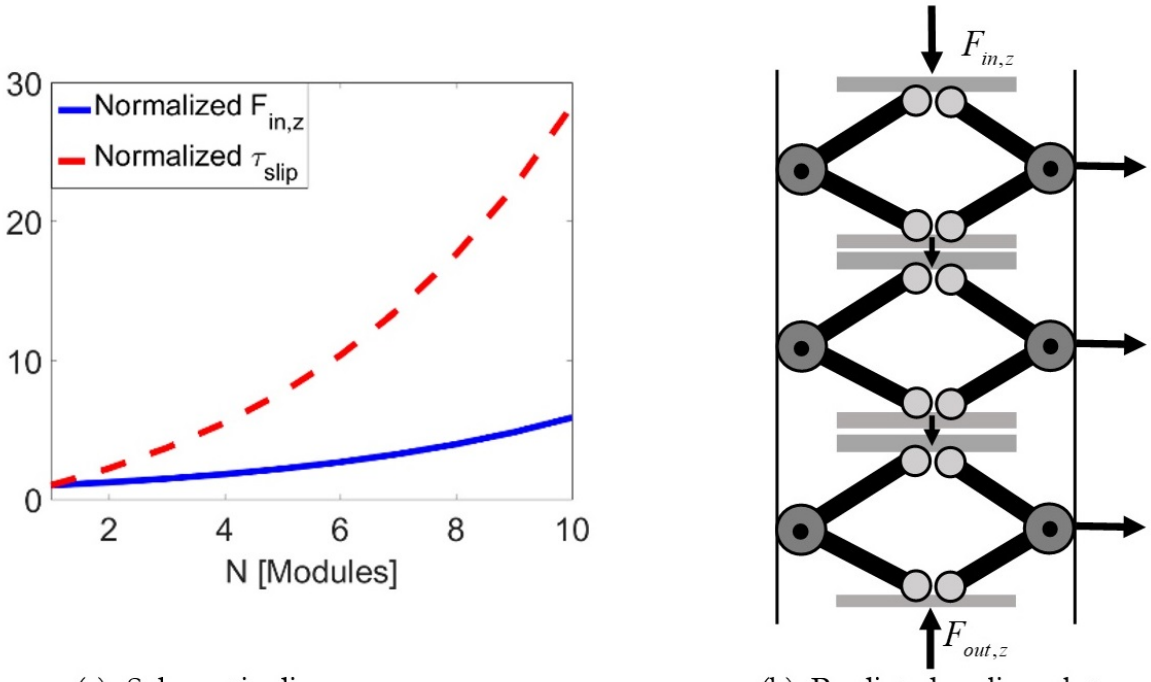

Figure 8-4. Schematic diagram (a) and predicted scaling plot (b) illustrating how multiple modules can be combined in series for improved torque reaction performance

8.4.4. Torque Reaction and Downhole WOB Proportional to Applied Load

A key advantage to this approach is the fact that torque reaction capacity, τ_{in}, and downhole WOB, F_{out}, are both proportional to the force applied at the top, F_{in}. This remains true even when multiple modules are used (EQ8-7–EQ8-8). This behavior enables the mechanism performance and downhole WOB to be simply controlled by modulating the loads at the top. A common way to achieve this is to pull up on the weight above the BHA. Thus, the reaction torque capacity may be increased by increasing the WOB. This generally aligns well with drilling, wherein torque and WOB for effective drilling generally scale together. However, there could be conditions in which it is desired to drill with high torque and modest WOB. This condition could be accommodated at the design stage by using a small value of ϕ or at drilling time by using a separate actuator to create an additional internal force in the module without impacting WOB.

8.5. Nominal Design

8.5.1. Predicted Performance

The analysis outlined in the previous section was used to design a system for drilling ~108 mm (4.0 in.) diameter holes. In Section 8.3, it was determined that it would require a torque reaction of up to 450 Nm (300 lbf-ft) to transmit 2,225 N (500 lbf-ft) WOB at the bottom of the borehole to a downhole motor and hammer drill. The design is conservative in that the maximum torque is reacted using the minimum WOB; additional force can be applied at the top if torque-reacting friction, μ, is less than expected. Coefficients of friction of $\mu = 1$ (steel on rough rock) and $\mu_z = 0.1$ (rolling contact with high-load bushings) were used for the design.

Two free variables are available to tune the design: the engagement angle, ϕ, and the number of modules, N. The design problem can be approached in two ways: (a) determining the number of modules and using this to select the engagement angle, or (b) first choosing the engagement angle and then calculating the number of required modules. For our design, we used approach b and chose the engagement angle. We attempted to maximize the mechanical advantage while still providing some robustness through the ability to expand into slightly larger holes. We achieve an engagement angle

of $\phi = 0.7$ (40°) for a 102 mm (4.0 in.) borehole and can expand to a maximum hole diameter of 108 mm (4.25 in.). Beyond 108 mm diameters, the links will collide and contact with the borehole wall is no longer ensured. We chose to utilize three linkages per module (n = 3). Two axially symmetric linkages/wheels produce no radially-induced moment on the drill string. Thus, two rollers are the minimum when assuming axial symmetry. Additional linkages offer no additional net torque gain but do reduce contact forces. However, additional linkages also add complexity and reduce the annular area for cuttings evacuation. A 3-linkage/roller design was chosen to provide robustness to linkage/roller failure, contact force reduction, and maximization of annular area. The wheel diameter was chosen based on packaging constraints and was not optimized for cuttings evacuation or resistance to material accumulation.

The predicted performance with this design is shown in Figure 8-5. The black dotted line represents the amount of tangential force at the borehole wall needed to resist the design torque, τ_{in}. The red circles denote the predicted tangential frictional force, $F_{f,\theta}$. To achieve our desired performance, a design using four modules provides sufficient reaction torque and gives a 5,000 N safety margin. The use of four modules increases $F_{f,\theta}$ from 3,470 N (780 lbf) (one module) to 14,720 N (3,308 lbf) (four modules). The required input force to achieve the downhole WOB of 2,225 N (500 lbf) is shown with blue markers and increases far more slowly from 2,526 N (568 lbf) to 3,697 N (831 lbf). This illustrates the favorable scaling behavior of our approach.

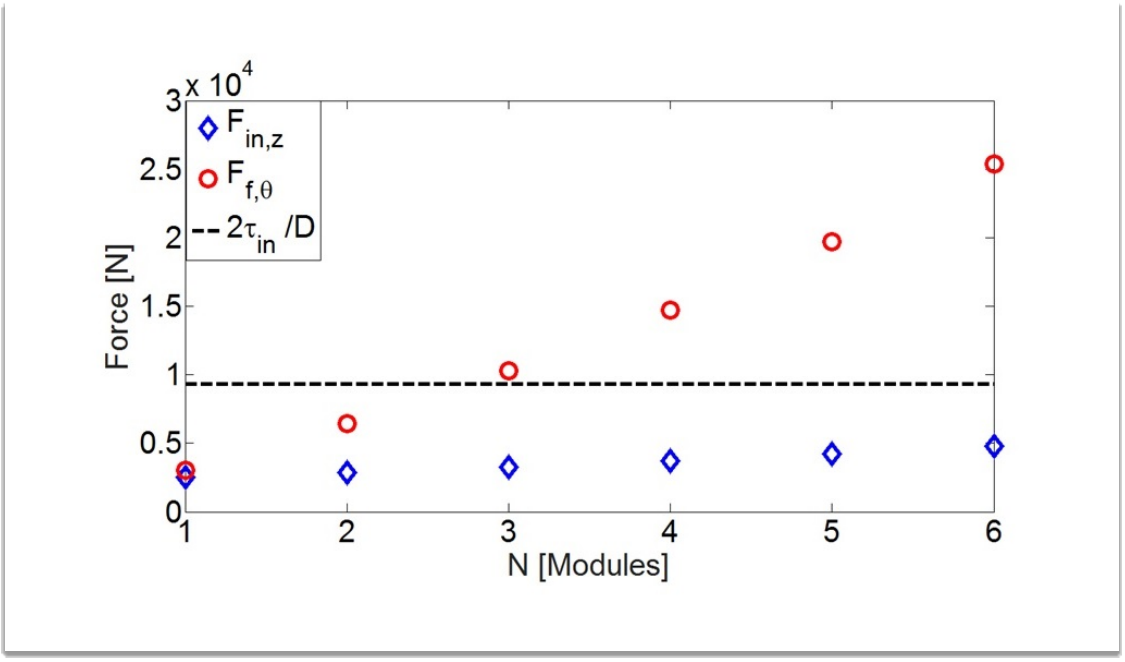

Figure 8-5. Predicted nominal performance based on number of modules

8.5.2. Prototype Design

A prototype design for laboratory evaluation and field testing was developed. This design, shown in Figure 8-6, uses three sets of nested links to achieve the desired strength and kinematics. This design is intended for use in a nominally 108 mm (4.0 in.) diameter borehole and features a clear central space for 25.4 mm (1.0 in.) tubing to supply the downhole components with pressurized air. Mounting features enable multiple modules to be placed in series.

All components are made of 4340 steel alloy. Originally, all bearings were high-load, high-temperature bushings made from PTFE or PEEK. The plastic bushings were used for the majority of experiments described in this work. Field testing demonstrated durability issues, and metal bushings were used for the full system tests. Thrust loads were managed using high-load thrust washers (shown in green in Figure 8-6 on each side of the wheels). This is essential to our design because the wheels are required to roll while subjected to large thrust loads resulting from the downhole motor moment. A variety of wheel geometries can be used. In this work, we focused primarily on smooth wheels where the edges have a radius to match that of the nominal borehole (Figure 8-

6b). This geometry minimizes the effect of wear and relies solely on friction rather than cutting into the borehole wall.

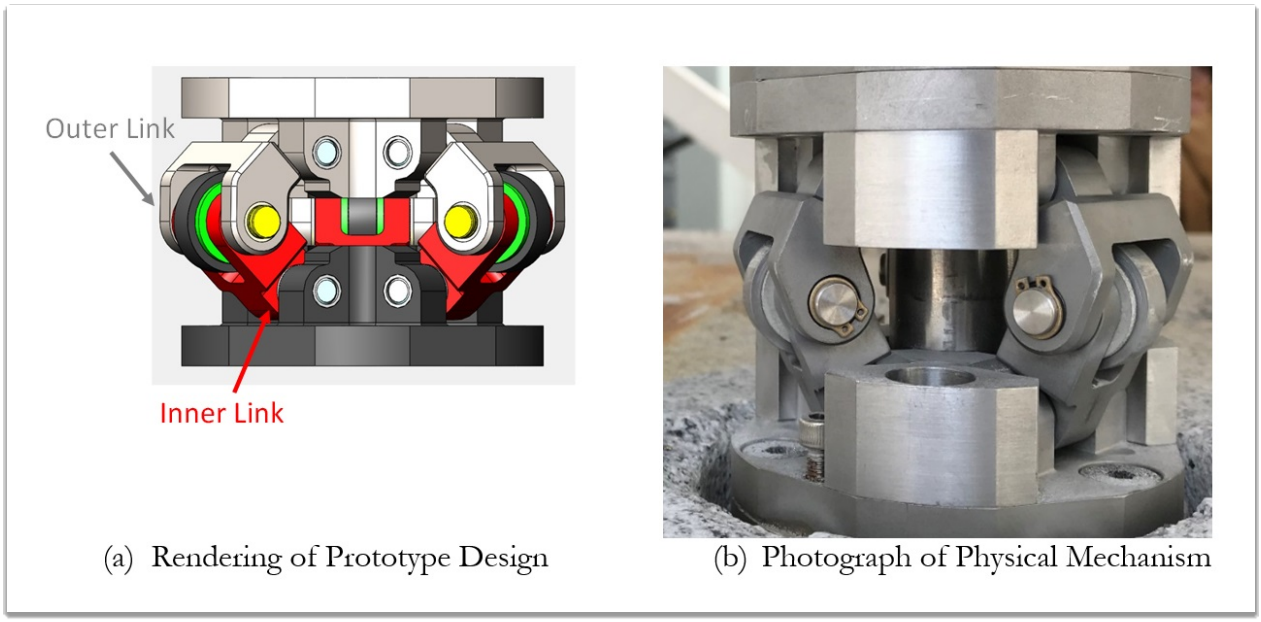

Figure 8-6. Rendering (a) and photograph (b) of the prototype design

Stress analysis was performed on the critical components, such as the shafts and the links. The stress on the shafts stems from the transmission of the vertical and radial forces. A conservative analysis assumes that the bottom-most module (closest to motor) bears the full motor torque until it slips slightly, allowing torque to be shared with the module above it. Using this assumption, the worst-case loading condition is when a single module is subjected to ~4,450 N (1,000 lbf) axial load and 270 Nm (199 lbf-ft) of torque. Components that are most likely to fail are the shafts and the outer links.

We assume that the vertical load is transmitted to the walls uniformly through all three links. The smaller shafts at each end of the mechanism experience a peak stress of approximately 109 MPa (15.8 ksi), providing a safety factor of 7.6 when using 4340 steel (σ_{yield} = 710 MPa).

The loading on the inner and outer links is more complex and stems from resisting torque. If we assume a worst-case scenario where the torque is uniformly resisted by each of the three linkages on only two modules (i.e., the load is shared equally by only half of

the total linkages), each link experiences a tangential force of 1,500 N (337 lbf). Finite element analysis results are shown in Figure 8-7.

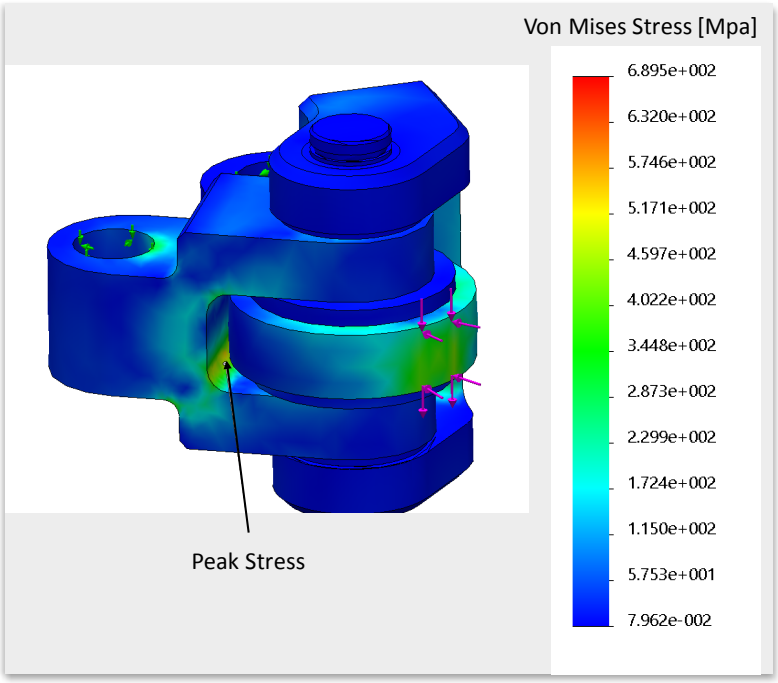

Figure 8-7. Even with these extremely conservative assumptions, the peak stresses remain below the yield strength for 4340 steel (the magenta arrows illustrate the tangential and radial loads on the system); the boundary conditions are stationary shaft constraints on the ends of the inner and outer links

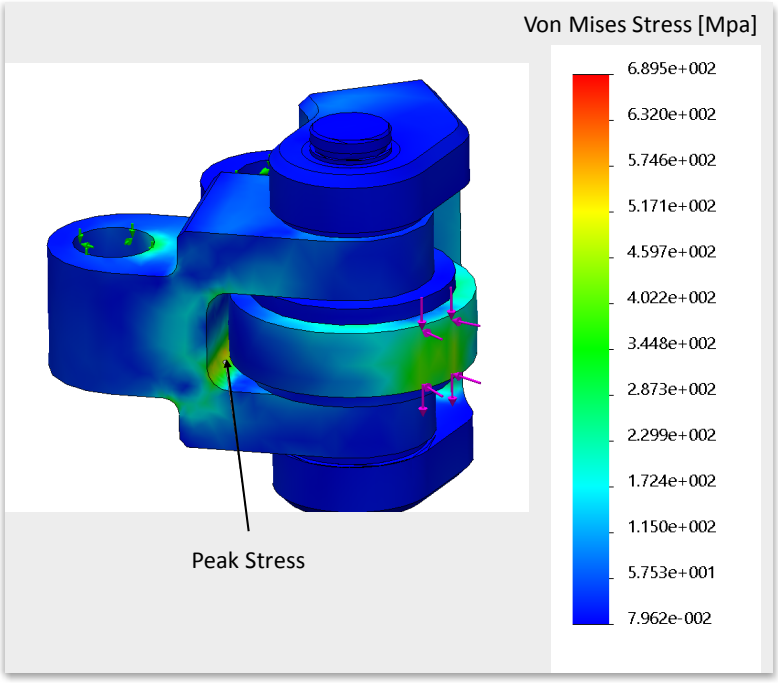

Figure 8-7. Finite element results for the inner and outer links

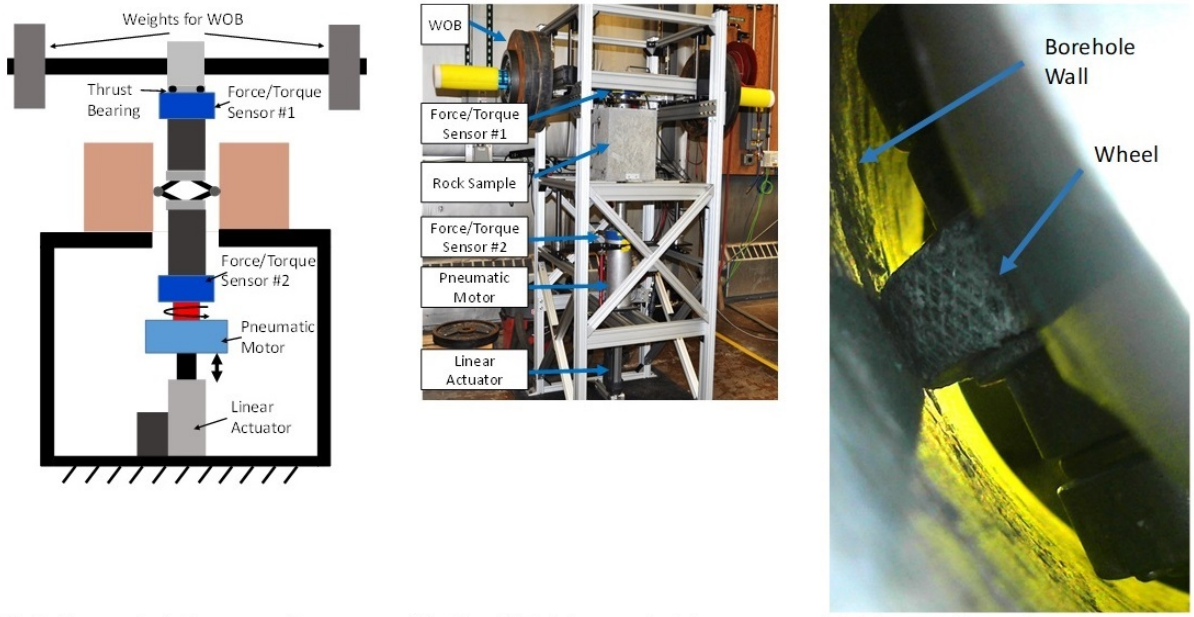

(a) Schematic Diagram for a Torque Reaction Testbed

(b) Sandia's Dynamic Torque Reaction Simulator

(c) Torque Reaction Mechanism Deployed in Sample Borehole

Figure 8-8. A schematic diagram (a) and photograph (b) of Sandia's Dynamic Torque Reaction Simulator; and photograph of a module engaging the borehole wall (c)

8.5.3. Practical Considerations

The spacing between modules depends on many application-specific conditions such as the borehole geometry. Larger spacing increases robustness to borehole geometry deviations but placing the modules too far apart may introduce additional effects such as compliance. In this work, a small spacing is used for laboratory testing, and a larger spacing is used for field testing. Cuttings present another practical concern. If allowed to accumulate, the cuttings could obstruct free operation of the linkages. The bearing blocks are designed to close and leave only a small gap for cuttings to enter (Figure 8-12-c). In addition, positive pneumatic pressure from the central tube can be used to prevent cutting accumulation.

8.6. Laboratory Experimental Evaluation

8.6.1. Dynamic Torque Reaction Simulator

In order to quantitatively validate the performance and models for our torque reaction mechanism, we constructed a new laboratory testbed focused on dynamically evaluating torque reaction and WOB transmission. This system, known as the Dynamic Torque Reaction Simulator, is part of Sandia's geothermal engineering facilities. The torque reaction simulator is illustrated in Figure 8-8 and is designed to emulate the physics of vertical WOB transmission and torque reaction. A schematic diagram shown in Figure 8-8 shows how the torque reaction mechanism sits within a rock sample. Weights are placed above the mechanism to simulate the use of drill collars to create downhole WOB. Axial forces and torques can be measured with each of the two force/torque sensors (Interface 2816 Axial Torsion Load Cell). Force/torque sensor 2 is connected to a pneumatic motor (Rad Torque 10GX), which is used to impart torques onto the torque reaction mechanism. The thrust bearing above force/torque sensor 1 allows the system to rotate if the torque reaction mechanism slips, without moving the weights. The rotary position of the torque reaction mechanism and pneumatic motor can be measured using a US Digital® MAE3 encoder system (not shown). Finally, a linear actuator (FIRGELLI® Automations) is used move the whole assembly up and down. This setup enables testing while allowing the system to move downwards (like in real drilling) and allows measurement of both above-hole and downhole forces and torques.

8.6.2. Single Module Tests

Initial tests utilized one module and were performed in a concrete block. The tests consisted of moving the mechanism to the top of the block, placing a set amount of weights, and then moving the linear actuator downwards while commanding increasing torques. Due to limited stroke, the torques were started at a value known to not cause slip but only slightly below the slip torque. The pneumatic motor does not act as an ideal torque source, so the applied torque fluctuates. A typical set of experimental data is shown in Figure 8-9. Initially the rotation angle, θ, remains flat and then sharply increases as the motor torque reaches the slip levels and the module slips. Since the torque fluctuates, slipping often stops when the torque relaxes. The occurrence of slip is denoted with the black dashed line.

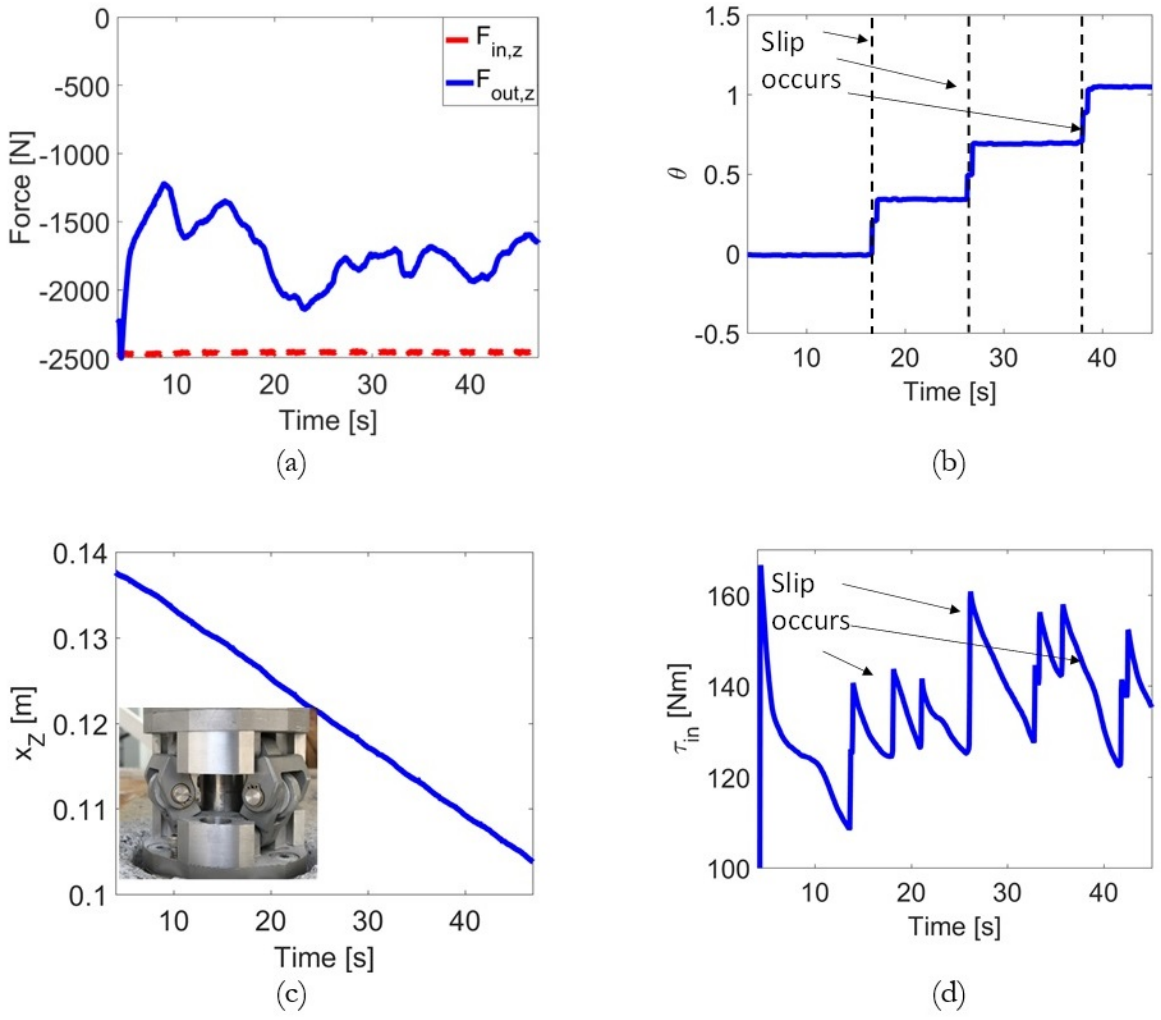

Figure 8-9. Experimental data showing z forces (a), measured rotation angle (b), linear displacement (c), and measured torque (d) during a trial in concrete with one module and 2,537 N applied at the top

For the case shown in Figure 8-9, the amount of weight added to the top of the system was 2,136 N (480 lbf). The other components weigh 400 N (90 lbf), resulting in a total applied force of 2,537 N (570 lbf). The measured forces in the z direction using both force/torque sensors are shown in Figure 8-9-a. The input force measured by force/torque sensor 1 is relatively constant and matches our estimate for total applied force ($F_{in,z}$). The force measured by force/torque sensor 2 is the force transmitted through our torque reaction mechanism ($F_{out,z}$) and is representative of the downhole WOB. As Figure 8-9 shows, while this force fluctuates as the mechanism moves downwards, the average force for this trial is within a 28% deviation of the input force. It is hypothesized that many of the fluctuations stem from irregular surfaces in the concrete borehole. It is important to note that the downhole WOB tracks within variations typical of drilling despite the fact that the mechanism is simultaneously moving downwards (Figure 8-9-c) and subject to substantial twisting torques.

The torque applied by the pneumatic motor is shown in Figure 8-9-d. The torque command is increased until frequent slipping occurs. Examples of slipping are illustrated in Figure 8-9-b, which shows the measured rotation angle, θ. Note that this is a highly dynamic process that depends on friction and involves the transition from static conditions to motion. As a result, the slip does not always occur at consistent torque levels. Therefore, we estimate the slip torque threshold, τ_{slip}, using a statistical approach based on aggregate data for each trial. The angular velocity, $\dot{\theta}$, is first filtered to reduce effects of sensor quantization. Then, the instances where nonzero $\dot{\theta}$ occurs are recorded along with the corresponding measured "motion torque." These torques are compiled and sorted, and a set of the lowest 10 motion torque points (approximately the bottom quartile of data) is used. Specifically, we use the median of this set to determine the actual slip threshold. We believe this is a conservative estimate for τ_{slip} because it uses the lowest slip levels, which may be indicative of small motions and compliance rather than full slipping. The estimate for $\tau_{slip}$for this particular trial is highlighted with a red line in Figure 8-9-d.

Similar data was collected at three other top weight settings: 846 N (190 lbf), 1,268 N (280 lbf), and 1,669 N (370 lbf) and demonstrated similar results. Three trials were performed at each top weight setting. The single module data is summarized in Figure 8-10. The axial force data was compiled by averaging the measured downhole force over the trial, and the slip torque was estimated using the approach described above. The best-fit lines are forced to intercept (0,0) in order to match the structure of our analytical models.

The slopes of the best-fit lines can be used to estimate frictional properties using EQ8-5 and EQ8-6. Using this approach, we get the following estimates: $\mu_z = 0.18$, $\mu_\theta = 1.9$. These values are higher than expected, but their ratio is very close to the design conditions. This is most likely due to the concrete rock sample being relatively soft, which causes the wheels to bite into the material. This higher friction assists torque reaction, and the axial friction remains relatively low, enabling good force transmission.

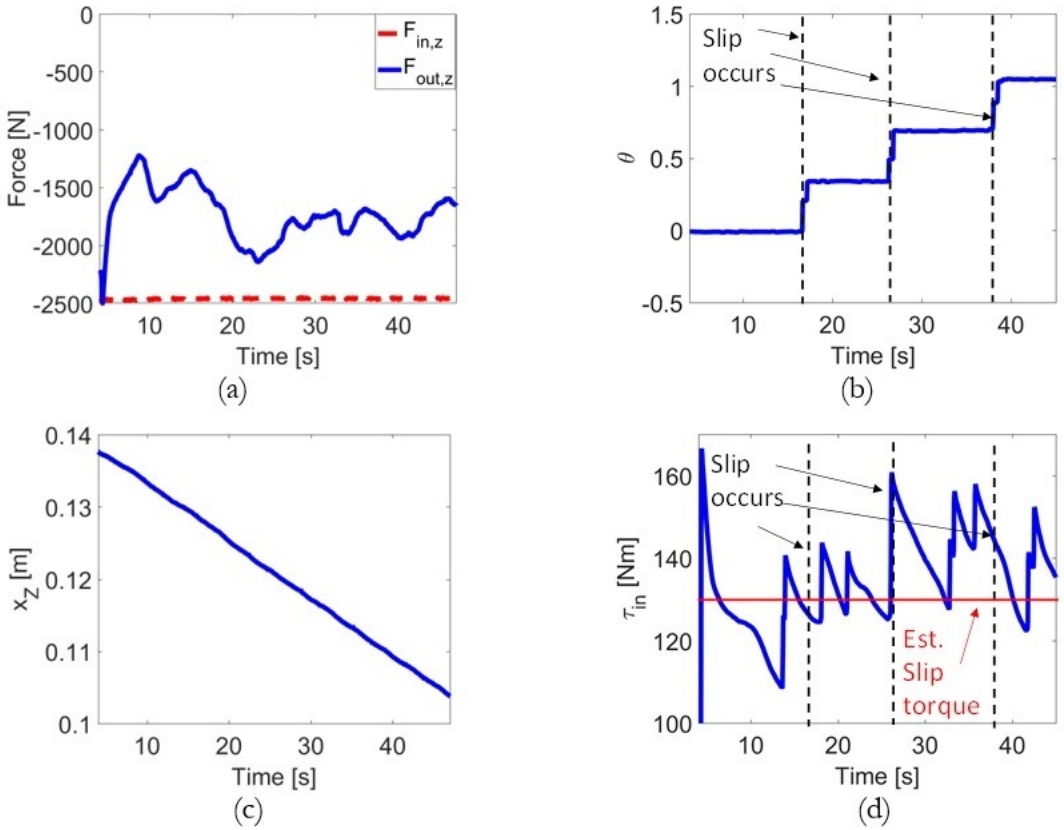

Figure 8-10. Experimental data illustrating force transmission (a) and torque reaction (b) with one module

8.6.3. Two Module Tests

A similar battery of tests was performed using two modules. This was to evaluate the performance of using multiple modules in order to increase torque reaction capacity. Time series data from a sample trial is shown in Figure 8-11. The aggregated data over several applied weight settings is shown in Figure 8-12.

While the structure of the dual module data is very similar to the single module data, there are two clear differences. First, the two-module trials had reduced axial force transmission. This is illustrated most clearly in Figure 8-12-a, which shows that the slope of the line of best fit has decreased from 0.79 to 0.673. We hypothesize that this is mainly due to the increased axial friction from the additional module. This behavior is in line with our theoretical predictions for performance.

The second difference is that the two-module case achieves higher torque reaction per unit input force than the single-module case. If the best-fit slopes of the plots of slip torque versus applied load are compared, this gives a prediction for the relative performance of one module versus two modules. Based on a comparison of the slopes, the slip torque per applied weight is 1.44X higher with two modules rather than one. This is a clear increase in torque reaction capacity.

In theory, two modules should provide a 1.78X improvement, which is 24% larger than what we observed. We believe there are two sources of this discrepancy. First, as described above, the slipping behavior is inherently dynamic and stochastic and therefore difficult to estimate precisely. Second, we hypothesize that the two-module system undergoes asymmetric loading, with the bottom module taking the full torque load until it slips slightly and begins loading the top module. This process is difficult to predict and may cause premature detection of slip. While we remain confident in the overall benefits of using multiple modules, it may be advisable to use conservative safety factors with a design that utilizes multiple modules.

Again, the best-fit lines can be used to estimate the frictional behavior. This time we have to use the expressions for multi-module systems (EQ8-7 and EQ8-8). Using these expressions, we get $\mu_z = 0.15$ and $\mu_\theta = 1.53$. These differ from the single module

predictions by about 20%; however, the 10:1 ratio of friction from the θ to z directions is remarkably consistent across tests.

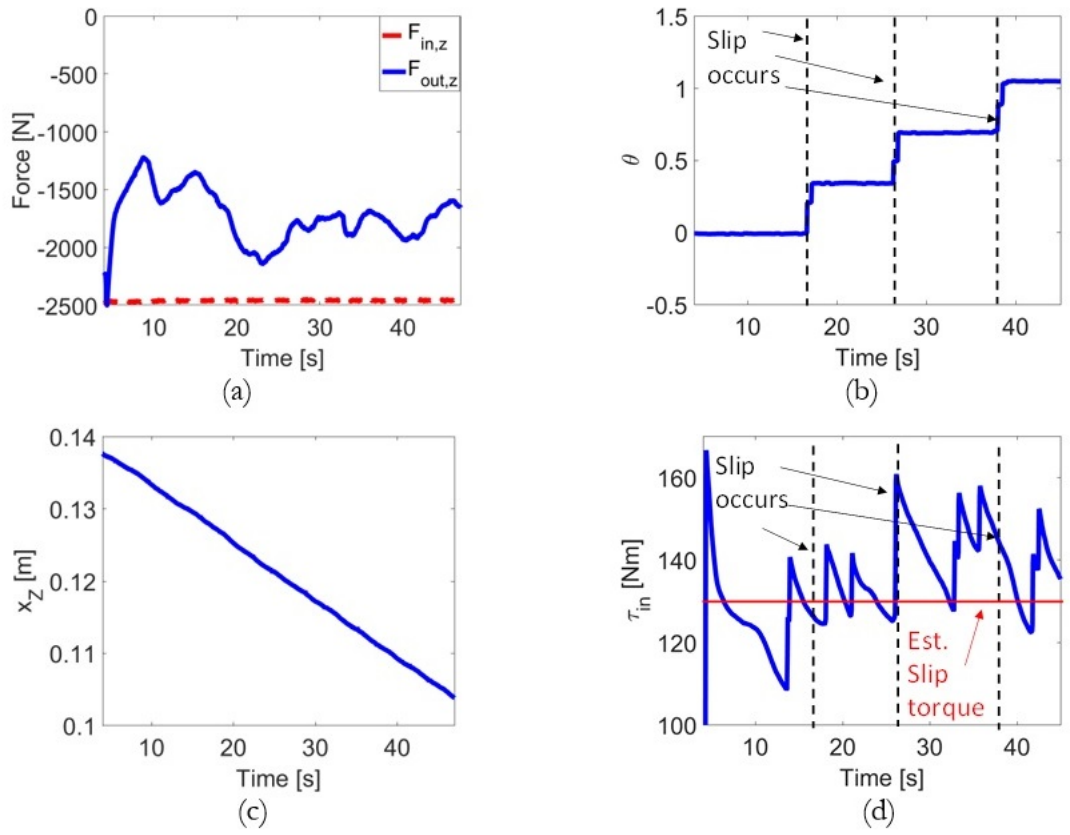

Figure 8-11. Experimental data showing z forces (a), measured rotation angle (b), linear displacement (c), and measured torque (d) during a trial in concrete with two modules and 2,069 N applied at the top

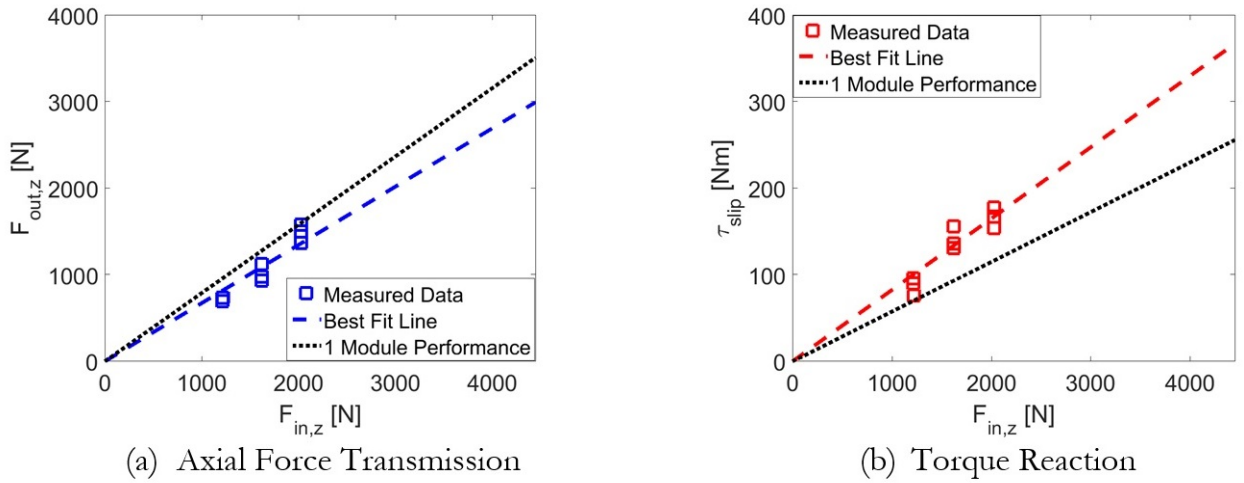

Figure 8-12. Experimental data illustrating force transmission (a) and torque reaction (b) with two modules

8.6.4. Discussion

The testbed results demonstrate the four key attributes associated with our proposed modular torque reaction system. Specifically, the results in this section illustrate (1) that mechanical advantage can be used to resist large torques within a small borehole, (2) that rolling contact creates direction-dependent behavior (axial translation vs. rotation), (3) that the modular design enables scalable performance, and (4) that torque reaction and downhole WOB are proportional to applied load.

8.7. Testing at the Sandia HOT Percussive Drilling Facility

An additional set of validation experiments were performed at the Sandia HOT percussive drilling facility (shown in Figure 8-13-a) to simulate more realistic drilling conditions. The HOT drilling facility is an instrumented drilling system built to test DTHH at high temperatures simulating downhole geothermal conditions. This facility consists of a percussive hammer, pneumatic WOB, and a large top hole pneumatic rotary drive motor. Hammer pressures up to 2,078 kPa (300 psi) can be achieved along with WOBs ranging from 445 to 26,700 N (100 to 6,000 lbf). The top hole motor can produce torques in excess of 1,355 Nm (1,000 lbf-ft). WOB is measured using pressure transducers in the pneumatic cylinders, and motor rotation is measured using a magnetic counter. The motor torque was characterized prior to experiments by comparing input

commands with the measured load on a load cell. The motor torque was most consistent at a setting of 312 Nm (230 lbf-ft).

While we did not utilize the high-temperature capability, the HOT facility enabled testing under realistic forces and torques. Most importantly, it allowed realistic testing of system durability during hammering. The large forces and vibrations caused by hammering are difficult to model and replicate in a laboratory environment. The HOT experiments were performed with two modules (as shown in Figure 8-13-b). The test protocol involved first spinning the motor with a nominal torque output (~312 Nm) and then steadily increasing the applied axial force, $F_{in,z}$, until the spinning was completely halted by torque reacted by the module. This was done with and without hammering, and the results are shown in Figure 8-14. The experimental results show that once a certain threshold WOB is achieved, the rotation angle (blue line) stops increasing. The axial force to react the torque was about 40% greater with hammering than without. This is likely due to the vibrations creating a dither-like effect that prevents static friction to engage. This is an important factor that must be taken into account for field drilling.

Two options for dealing with this effect are adding more modules or increasing the applied force, $F_{in,z}$. Based on the limited HOT data, we still anticipate that a percussive system with four modules will still provide approximately 450 Nm (300 lbf-ft) of torque reaction while achieving a downhole WOB of ~2,200 N (500 lbf).

During testing at the HOT facility, the module was exposed to torques of up to about 500 Nm and applied load of approximately 160,000 N (3,600 lbf). The modules survived these loads without visible damage other than slight wear on the wheels and cracking to plastic bushings. All plastic components were replaced with metal ones for future systems and experiments.

Figure 8-13. Photographs of the Sandia HOT facility (a) and percussive drill equipped with torque reaction modules (b)

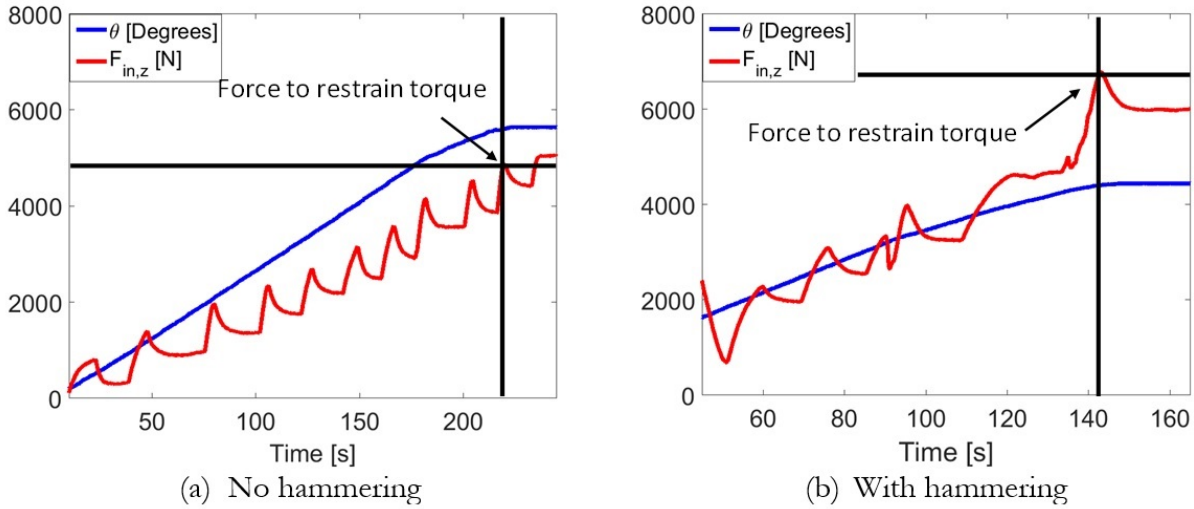

Figure 8-14. Experimental data illustrating torque reaction (~312 Nm) without (a) and with (b) hammering

8.8. Conclusions

Section 8 presented a novel modular mechanism that simultaneously reacts torque and transmits axial forces to a drill bit. We have described the conceptual design, provided mathematical analysis, physical designs, and experimental results. Our results illustrate that this approach enables continuous drilling motion and is capable of scalable performance. Additionally, this system provides force transmission and torque reaction capabilities that are proportional to applied force. Therefore, the resulting physical systems are simple to control and can be used in a manner similar to traditional drilling systems.

We provided a case study example based on drilling of very small (101.6 mm) diameter holes. The design was formulated using the analytical tools proposed in this work and was then validated both on a controlled laboratory test-bed and under realistic drilling conditions at the Sandia HOT facility. These experimental results illustrate that our proposed design has four valuable attributes: (1) mechanical advantage for resisting large torques with friction (~340 Nm), (2) anisotropic frictional behavior using rolling elements (~10X), (3) scalable performance through multiple modules, and (4) load capacity that scales linearly with applied force. The mechanism was also used within a wireline-deployed drilling system where it enabled drilling and prevented twisting of the cable.

We believe the principles outlined in this work have broad applicability beyond microholes. For example, other systems that require downhole rotation such as directional drilling could benefit from the ability to react torque near the motor rather than with the drill string. Similarly, the mechanical advantage principles can be used to create other types of relevant devices, such as inchworm type devices that lock within the borehole or cutting tools that exploit mechanical advantage to apply large radial loads to the borehole wall.

8.9. Acknowledgements

The authors wish to thank Elton Wright, Dennis King, and Michael Kuehl for their assistance with fabrication, prototyping, and testing. This work was funded by the U.S. DOE, Office of Science, GTO WBS – 3.2.1.4.

8.10. References for Section [8]

[1] Zhang, Y., Pan, L., Dobson, P., Oglesby, K., and Finsterle, S. 2012. Microholes for improved heat extraction from EGS reservoirs: Numerical evaluation, In Proceedings of the Thirty-Seventh Workshop on Geothermal Reservoir Engineering, held in Stanford, California, January 30–February 1, 2012. Stanford Geothermal Program, pp. 1–6.

[2] Albright, J., D. Dreesen, D. Anderson, J. Blacic, J. Thomson, and T. Fairbanks., T., 2005. Road Map for a 5000-ft Microborehole. Technical Report, Los Alamos National Laboratory, Los Alamos, New Mexico.

[3] Pritchett, J., 1995. Preliminary estimates of electrical generating capacity of slim holes - a theoretical approach. In Proceedings of the Twentieth Workshop on Geothermal Reservoir Engineering, Stanford University, held in Stanford, California, January 24–26, 1995, pp. 41–46.

[4] Randolph, S., Bosio, J., and Boyington, B., 1991. "Slimhole Drilling: The story so far..." *Oilfield Review*, 1(1), July, pp. 46–54.

[5] Talalay, P., 2014. "Drill heads of the deep ice electromechanical drills." *Cold Regions Science and Technology*, 97 (January 2014), pp. 41–56.

[6] Liu, B., Wang, R., Talalay, P., Wang, Q., and A. Liu. 2016. "Circulation system of an Antarctic electromechanical bedrock drill," *Polar Science*, 10, (August 2016), pp. 463–469.

[7] Talalay, P., Fan, X., Zheng, Z., Xue, J., Cao, P., Zhang, N., Wang, R., Yu, D., Yu, C., Zhang, Y., Zhang, Q., Su, K., Yang, D., and J. Zhan. 2014. "Anti-torque systems of electromechanical cable-suspended drills and test results," *Annals of Glaciology*, 55(68) (December 2014), pp. 207–218.

[8] Wumkes, M., 1994. "Development of the U.S. deep coring ice drill." *Memoirs of National Institute of Polar Research*, 49, pp. 41–51.

[9] Johnson, J., Shturmakov, A., Kuhl, T., and N. Mortensen. 2014. "Next generation of an intermediate depth drill," *Annals of Glaciology*, 55(68) (December 2014), pp. 27–33.

[10] Suzuki, Y., 1979. "New counter-torque devices of a cable-suspended electromechanical drill." *Low Temperature Science*, *Series A*, 37 (March 1979), pp. 163–166.

[11] Zagorodnov, V., Thompson, L., and Mosley-Thompson, E., 2000. "Portable system for intermediate-depth ice-core drilling," *Journal of Glaciology*, 46(152) (January 2000), pp. 167–172.

[12] Alden, M., Arif, F., Billingham, M., Gronnerod, N., Harvey, S., Richards, M., and West, C., 2004. "Advancing downhole conveyance," *Oilfield Review*, 16(3) (September, 2004) pp. 30–43.

[13] Billingham, M., El-Toukhy, A., Hashem, M., Hassaan, M., Lorente, M., Sheiretov, T., and Loth, M., 2011. "Conveyance- down and out in the oil field," *Oilfield Review*, 23(2) (June 2011), pp. 18–31.

[14] Sheiretov, T., 2016. Wireline Tractors and Mechanical Services Tools: Comparative Study of Technical Solutions. In Proceedings of the SPE/ICoTA Coiled Tubing and Well Intervention Conference and Exhibition, held in Houston, Texas, March 2016, Society of Petroleum Engineers, pp. 1–21.

[15] Maidla, E., and M. Haci. 2004. Understanding Torque: The Key to Slide-Drilling Directional Wells. In Proceedings of the IADC/SPE Drilling Conference, held in Dallas, Texas, March 2004, Society of Petroleum Engineers, pp. 1–7.

[16] Pink, T., Koederitz, W., Barrie, A., Bert, D., and D. Overgaard. 2013. Closed Loop Automation of Downhole Weight on Bit Improves Sliding Performance and Reduces Conservatism in Unconventional Horizontal Well Development. In Proceedings of the SPE Annual Technical Conference and Exhibition, held in New Orleans, Louisiana, Society of Petroleum Engineers, pp. 1–14.

9. FIELD DRILLING

The previous sections of this report described the individual subsystem testing and development for the various microhole drilling system components. The next step in the project was to integrate those subsystems and conduct limited field tests to assess the overall performance of the microhole drilling system. Sandia has an existing test site at the New Mexico Tech Energetic Materials Research and Testing Center (EMRTC) Blue Canyon Dome (BCD) in Socorro, New Mexico. The formation consists of weathered rhyolite containing large clasts in the uppermost 30 to 35 ft (~9.1–10.7 m) (Figure 9-1). Deeper in the formation, unweathered rhyolite extends to a depth of up to 400 ft (~122 m). The unconfined compressive strength of the rock in is approximately 38 ksi (~260 MPa).

A drilling contractor spudded and cased a borehole to 35 ft (~10.7 m) with 5.625 in. OD x 4.25 in. ID casing. An additional 20 ft (~6 m) of 4 in. (~10 cm) hole was left open. Figure 9-2 shows a downhole camera image of the formation.

Figure 9-1. Surface shot at the EMRTC BCD site in Socorro, New Mexico

The overall drilling system configuration is shown in Figure 9-3. In keeping with the theme of minimal and compact surface equipment, a wireline truck was used to deploy the drilling assembly. It regulates the WOB by either pulling back or lowering the drilling assembly. A load cell on the main pulley measures the hook load. A hose reel at the

surface provides the conduit for compressed air that powers the downhole motor and percussive hammer. It is tied to the BHA through a swivel assembly with an API box connection.

The wireline truck controls were retrofitted with electro-hydraulic control valves to enable computer control of the wireline tension. This system has a manual bypass that allows it to be operated with a joystick or computer control using a voltage control signal to the electro-hydraulic valve.

Drill collars provide the WOB. Each drill collar is 6 ft (~1.8 m) long and weighs approximately 180 lbs (~81.6 kg). These are stacked to get the desired maximum WOB, with intermediate WOB regulated through the wireline pullback. Based on initial estimates of WOB requirements, we procured 10 drill collars for the field tests.

Figure 9-2. Formation images prior to drilling

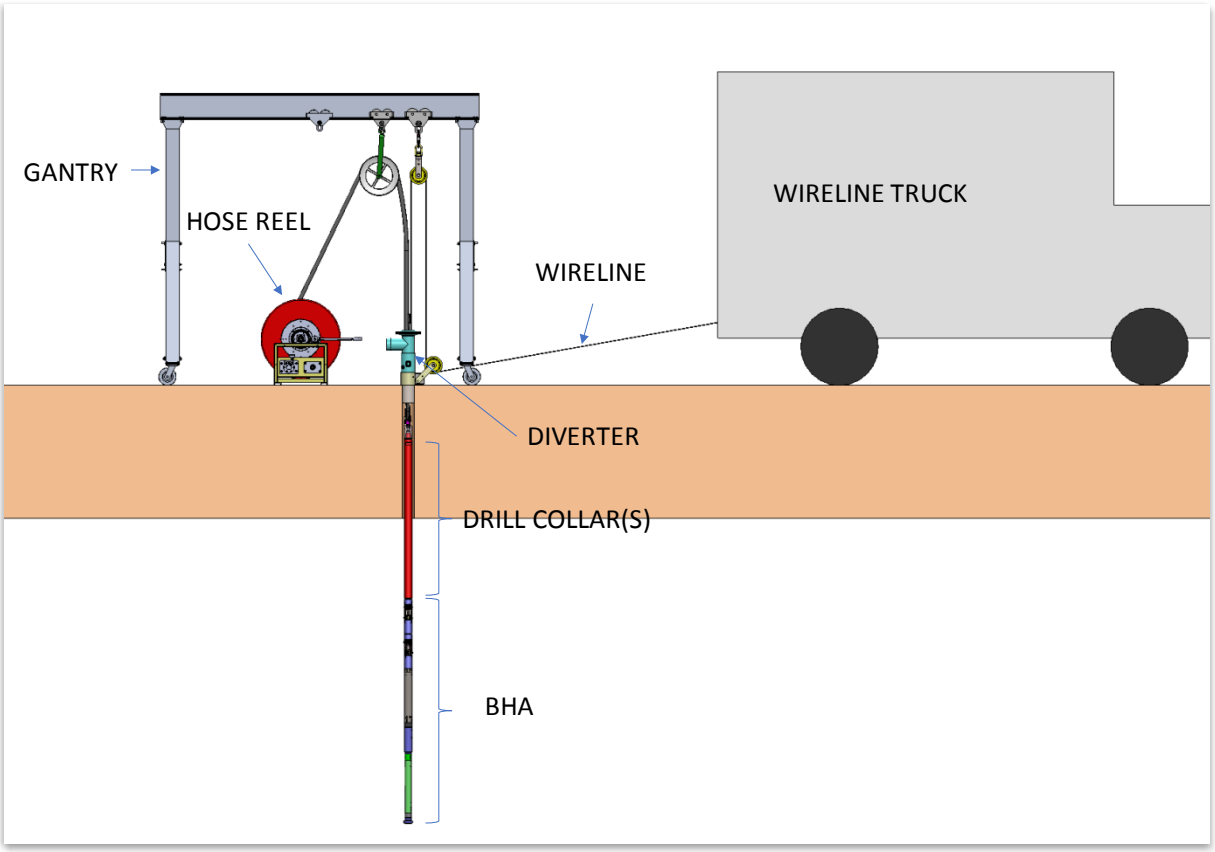

Figure 9-3. Overall drilling system configuration

The active portion of the BHA is shown in Figure 9-4. The drilling assembly consists of the rock reduction component (i.e., DTHH, laser drill), downhole motor, and the WOB/torque reaction modules. For the system deployed in this test, the rock reduction component is the percussive hammer described in Section 6. An external air compressor is required to power the drilling assembly, which for this field test was a 200 psi (~1,380 kPa), 400 scfm (~11.3 m^3/min) compressor (Figure 9-5) connected to the system through a 2 in. (5.4 cm) diameter hose attached to the hose reel. An electro-pneumatic ball valve is used to control the flow of air from the compressor to the hose reel. Additional pictures of the individual components in the BHA are shown in Figure 9-6-Figure 9-9.

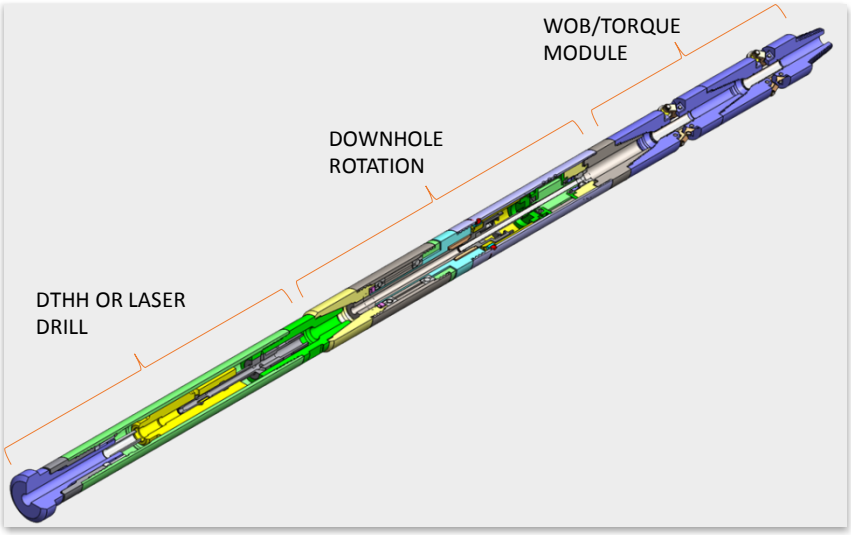

Figure 9-4. Microhole BHA schematic

Figure 9-5. Air compressor used to drive hammer and motor (200 psi [~1,380 kPa], 400 scfm [~11.3 m^3/min])

Figure 9-6. Percussive hammer as assembled in the BHA

Figure 9-7. Air motor as assembled in the BHA

Figure 9-8. WOB modules (MADS) as built and assembled with two sets of reaction modules

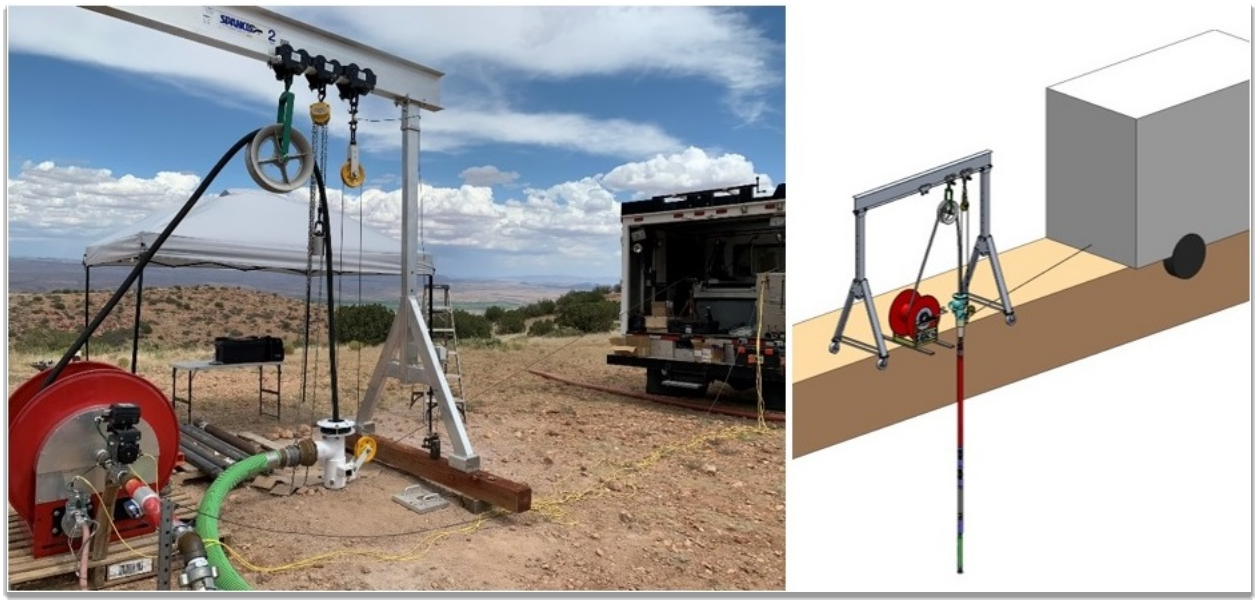

Figure 9-9. Microhole system as built and as designed

Table 9-1 lists the individual drilling assembly components. For the initial tests, only five drill collars were used due to the spudded hole depth. The load cell values listed in the table represent twice the WOB load due to the pulley. The load at the bit is, at most, half of the load cell reading due to friction and drag.

Table 9-1. Drilling Assembly Components with Length and Load Cell Reading

BHA Number	Description	Length (in.)[1]	Load Cell (lbf)[2]
1	QLX35	35.25	
2	Shock Sub	14.19	
3	Air motor	37.68	450
4	WOB module 1	16.00	471
5	21 in. sub	21.00	
6	WOB module 2	16.00	670
7	Drill collar	72.00	965
8	Drill collar	72.00	1,320
9	Drill collar	72.00	1,680
10	Drill collar	72.00	1,990
11	Drill collar	72.00	2,370

[1] Multiply in. by 2.54 to get length in cm

[2] Multiply lbf by 4.448 to get load in N

Four of the torque reaction modules were deployed as part of a full microhole drilling system. This wireline-deployed system uses a downhole motor and percussive hammer to drill 101.6 mm (4 in.) diameter holes. Drill collars were used to apply WOB. The BHA consisted of (from bottom to top) percussive hammer, downhole motor, torque reaction modules, and up to 1,800 lbs (~816 kg) of drill collars. A photograph of the complete system is shown in Figure 9-8. When deployed during drilling, visual inspection is used to assess the performance of the torque reaction modules. The downhole motor caused the cable to twist when the torque reaction mechanism was not engaged with the formation.

When engaged, the torque reaction mechanism prevented twisting of the cable suspension and allowed the drilling assembly to advance as intended. Performance was qualitatively evaluated by drilling a short distance with the modules engaged. During initial drilling, the system worked nominally as illustrated by the dust plume in Figure 9-10. However, after a short distance, the system became stuck in the formation, and the characteristic hammering pulsation and motor rotation signature stopped.

Efforts were made to pull back on the wireline, as well as slack-off, to free the drilling assembly. Up to 5,000 lbf (~22,240 N) of pull force was applied to the wireline, but none of those efforts were successful in unsticking the BHA. A separate attempt was made to fish out the assembly using a conventional drilling rig.

Figure 9-10. Dust plume from drilling

The additional pulling capacity of the standalone rig extracted most of the components from the borehole. As shown in Figure 9-11, there was some damage to the torque modules that likely occurred during drilling. Several of the rollers and pins were missing when the tool was extracted. There was also what appeared to be a fracture in the links as

highlighted in Figure 9-12. Both of these are indications that the MADS modules experienced loads that we did not fully anticipate.

Figure 9-11. Results of post-drilling fishing attempts

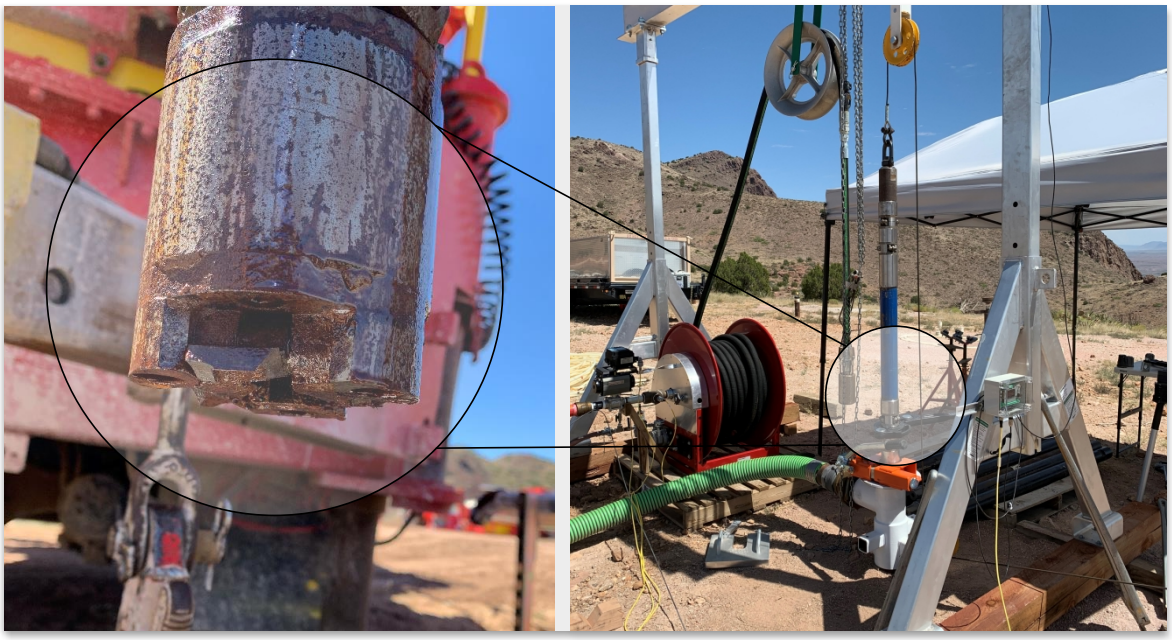

Figure 9-12. Lower set of MADS components after extraction

At the time this report was compiled, there were several components still resting at the bottom of the W-5 hole at BCD. These include the modified QLX35 hammer, the air motor, and some components from the remaining portion of the MADS module. There is still a planned fishing attempt to extract the remaining components.

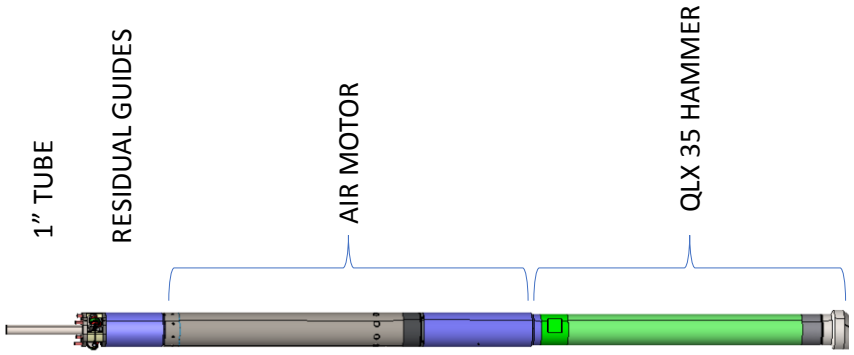

Figure 9-13. Residual downhole components

Overall, the limited field trial was an invaluable exercise. It confirmed some of our initial notions about the drilling assembly behavior related to drill string twist and how to manage that using a flexible drill string. There were challenges with the design and durability of some of the components, which will have to be addressed prior to future testing. The motor and percussive hammer were well matched and performed well before the other component failures.

10. CONCLUSION

This research program successfully demonstrated the technical feasibility of low WOB microhole drilling for geothermal exploration, assessment, and monitoring. High drilling costs—especially those associated with the exploration and confirmation of geothermal resources—remain a significant barrier to geothermal energy development. Lower cost microholes are a potential solution, but high WOB drilling technologies do not scale down to microhole sizes, which are typically less than 4 in. (~10 cm) in diameter.

Our program conceived, developed, and conducted limited testing of two proof-of-concept low WOB microhole drilling systems: (1) a laser-assisted mechanical drill, which was tested in the laboratory and is currently at a low TRL and (2) a lightly modified COTS percussive hammer, which was deployed in the field and has a high TRL due to its commercial availability. The results of our research warrant further investigation, especially into methods of ruggedizing the subsystems and components for the extreme conditions (i.e., high temperatures and pressures, corrosivity) encountered during geothermal drilling.

The following tasks were conducted under this research program: (1) evaluation of the technical and economic feasibility of low WOB technologies; (2) development of downhole rotational solutions because the ability to generate rotation downhole and control WOB will be key to the success of this technology; (3) development of design specifications for the two low WOB drilling systems; (4) development of a mechanism that enables effective and controllable downhole WOB transmission and torque reaction; and (5) evaluation and testing of the two low WOB technologies.

As part of our research, we conducted a flow analysis to bound the size of usable microholes. We showed that production flow tests using microholes have physical limitations, preventing a continuous flow of geothermal fluid for geochemical sampling and analysis. Thus, we propose repurposing existing and newly emerging fluid analysis techniques to conduct these analyses in situ.

Although the results of the laboratory-tested laser-assisted mechanical drill were encouraging, the system encountered challenges that prevented it from achieving the desired ROP. The suboptimum beam profile slowed the drilling process. Future work

should focus on designing and testing a system to improve manufacturability, assemblability, ROP, and reliability based on the lessons learned during this project. Then the originally proposed parameter space should be reexamined.

The limited field drilling program largely focused on gaps in COTS hardware used in the low WOB microhole drilling system. Supporting equipment, including downhole rotation and a drill string twist reaction tool, were developed to enable wireline deployment of a drilling assembly. A WOB control algorithm was developed and refined for the overall system controller to optimize WOB during drilling. The motor and percussive hammer performed well, but there were challenges with the design and durability of some of the components, which will have to be addressed prior to future testing. In addition, the drill conveyance system, which advances the drill bit and retracts it on pullback, requires additional capacity for pullback.

The technology explored in this research program has broader application to other drilling systems requiring downhole rotation, such as directional drilling, which benefit from the ability to react torque near the motor rather than with the drill string. Similarly, the mechanical advantage principles can be used to create other types of relevant devices, such as inchworm type devices that lock within the borehole or cutting tools that exploit mechanical advantage to apply large radial loads to the borehole wall.

DISTRIBUTION

Email—Internal

Name	Org.	Sandia Email Address
Jiann-Cherng Su	08866	jsu@sandia.gov
Anirban Mazumdar	05449	amazumd@sandia.gov
Stephen Buerger	06533	sbuerge@sandia.gov
Adam Foris	08916	aforis@sandia.gov
Giorgia Bettin	08866	gbettin@sandia.gov
Technical Library	01977	sanddocs@sandia.gov

Email—External

Name	Company Email Address	Company Name
Angel Nieto	Angel.nieto@ee.doe.gov	U.S. DOE Geothermal Technologies Office

Sandia National Laboratories

Sandia National Laboratories is a multimission laboratory managed and operated by National Technology & Engineering Solutions of Sandia LLC, a wholly owned subsidiary of Honeywell International Inc. for the U.S. Department of Energy's National Nuclear Security Administration under contract DE-NA0003525.